

3-26-2015

Surface Geometry and Chemistry of Hydrothermally Synthesized Single Crystal Thorium Dioxide

Scott W. Key

Follow this and additional works at: <https://scholar.afit.edu/etd>



Part of the [Nuclear Engineering Commons](#)

Recommended Citation

Key, Scott W., "Surface Geometry and Chemistry of Hydrothermally Synthesized Single Crystal Thorium Dioxide" (2015). *Theses and Dissertations*. 83.

<https://scholar.afit.edu/etd/83>

This Thesis is brought to you for free and open access by the Student Graduate Works at AFIT Scholar. It has been accepted for inclusion in Theses and Dissertations by an authorized administrator of AFIT Scholar. For more information, please contact AFIT.ENWL.Repository@us.af.mil.



**SURFACE GEOMETRY AND CHEMISTRY OF HYDROTHERMALLY
SYNTHESIZED SINGLE CRYSTAL THORIUM DIOXIDE**

Thesis

Scott W. Key, Major, USA

AFIT-ENP-MS-15-M-87

**DEPARTMENT OF THE AIR FORCE
AIR UNIVERSITY**

AIR FORCE INSTITUTE OF TECHNOLOGY

Wright-Patterson Air Force Base, Ohio

DISTRIBUTION STATEMENT A.

APPROVED FOR PUBLIC RELEASE; DISTRIBUTION UNLIMITED.

The views expressed in this thesis are those of the author and do not reflect the official policy or position of the United States Air Force, Department of Defense, or the United States Government. This material is declared a work of the U.S. Government and is not subject to copyright protection in the United States.

AFIT-ENP-MS-15-M-87

**SURFACE GEOMETRY AND CHEMISTRY OF HYDROTHERMALLY
SYNTHESIZED SINGLE CRYSTAL THORIUM DIOXIDE**

THESIS

Presented to the Faculty

Department of Engineering Physics

Graduate School of Engineering and Management

Air Force Institute of Technology

Air University

Air Education and Training Command

In Partial Fulfillment of the Requirements for the

Degree of Master of Science in Nuclear Engineering

Scott W. Key, BS

Major, USA

March 2015

DISTRIBUTION STATEMENT A.
APPROVED FOR PUBLIC RELEASE; DISTRIBUTION UNLIMITED.

**SURFACE GEOMETRY AND CHEMISTRY OF HYDROTHERMALLY
SYNTHESIZED SINGLE CRYSTAL THORIUM DIOXIDE**

Scott W. Key, BS

Major, USA

Committee Membership:

Tony D. Kelly II, PhD
Chair

James C. Petrosky, PhD
Member

John W. McClory, PhD
Member

Alex G. Li, PhD
Member

Abstract

The surface chemistry and geometry of hydrothermally grown, single crystal ThO₂ was studied using X-ray Photoemission Spectroscopy (XPS) and Atomic Force Microscopy (AFM). The crystal was studied before and after sputter etching with Ar⁺, heating up to 675 K, and dehydration with dry nitrogen. The hydrothermal growth technique incorporated Cs and F into the near surface bulk. Heating to 675 K drove off the F, but did not remove the Cs in measureable quantity. Not all hydrocarbons were removed by the cleaning technique, but OH was partially removed by heating to 675 K.

Sputtering with Ar⁺ at 75° grazing incidence removed crystallite impurities and created a more uniform surface geometry. The Th 4f peak resolution, as measured by XPS, improved by a factor of 3; the surface roughness, as measured by AFM, reduced by a factor of 2; and the deviation in adhesion force measurements at different location on the crystal reduced by a factor of 2.

The surface of ThO₂ becomes more metallic with heating. X-rays, used in XPS, created 7.3 eV of charging on the ThO₂ crystal surface at room temperature. Metallic Th 4f peaks appeared in the XPS spectrum at 675 K, while the charging was reduced.

The adhesion of hydrophilic metal tips to ThO₂ crystal is caused by capillary, van der Waals and dipole induced-dipole forces. For the as-grown crystal, the adhesion force strength by metal was Au>In>Ni>Ti. Post-cleaning the adhesion force relation is In>Au~Ni>Ti. Interface energy computations confirm that the gold metal adhesion

decreased by half for the cleaned crystal. Based on these results, indium is the best choice of metal for application of contacts to the ThO₂ single crystal used in this research.

Acknowledgments

I would like to thank the sponsor of this work, the Department of Homeland Security, Domestic Nuclear Detection Office.

I would like to thank my committee for their commitment to science, timely advice and patience. Dr. Kelly, as chair, provided me with excellent guidance and motivation to accomplish the work with scientific vigor. I appreciate his willingness to review my work and provide necessary corrections. I would like to thank Dr. Petrosky for always pushing the bigger picture and ensuring the focus of the research was meeting the larger goals. I appreciate Dr. McClory's skeptical views and critical thinking that kept me from straying into scientific error. I appreciated Dr. Li's tremendous patience that was demonstrated as I attempted to load the AFM tip onto the holder and the tip fell tip-down time after time. I appreciate his willingness to listen to my ideas and provide thoughtful insights.

I would like to thank the fellow scientists that assisted me with the research. I would like to thank Dr. Hengehold for his mentorship and thoughtfulness. I appreciate his willingness to listen to my crazy ideas and respond with his vast scientific knowledge. I would like to thank Dr. Turner for his work in assembling, maintaining, and operating the PES chamber. I appreciate his instruction of operation, his patience when problems occurred, and his work on mounting the crystal. I would like to acknowledge Mr. Greg Smith for his assistance with the Zygo Profilometer, SEM, and making the small repairs that keep the lab functioning. Finally, I would like to thank Dr. Burggraf for his ideas on surface chemistry.

I would like to thank God for the gifts he has given me. I would like to thank my family, Stephanie, Joshua, and Bryan for all their support and understanding. I appreciated my wife's encouragement and enthusiasm. Without her, my own enthusiasm would wane. She is the source of my confidence. My children are a blessing and provide a useful relief from the day.

Table of Contents

	Page
Abstract	iv
Table of Contents	vii
List of Figures	ix
List of Tables	xi
List of Acronyms	xii
List of Symbols	xiii
I. Introduction	1
1.1 Research Motivation: ThO ₂ as a Potential Oxide Layer in Electronic Devices	1
1.2 Research Objectives	3
II. Theory	5
2.1 Description of the Four Forces that Comprise the Adhesion Force	5
2.1.1 The Dispersion Forces, F_{vdW}	6
2.1.2 The Electrostatic Force, F_{es}	7
2.1.3 The Capillary Force, F_{cap}	10
2.1.4 The Contact Force, F_{cont}	12
2.2 Description of Surface and Interface Energy	12
2.3 AFM Adhesion Measurement and Cantilever Spring Constant Calibration	16
2.4 Sputter Etching of Crystals with Ions.....	18
2.5 X-ray Photoemission Spectroscopy	22
2.5.1 XPS Shakeup Satellites of ThO ₂	23
2.5.2 The XPS Spin-Orbit Splitting of Peaks	24
2.5.3 Chemical Shifts and Surface Sensitivity of XPS.....	25
2.5.4 From Electron Kinetic Energy to Electron Binding Energy	26
III. Methodology	27
3.1 General	27
3.2 AFM Spectroscopy to Measure Adhesion Force and Surface Roughness	28
3.3 Dehydration of the Crystal Surface	35
3.4 Cleaning the Crystal Surface by Sputter Etch	36
3.5 Cleaning the Surface by Heating	38
3.6 X-ray Photoelectron Spectroscopy of As-Grown and Cleaned Surfaces	39
IV. Results and Analysis	45
4.1 Results and Analysis of the As-Grown ThO ₂ Crystal	45
4.1.1 XPS Ta Foil Peaks and Baseline Th Peaks	45

4.1.2 Hydrothermal Growth Mineralizer Impurities in the As-Grown ThO ₂ Crystal	47
4.1.3 Atmospheric Adsorbents on the As-Grown ThO ₂ Crystal	48
4.1.4 Roughness of the As-Grown ThO ₂ Crystal as Measured by AFM	50
4.1.5 AFM Adhesion Force Measurements of the As-Grown ThO ₂ Crystal	52
4.1.6 Surface and Interface Energy Computations for the As-Grown ThO ₂ Crystal	55
4.2 Changes in the ThO ₂ Crystal during Sputtering, Heating, and Dehydration.....	59
4.2.1 Heating Reduces the Mineralizer Impurities.....	59
4.2.2 Heating Changes the Concentration of Atmospheric Adsorbents.....	61
4.2.3 Heating Changes the Quantity of Charge on the ThO ₂ Surface	63
4.2.4 Humidity Reduces Adhesion Force for Hydrophilic Indium AFM tip	69
4.3 Impurities and Adhesion of the Crystal at the End of Cleaning.....	72
4.3.1 ThO ₂ Impurities Reduced.....	72
4.3.2 Th 4f Peak Improvement	73
4.3.3 Sputtering Improved Surface Variability	74
4.3.4 Adhesion Force and Interface Energy of Cleaned ThO ₂ Crystal	79
V. Conclusions and Recommendations for Future Research.....	83
5.1 General	83
5.2 Future Research	85
Appendix A.....	88
Load lock sample change out procedures.....	88
Sputtering of sample procedures	88
AFM measurement procedures.....	89
Appendix B	91
Silicon Sputtering Results	91
References.....	94
Vita.....	97

List of Figures

Figure	Page
1. Crystal 8a grown by the hydrothermal growth technique.....	3
2. AFM tip radius, R_t , and the distance, D , from the ThO_2 crystal surface.....	5
3. The (111) crystal face of ThO_2	8
4. Diagram of the influence of the capillary force on water adhesion in an AFM measurement.	11
5. Diagram of the adhesion forces acting at one location.	14
6. Diagram of the surface labels for the AFM tip, ThO_2 surface, and water.	15
7. AFM tip and cantilever deflects a distance due to adhesion force.....	17
8. Sputtering yield of ThO_2 verses sputtering energy of bombarding Ar^+	21
9. The schematic depicts the atomic binding energy levels for XPS.....	27
10. Process chart for determining geometry and chemistry of ThO_2	28
11. This AFM Setup with the dry nitrogen bag was used for adhesion measurements ...	31
12. Although for indium, this plot is typical of the adhesion force spectral measurements used for the comparison of metal tips onto the ThO_2 single crystal.	34
13. Photograph of the XPS system that was used for this experiment.	41
14. ThO_2 single crystal #8a mounted to Ta foil plate.	42
15. The PeakFit routine fits the Th 4f peaks post sputtering.	43
16. Ta and as-grown spectrum are plotted without shifting due to the system work function.	46
17. F and Cs impurity plot.....	48

18. O and C peaks for the as-grown ThO ₂ crystal. The peaks on the right in each spectrum are associated with Ta.	49
19. 3 x 3 μm initial surface feature scan by AFM..	50
20. Crystal surface feature error verses electronic error.	51
21. As-grown thorium dioxide adhesion force and graphite adhesion force.	52
22. Adhesion plot of indium and gold on as growth ThO ₂ .	54
23. The effective radius of the tip is different for capillary and non-capillary forces..	56
24. Fluorine to thorium peak ratio.....	60
25. The C 1s peaks during 2nd heating experiment.....	62
26. Uncorrected experimental binding energy verses Fuggle reported binding energy...	65
27. System work function and charging of ThO ₂ verses temperature.....	67
28. The Th peaks at 675 K during the heating phase of the 2nd sequence..	68
29. Adhesion force as a function of relative humidity.....	70
30. In metal tip adhesion force spectrum on ThO ₂ and graphite.	71
31. The ThO ₂ (left peak) and Ta (right peak) O1s peaks as a function of sputter etching (left side chart) and heating (right side chart).	73
32. Thorium 4f peaks before and after the surface processing	74
33. Changes in ThO ₂ single crystal geometry and topography histogram.....	76
34. ThO ₂ crystal 8a tapping mode surface scan after sputtering and heating..	77
35. Adhesion force for each metal tip before and after surface processing	79

List of Tables

Table	Page
Table 1. Useful properties of SiO ₂ , ThO ₂ , and HfO ₂	2
Table 2. List of seven metal candidates and pertinent metal properties	32
Table 3. Argon sputtering gun was set to the tabulated values for different energies....	37
Table 4. Mean sputtering depth computations based on Ar ion sputtering energy.....	38
Table 5. As-grown interface energy estimates for metal tips onto ThO ₂	57
Table 6. Affect of surface dehydration on interface energy quantities.....	58
Table 7. O 1s ratio peak intensity changes after sputtering and heating.	63
Table 8. Measured thorium binding energy compared to previously reported values.....	64
Table 9. Resolution (RES) of the Th 4f _{7/2} peak before and after sputter etching.	75
Table 10. AFM adhesion force measurements on ThO ₂	78
Table 11. Estimated interface energy of metal to ThO ₂ crystal.....	81
Table 12. The change in estimated interface energy values from the as-grown to the cleaned crystal.....	82

List of Acronyms

Abbreviation	Page
AFM.....Atomic Force Microscopy	5
Al.....Aluminum	32
Al ₂ O ₃Aluminum Oxide	1
Ar ⁺Argon ion	27
Au.....Gold.....	4
CMOSComplementary Metal Oxide Semiconductor	1
COCarbon monoxide.....	61
CO ₂Carbon dioxide.....	61
CsCesium	47
(k)eV (kilo) Electron-Volt.....	1
FCCFace Centered Cubic	2
FFluoride	47
FWHMFull Width Half Max.....	40
H ₂ OWater.....	5
HfO ₂Hafnium Dioxide	1
InIndium	4
IR.....Infrared Spectroscopy	87
LEEDLow Energy Electron Diffraction	87
Li ₂ O.....Lithium Oxide.....	49
MgMagnesium.....	39
MOSMetal Oxide Semiconductor	1
MOSFETMetal Oxide Semiconductor Field Effect Transistor	1
Ni.....Nickel	4
PES.....Photoemission Spectroscopy	22
SEMScanning Electron Microscopy	85
SiO ₂Silicon Dioxide	1
TaTantalum	38
ThO ₂Thorium Dioxide.....	2
Ti.....Titanium.....	4
TOF-SIMSTime of Flight- Secondary Ion Mass Spectrometry.....	20
UPSUltraviolet Photoemission Spectrometry	22
XPSX-ray Photoemission Spectroscopy	22

List of Symbols

Abbreviation		Page
A.....	Unit cell length.....	8
B	Dipole-induced dipole interaction constant	9
c	Speed of light	24
C	Material interaction constant.....	7
C_i/C_f	Wave function constant initial/final.....	23
d.....	Distance tip extends into water	11
D.....	Distance from AFM tip to crystal surface.....	5
E(eV).....	Energy of sputtering ions	18
E_{binding}	Binding energy of electron in crystal lattice	26
E_c	Energy of Conduction Band.....	27
E_F	Energy of Fermi level	27
E_{KE}	Kinetic energy of ejected electron	26
E_{th}	Sputtering threshold energy	18
E_v	Energy of Valence band.....	27
E_{vac}	Energy of Vacuum level	27
ΔE	Energy resolution of XPS peak.....	40
ΔE_a	Energy resolution of electron analyzer	40
ΔE_n	Energy resolution of photo electric emission.....	40
ΔE_p	Energy resolution of excitation source	40
f	Resonance frequency of AFM cantilever	17
$f(Z)$	Force component from all atoms	14
F(D).....	Force at distance D.....	14
F_{adh}	Total force of adhesion	6
F_{cap}	Capillary force	6
F_{cont}	Contact force	6
F_{es}	Electrostatic force	6
F_{vdW}	Van der Waals forc	6
h.....	Intensity of XPS peak (height).....	40
H.....	Hamaker constant.....	7
$h\nu$	Energy of X-rays.....	26
I	Ion beam current	22
j.....	Total angular quantum number.....	24
J	Total angular quantum state.....	24
l	Orbital quantum number	24
L	Orbital quantum state	24
k_c	Spring constant of AFM cantilever.....	16

k_e	Lindhard electronic stopping coefficient	19
M_1/M_2	Mass of atom 1 and atom 2	18
M_m	Molar Mass	22
N	Number of electrons	22
N_A	Avagadro's number	22
p/p_0	Relative vapor pressure	10
q	Charge on atom or molecule	9
$Q(z)$	Fit parameter by Yamamura	18
R	Radius	23
\vec{r}	Radial vector of wavefunction	23
r_K	Kelvin radius of meniscus	10
r_{mc}	Radius of meniscus curve	10
r_{mr}	Radius of small meniscus curve	10
R	Ideal gas constant	10
R_t	Radius of the tip	10
$R_{t,eff}$	Effective radius of the tip	58
R_1, R_2	Radius of surface 1 or surface 2	14
RES	Resolution of XPS peak	40
s	Exponent fit parameter for sputtering yield	18
s	Spin quantum number	24
S	Spin quantum state	24
S^n_{TF}	Thomas-Fermi potential based on reduced mass energy	19
$S^n(E)$	Nuclear stopping power	19
t	Sputtering time	22
T	Temperature	10
U_s	Surface binding energy	19
$V(r)$	Potential energy at radius	24
Vol	Volume	22
W_{12}	Work required to remove surface 1 from surface 2	14
W_{132}	Same as W_{12} , but in presence of surface 3	14
W_z	Fit parameter for electronic stopping power	19
X	Distant of atom interaction	13
x_c	Distance cantilever deflects	16
x_d	Distance laser deflects on photon detector	17
$Y(E)$	Sputtering yield	18
Z	Distance from surface of crystal inward	14
A	Sputtering angle	20
α^*	Fit value for reduced mass ratio	18
$\alpha_{1,2}$	Angle of laser beam	17

ϵ_0	Permittivity of free space	9
γ	Energy transfer coefficient for elastic collision	20
γ_1, γ_2	Surface energy of surface 1 and surface 2	15
γ_I	Interface surface energy	15
γ_L	Capillary force energy	10
γ_T	Computed residual interface energy	57
γ_{tw}	Interface energy of metal tip with water adsorbed	15
γ_{cw}	Interface energy of ThO ₂ crystal with water adsorbed	15
γ_{ct}	Interface energy of metal tip on ThO ₂ crystal	15
Γ	Fit parameter of the electronic stopping power	18
ϕ_i/ϕ_f	Wave function of electron that will be ejected	23
ϕ_{sys}	Work function of system	26
ρ	Mass density of material	22
θ	Meniscus angle between crystal and metal	10
ψ_i/ψ_f	Wave function of electrons	23
ϵ	Reduced mass energy	20

SURFACE GEOMETRY AND CHEMISTRY OF HYDROTHERMALLY SYNTHESIZED SINGLE CRYSTAL THORIUM DIOXIDE

I. Introduction

1.1 Research Motivation: ThO₂ as a Potential Oxide Layer in Electronic Devices

Metal oxide silicon (MOS) devices are essential to most modern electronics, such as MOS field effect transistor (MOSFET) and complementary MOS (CMOS). The electronics industry is attempting to develop smaller, faster and more efficient electronics. However, some smaller electronics are more susceptible to dielectric or channel breakdown resulting in device failure [1]. A device with a high dielectric constant solves these problems.

SiO₂ is the standard oxide layer material and has reached its physical limit due to its relatively small dielectric constant. To solve this problem, researchers are investigating highly resistive materials with band gaps in excess of 6 eV and possessing dielectric constants greater than SiO₂ (3.9). Al₂O₃, HfO₂, and Zr_xSi_{1-x}O₂ match these criteria and have demonstrated promise as a replacement for SiO₂ [1, 2]. However, each of these materials has unique challenges. For instance, HfO₂ has been thoroughly researched in the past decade, including studies of radiation effect on HfO₂ MOS devices

[3, 4]. These devices performed poorly due to large defect concentrations derived from poor crystal growth.

ThO_2 could be a candidate to replace SiO_2 in MOS devices, possessing similar physical and electrical properties as HfO_2 . Listed in Table 1 are some properties of ThO_2 , HfO_2 , and SiO_2 that are useful in making electronic devices. For example, one critical electronic property relevant to gate oxide performance is the electronic band gap. One theoretical calculation determined the band gap of ThO_2 to be 4.6 eV [2]. However, recent experimental work on ThO_2 single crystal, determined a band gap between 6-7 eV with a smaller, functional optical band gap due to the impurities and occlusions in the single crystal [5].

Table 1. Useful properties of SiO_2 , ThO_2 , and HfO_2 .

Property	ThO_2	HfO_2	SiO_2
Unit Cell	FCC	Monoclinic	Tetrahedral
Lattice Constant (\AA)	5.59[5]	5.08[2]	4.18[6]
Density (g/cm^3)	9.6[7]	9.68[8]	2.533[8]
Melting Point ($^\circ\text{C}$)	3640[7]	2774[8]	1710[8]
Work Function (eV)	2.6[9]		
Band Gap (eV)	6-7[5]	5.65[10]	8.9[11]
Dielectric Constant	18.9[12]	22[10]	3.9[11]

Despite the consideration of ThO_2 as a replacement for SiO_2 , many of its properties remain uncertain such as: the expected density of charge carriers, suitable ohmic contacts, break down voltages of potential oxide layers, and performance in radiation hardened electronics. Yet, answering these questions requires the adhesion of a metal contact to the ThO_2 surface. Once the surface properties of ThO_2 are understood, an acceptable metal can be chosen as contact material. A methodical, systematic

approach to analyzing the crystal surface is needed to generate the necessary chemical and geometric information for this assessment.



Figure 1. Crystal 8a grown by the hydrothermal growth technique. This is the crystal used for all experiments.

The crystal used in this experiment was grown by hydrothermal growth techniques via spontaneous nucleation. The experiment was conducted on crystal 8a depicted in Figure 1. Furthermore, the experimental methodology used to study ThO₂ applies to the study of future UO₂ single crystals. UO₂ has potential as a semiconducting material and its electrical properties need to be studied. The surface geometry and surface chemistry of UO₂ also require investigation. The methodology developed in this thesis can thus be used for future UO₂ studies.

1.2 Research Objectives

The objective of this research is to systematically investigate the surface chemistry and geometry of ThO₂. The goal of the research is to determine the “best” metal to apply as a contact to ThO₂. The adhesion of a metal to the ThO₂ crystal surface

requires a detailed study of the surface of ThO₂. Two surface properties directly contribute to a metal's performance as a suitable contact: the magnitude of the attractive force of each metal to the surface of ThO₂ and the concentration and type of surface impurities. The methodology includes determining how the surface properties of ThO₂ change as the surface impurities and defects are eliminated. The method for removing the impurities and defects includes chemical cleaning, sputter etching with argon ions, heating, and dehydration. Understanding these properties will then allow a selection of a proper metal to use as a contact from the four metals chosen to study: gold, indium, nickel, and titanium.

II. Theory

2.1 Description of the Four Forces that Comprise the Adhesion Force

Adhesion is the attractive force, F_{adh} , of molecules and atoms with other molecules and atoms. It can be measured by atomic force microscopy (AFM). For all adhesion force and surface energy computations in this document, the surface interaction resembles a sphere (the AFM tip) touching a plane (the ThO₂ crystal surface). In reality, the AFM tip is not perfectly spherical nor is the ThO₂ surface perfectly flat as depicted in Figure 2. However, the aforementioned assumptions do not diminish significantly the first order approximation used to understand the physical processes in this research.

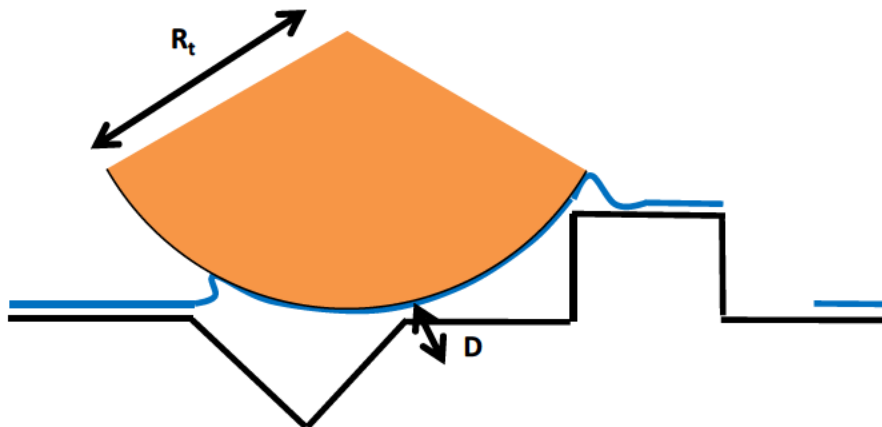


Figure 2. AFM tip radius, R_t , and the distance, D , from the ThO₂ crystal surface. The AFM tip is orange, the ThO₂ surface is black, and H₂O is blue. The tip radius, R_t , is provided by the manufacturer as the radius of curvature of the bottom of the tip. The distance, D , from the tip to the surface is estimated to be near zero when the tip applies a contact force, F_{cont} . This diagram is of a hydrophilic metal tip with the water wetting.

The adhesion force is a combination of multiple underlying forces, four of which are considered [13]: the van der Waals force, F_{vdW} , the electrostatic force, F_{es} , the capillary force, F_{cap} , and the contact force, F_{cont} .

$$F_{adh} = F_{vdW} + F_{es} + F_{cap} - F_{cont} \quad (1)$$

2.1.1 The Dispersion Forces, F_{vdW}

Dispersion forces and dipole forces are combined into one term: the van der Waals force, F_{vdW} . Dispersion forces are an attractive force that is dependent on the polarizability of the atoms involved. The van der Waals force decreases with distance D on the order of D^{-2} . An instantaneous dipole gives rise to a momentary local electric field which induces additional dipoles in adjacent atoms, giving rise to more dipoles. This electric field propagates, and the original dipole field is dispersed throughout the medium. The resultant dispersive force acts to attract the atoms and molecules together.

The polarizability of atoms or molecules determines how large the attractive force is and how far the dipole disperses. Because the ThO₂ oxidation state is +2.47 rather than +4 [14], the momentary polarizability of oxygen in ThO₂ is different from the momentary polarizability of metallic thorium. No matter the oxidation magnitude, as an ionic species, the thorium has fewer electrons than protons which are pulled closer to the nucleus, increasing the overall electron density. This leads to rigidity in the electron cloud movement. Conversely, oxygen has the -2 oxidation state allowing the outer electrons to be shielded from the nucleus by other electrons. These outer electrons are easily polarizable. Thus, the ThO₂ surface polarizability depends on which atoms terminate the surface.

For a sphere and a flat plane the van der Waals force can be estimated by the empirical relationships

$$F_{vdW} \approx \frac{HR_t}{6D^2}, \text{ and} \quad (2)$$

$$H = \pi^2 C \rho_1 \rho_2, \quad (3)$$

where R_t is the radius of a sphere, D is the distance between the sphere and a flat plane, and H is the Haymaker constant, which does not change for a given material under static conditions. The material density is ρ , and C is the interaction constant (London constant) [15]. The van der Waals force and the Haymaker constant depend on the metal and the crystal face features.

2.1.2 The Electrostatic Force, F_{es}

The electrostatic force, F_{es} , originates from the Coulombic attraction of positive and negative atoms. Static and non-static charges (example: dipoles and induced dipole), bond using this force. ThO_2 has a natural dipole due to the difference in electronegativity of the atoms where thorium is positively charged and the oxygen is negatively charged. The ThO_2 crystal structure generates a dipole on the surface. ThO_2 has a fluorite crystal structure ($Fm\bar{3}m$ [2]), with a lattice constant of 5.599 Å [16]. The fluorite structure $Fm\bar{3}m$ means the crystal is face centered cubic with a fourfold mirror rotation in the (110) and (100) face and three fold rotation in the (111) face. Figure 3 depicts the ThO_2 (111) face with the oxygen (red) in a slightly higher plane than the thorium ions (blue).

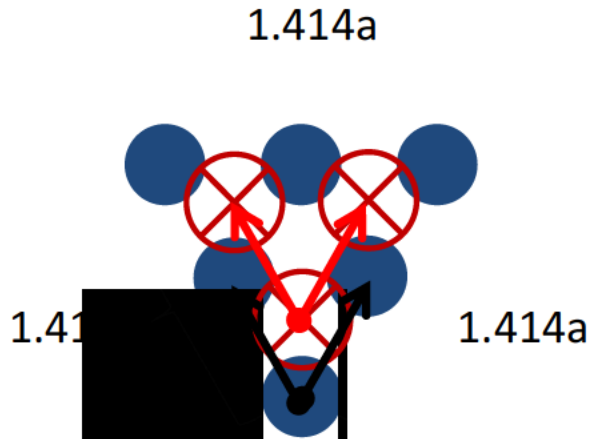


Figure 3. The (111) crystal face of ThO_2 . Red circles are oxygen while the blue circles are thorium. The size of the atoms based on Pauling ionic radius and spacing of the atoms are nearly to scale. As depicted, the oxygen atoms are on the outside layer and the thorium atoms are on the inside.

Based on empirical surface potentials, the oxygen atoms near the surface tend to shift towards the surface and the thorium atoms shift towards the bulk [12]. Thus, oxygen should be on the (111) surface [9]. With the negative charge on the surface and a positive charge towards the bulk, a permanent dipole is established on the (111) surface. Since the (111) surface is the most stable [12, 17], i.e. it has the lowest surface free energy, it potentially has a lower adhesion force. The theorized crystal face of ThO_2 should have a dipole and generate an induced dipole in the AFM metal tip upon contact.

As an atom approaches the crystal surface, the surface dipole will repulse the atom's electron cloud and induce a dipole with the partial positive charge facing the negative dipole of the crystal surface. The negative dipole charge on the surface and positive charges on the dipole of the atom's electron cloud provide an attractive force.

Assuming a point source, Coulombic forces decrease by D^{-2} as in Coulomb's law,

$$F_{es} = \frac{q_1 q_2}{4\pi\epsilon_0 D^2}, \text{ but dipole induced-dipole forces decrease by } D^{-6} [18],$$

$$F_{es} = \frac{B}{D^6}, \quad (4)$$

where q is the surface charge, ϵ_0 is the permittivity of free space, and D is the distance between the surfaces [19]. B is a constant that includes metrics for surface free energy of the dipole and induced dipole, the polarizability of the induced dipole, geometric term for the dipole angle in relation to the surface, and the dielectric strength of the medium between the surfaces. As the atom move farther from the dipole, the dipole induces a smaller effective dipole in the adjacent atom, which further reduces the force. Thus, an increase in distance, D , has a greater affect on the attractive force and D^{-2} for Coulomb's law becomes D^{-6} for dipole induced-dipole forces.

The metal tips used in this research are electrically neutral and assumed to be mostly free of oxidation. Therefore the tips do not have a dipole force. Besides the induction of a dipole at the atomic level, the surface dipole of the ThO₂ crystal attracts positive electric charge to the surface of the metal. The Coulombic force, F_{es} , varies with each metal's polarizability and electrical resistance, and it will change the total adhesive force.

Additionally, hydrogen bonding is included as a capillary force in Equation 8. Because of the ThO₂ molecular dipole, hydrogen bonding is expected to contribute significantly to the total force.

2.1.3 The Capillary Force, F_{cap}

The capillary force, F_{cap} , is due to water and humidity creating a meniscus from the AFM tip to the crystal surface. The hourglass shaped meniscus has a high surface tension that pulls the tip towards the crystal minimizing the energy of the system. The Kelvin equation gives the relationship between radii of the meniscus and physical constants of the materials involved [13, 20]

$$r_K = \frac{1}{\frac{1}{r_{mc}} + \frac{1}{r_{mr}}} = \frac{\gamma_L Vol}{RT \log(\frac{p}{p_0})}, \quad (5)$$

where r_K is the Kelvin radius, r_{mc} is the radius of the meniscus curve, r_{mr} is the smallest radius of the meniscus hourglass, γ_L is the surface tension of water, Vol is the volume of the water, p/p_0 is the relative vapor pressure of water, and RT is the gas constant and temperature. The Kelvin radius is a constant for a given material system.

The relative humidity is related to the relative vapor pressure in Equation 5 [13]. As the relative humidity increases, the volume of water in the meniscus increases, and vice versa. As humidity decreases water remains in the crystal defects that are smaller than the Kelvin radius [13].

The hydrogen bonding capability of water generates a capillary force that has a longer range than the other forces in this model because it decreases as D^{-1} . The capillary force can be computed by the approximation [13, 15]

$$F_{cap} \approx \frac{4\pi R_t \gamma_L \cos \theta}{1 + \frac{D}{d}}, \quad (6)$$

where θ is the contact angle of water from the surface and d is the distance the tip extends into the water bridge. For the AFM measurements, if the distance of the tip to the surface, D , and the radius of the tip, R_t , are the same, the only parameters depend on the AFM tip metal are the angle of meniscus, θ , and the surface tension of the water to the adhesion metal, which is included in the term, γ_L . An increase in the affinity of the metal towards water increases the meniscus angle, as diagrammed in Figure 4. The increase in meniscus angle generates a larger capillary force. A meniscus angle of 90° means that the tip is hydrophobic and has no associated capillary force.

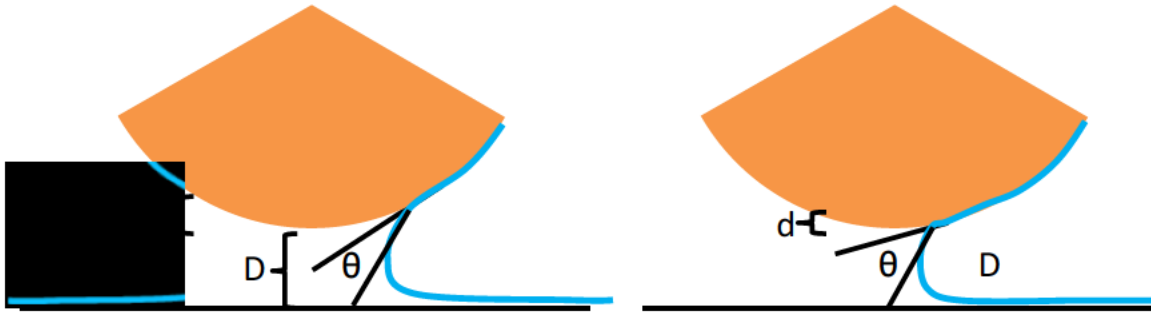


Figure 4. Diagram of the influence of the capillary force on water adhesion in an AFM measurement. The AFM tip is shown in orange, the ThO_2 surface is in black, and the water is in blue. To show detail, this diagram is not proportional.

The crystal face also affects the capillary force in a fashion similar to the dipole induced-dipole force. The dipole of ThO_2 varies based on whether the Th or O is on the surface of the (111) or (100) face. Water will align the hydrogen to the electronegative oxygen in a hydrogen bond [17], and the water oxygen will align with the thorium. This alignment of the water reduces the dipole normal to the surface [17], but the water still propagates the dipole. The ThO_2 dipole faces normal to the surface for the (111) and (100) face, however for the ThO_2 (110) face, the Th and O atoms are in the same plane

and the dipole vector is parallel to the surface. Thus the capillary force should be different based on the exposed surface face. According to Eastman, the capillary force is affected by the wetting of water to the substrate and of water to the tip [15]. The capillary force decreases as the tip becomes more hydrophobic [15]. The hydrophobic nature of the metal and crystal affects the magnitude of the capillary force as does the crystal face of the ThO₂.

2.1.4 The Contact Force, F_{cont}

The contact force, F_{cont} , displaces atoms of the crystal lattice from their equilibrium lattice locations. For AFM measurements, the F_{cont} is directly proportional to the tip radius and the depth that the tip penetrates into the surface. As the tip penetrates and deforms the surface (and the surface deforms the tip), the effective radius and the adhesion force increases. This assumes that the deformation causes the tip and surface to match geometry, which increases the number of atoms or molecules participating in adhesion. This deformation can be elastic or plastic. The adhesion force and surface energy models listed do not include deformation of the crystal or tip. This force only has magnitude when the tip is compressed into the surface. Once the tip is above surface, F_{cont} is zero.

2.2 Description of Surface and Interface Energy

All crystal surfaces have dangling bonds, surface dipoles, or other highly energetic states. To reduce the resulting free energy, either the crystal lattice distorts or the crystal adsorbs atmospheric contaminants. In processing, the surface contamination

can be controlled by applying a suitable surface interface material. Each surface must satisfy the dangling bonds, surface dipoles, and high energy states of the other surface.

When two surfaces are in contact, as in the case of an AFM metal tip to a surface, only a finite area actually touches. The area of contact is not well described since both surfaces may have plastic deformation and neither are perfect spheres or planes. However, to understand the surface energies, the ideal case of two perfect spheres touching is considered the best starting point, as in Figure 5. The force, $F(D)$, between two spheres is described by [19]

$$F(D) = 2\pi \int_{Z=D}^{Z=\infty} xf(Z)dx . \quad (7)$$

Z runs through the center of the sphere and the x axis is perpendicular to the z axis, $f(Z)$ is the force of all the atoms in sphere 2 acting upon one spot on sphere 1, D is the distance between the two spheres, and x is the radial distance from the center of a ring that bisects

the sphere as diagrammed in Figure 5. Since $Z = D + z_1 + z_2 = D + \frac{x^2}{2} \left(\frac{1}{R_1} + \frac{1}{R_2} \right)$, then

$$dZ = \left(\frac{1}{R_1} + \frac{1}{R_2} \right) x dx [19]. \quad \text{The increment } dZ \text{ is the depth of the bisecting ring and } dx \text{ is}$$

the increment of width of the bisecting ring, z_1 is the depth in sphere 1 along the Z axis that the force acts upon, and z_2 is the depth of the bisection ring in sphere 2.

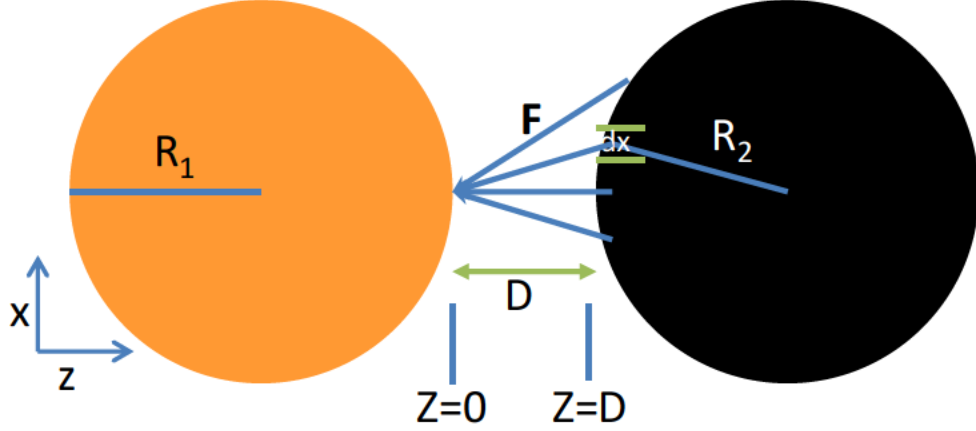


Figure 5. Diagram of the adhesion forces acting at one location. The black sphere is divided into concentric rings about the z axis. The width of those rings is dx . This area applies a force towards a single point on the opposite sphere. Summing the contribution of these forces in the z direction gives the total adhesion force.

If the spheres have radii of R_1 and R_2 , the computation of the integral approximates to

$$F(D) \approx 2\pi \left(\frac{R_1 R_2}{R_1 + R_2} \right) W_{132}(D). \quad (8)$$

However, the ThO_2 crystal is better represented as a plane rather than a sphere, so

as R_2 approaches infinity, $\frac{R_1 R_2}{R_1 + R_2} \rightarrow R_1$. Using the work-energy theorem, the work done

on the system to remove the sphere from the plane is equal to one half the surface energy of an individual surface [19]. The maximum non-capillary force, $F_{non-cap}$, computed is when $D = 0$

$$F_{non-cap} = 4\pi R_1 \gamma_I. \quad (9)$$

Thus the force of adhesion is directly related to the radius of the sphere and the interface energy of the system, γ_I . More specifically; the tip is surface 1, the crystal is surface 2, and the water/vapor is surface 3 as in Figure 6.

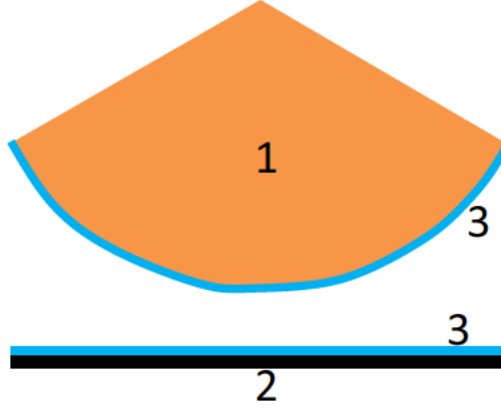


Figure 6. Diagram of the surface labels for the AFM tip, ThO₂ surface, and water. The AFM metal tip is orange, ThO₂ surface is black, and water is blue. The water on the surface reduces the interface energy available for further adhesion force.

The interface energy based on separating two surfaces in the presence of a third media is the sum of the surface energies involved and is described by [19]

$$\gamma_I = 2W_{tc} = \gamma_{tw} + \gamma_{cw} - \gamma_{tc}. \quad (10)$$

The interface energy is a combination of the residual interface energy of the tip covered by water, γ_{tw} , plus the residual interface energy of the crystal covered by water, γ_{cw} , minus the residual interface energy that remains after the tip contacts the crystal, γ_{tc} . This equation can be further subdivided to account for the original surface energy of the unadulterated surface. By removing the work required to separate the satisfied surface, the Dupre equation applied [19]

$$\gamma_{12} = \gamma_1 + \gamma_2 - W_{12}, \quad (11)$$

where γ_1 and γ_2 are the surface energies of a pure surface and W_{12} is the work required to separate surfaces 1 and 2. Equation 11 applies to the water on the metal tip, γ_{tw} , water on the crystal surface, γ_{cw} , and for the metal tip on the crystal surface, γ_{tc} as in Equation 10.

The values of γ_t , the surface energy of the metal tip, γ_c , the surface energy of the crystal and γ_w , the surface energy (tension) of water, are material properties which do not change under this research's conditions. For instance, in the case of the interface energy of the metal tip to water- γ_{tw} , γ_t and γ_w do not change. However, W_{tw} is a function of the humidity, and the amount of water available to reduce the surface energy. The water on the surface satiates the dangling bonds and dipoles of the tip and crystal, thus reducing the surface energy to the residual interface energy, γ_{12} .

Capillary forces also contribute to the surface energy relaxation of a material. There are up to three bilayers of water and hydroxyl groups on the surface of ThO₂ [7] and even a clean surface becomes hydroxylated in a humid environment [17]. The force of adhesion for the surface surrounded by a vapor is specified by [19]

$$F_{cap} = 4\pi R_t \gamma_L \cos \theta, \quad (12)$$

where γ_L is the surface tension of water and θ is the contact angle of the water.

Equation 12 assumes similar capillary adhesion response of the water to the crystal and to the AFM tip.

2.3 AFM Adhesion Measurement and Cantilever Spring Constant Calibration

The adhesion force of metals to the ThO₂ is measured by the deflection of a cantilever (Figure 7). The cantilever and tip operate as a simple spring that is governed by Hooke's law,

$$F_{adh} = k_c x_c. \quad (13)$$

As the tip deflects, the location of the laser spot on the photodetector changes. The spring constant of the cantilever, k_c , cannot be directly measured; the cantilever is tens of microns long.

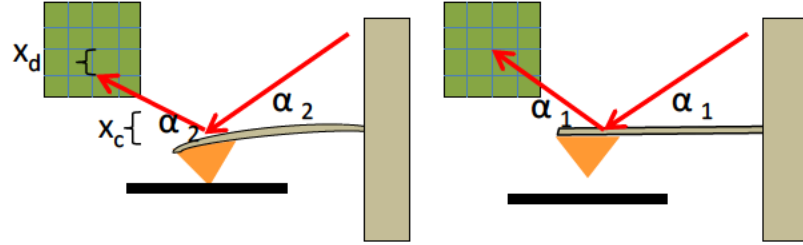


Figure 7. AFM tip and cantilever deflects a distance due to adhesion force. The diagram on the right is the AFM system at rest. The diagram on the left is the adhesion of the tip to the crystal surface causing cantilever deflection. The adhesion force of the metal tip, orange triangle, to the ThO₂ surface, black, causes the tip and cantilever to deflect. This deflection causes the laser, red arrow, to reflect off the back side of the cantilever at a different angle, α_2 instead of α_1 . The distance of travel on the detector, x_d , corresponds to the deflection of the cantilever, x_c .

Based on the motion of a simple harmonic oscillator, the resonance frequency of the cantilever, f , is proportional to the square root of the spring constant,

$$2\pi f = \sqrt{\frac{k_c}{m}}. \quad (14)$$

The AFM measures the deflection of the cantilever, x_c , using a laser and photodetector. In Figure 7, as the cantilever bends, the laser spot changes location on the photo detector. The amount of change in the location on the photodetector, x_d , is directly proportional to the amount of deflection in the cantilever, x_c .

2.4 Sputter Etching of Crystals with Ions

Sputter etching is the process of physically removing atoms or clusters from a surface by a mechanical process. Normally, ionized particles accelerated by an electric field bombard the surface to be sputtered. The ion transfers its kinetic energy to the crystal overcoming the adhesive forces of the surface. Typically, the ionized atoms are noble gases due to their simple geometry, chemical inertness, and ionization simplicity.

Incoming ions interact with the surface by ballistic spalling and penetration, followed by energy deposition and release [21]. The first process is a direct transfer of energy from the incoming ion to the crystal lattice, resulting in atoms departing the crystal surface. In the second process, the incoming ion transfers energy to the crystal lattice, adding additional phonon energy, and releasing more atoms from the surface.

Yamamura and others presented a semi-empirical method to determine the sputtering rate of monatomic crystal surfaces with accelerated ions [21]. The method is based on the Thomas-Fermi potential of atoms and the nuclear stopping power of individual lattice atoms for the incoming ion [21]. Equation 15 is the central equation describing the sputtering yield, $Y(E)$, as a function of energy of the incoming atoms,

$$Y(E) = 0.042 \frac{Q(z_2)\alpha^*(M_2/M_1)}{U_s} \frac{S_n(E)}{1 + \Gamma k_e \epsilon^{0.3}} \left[1 - \sqrt{\frac{E_{th}}{E(eV)}} \right]^s, \quad (15)$$

Q and s are dimensionless fitting parameters, E_{th} and $E(eV)$ are the sputtering threshold energy and the sputtering energy respectively. The fit value α^* is the reduced mass ratio described by

$$\alpha^* = 0.249 \left(\frac{M_2}{M_1} \right)^{1.56} + 0.0035 \left(\frac{M_2}{M_1} \right)^{1.5}. \quad (16)$$

M_2 and M_1 are the mass of the target atom and bombarding ion respectively, U_s is the surface binding energy, $S_n(E)$ is the nuclear stopping power described by

$$S_n(E) = \frac{84.78Z_1Z_2}{(Z_1^{2/3} + Z_2^{2/3})^{1/2}} \frac{M_1}{M_1 + M_2} s_n^{TF}(\epsilon). \quad (17)$$

The nuclear stopping power is based on the Thomas-Fermi potential, $s_n^{TF}(\epsilon)$, which relates the nuclear potential well of the nucleus and the mass ratios, M_2 and M_1 , of the bombarding ions. The number of protons in the nucleus, Z_1 and Z_2 , dramatically increase the stopping power due to the increased nucleus size and increased interaction potential energy. The Thomas-Fermi potential is based on the reduced energy ϵ and is given by

$$s_n^{TF} = \frac{3.441\sqrt{\epsilon} \ln(\epsilon + 2.718)}{1 + 6.355\sqrt{\epsilon} + (6.882\sqrt{\epsilon} - 1.708)}. \quad (18)$$

For crystal atoms larger than the bombarding atoms,

$$\frac{E_{th}}{U_s} = \frac{1 + 5.7(M_1 / M_2)}{\gamma}, \quad (19)$$

describes the relationship between the threshold sputtering energy, E_{th} , surface binding energy, U_s , and γ the energy transfer factor for an elastic collision. The Γ is a fit parameter for electronic stopping power described by

$$\Gamma = \frac{W_{Z_2}}{1 + (M_1 / 7)^3}, \quad (20)$$

where W_{Z_2} is a fit parameter that correlates to a fraction of the surface binding energy, U_s [21]. In Equation 15, k_e is the Lindhard electronic stopping coefficient given by

$$k_e = 0.079 \frac{(M_1 + M_2)^{3/2}}{M_1^{3/2} M_2^{1/2}} \frac{Z_1^{2/3} Z_2^{1/2}}{(Z_1^{2/3} + Z_2^{2/3})^{3/4}}. \quad (21)$$

The stopping coefficient is simply a reduced mass and reduced charge relationship. The reduced energy ϵ is given by

$$\epsilon = \frac{0.03255}{Z_1 Z_2 (Z_1^{2/3} + Z_2^{2/3})^{1/2}} \frac{M_2}{M_1 + M_2} E(eV). \quad (22)$$

Z_1 and Z_2 are the atomic numbers of the bombarding ion and the crystal atom respectively

$$\gamma = \frac{4M_1 M_2 \cos^2(\alpha)}{(M_1 + M_2)^2} \quad (23)$$

The cosine component in Equation 23 accounts for the angle with respect to the surface normal. It reduces the energy deposited based on the conservation of energy and momentum of an elastic collision. With a known crystal lattice and bombarding ion, only the surface binding energy of the crystal, U_s , and the three fit parameters, Q , W , and s are unknown. The sputtering yield $Y(E)$ can then be plotted as a function of the bombarding ion energy $E(eV)$, as in Figure 8.

It is essential to realize that Yamamura's empirical formula is designed for an ion bombarding a monatomic crystal, which ThO_2 is not. When sputtered, ThO_2 crystal could emit various clusters such as Th , ThO^{2+} , ThO_2 , O_2 , O etc. as ejected material. To simplify the calculation, only ThO_2 is considered to be ejected and will be treated as a single atom. However, time of flight- secondary ion mass spectrometry (TOF-SIMS) confirms the ejection of the various other clusters [22].

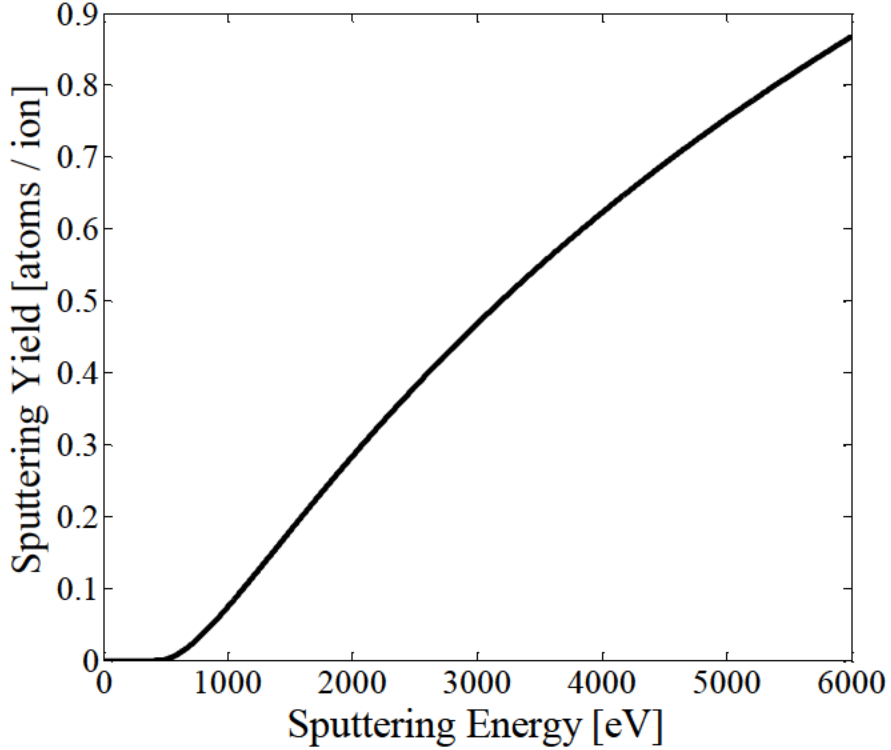


Figure 8. Sputtering yield of ThO_2 verses sputtering energy of bombarding Ar^+ . Parameters used for this plot are U_s - 6.98 eV, Q - 0.63, W - 2.443, s - 2.5, M_2 - 264, and Z_2 - 106. The bombarding angle is 75° from the normal. Sputtering energies of less than 500 eV have minimal sputtering yield.

Based on a parameter study, W_{Z2} from Equation 18, has little influence on the sputtering yield because most of the energy transfer occurs through the nuclear stopping power, $S_n(E)$ and not the electronic stopping power, Γ [21]. The Q value was assumed to be similar to the Q value for thorium metal. For most metals, s is 2.5 [21]. The value of the ThO_2 surface binding energy, U_s , from Equation 22 is not provided by Yamamura. However, Yamamura's surface binding energy is nearly equivalent to the sublimation energy. ThO_2 's sublimation energy is 6.98 eV/atom [7] and is used for the surface binding energy. Consequently, Figure 8 is a plot of the sputtering yield of ThO_2 verses sputtering energy of Ar^+ at 75° to the normal. The yield is insignificant at sputtering

energies less than 500 eV. The yield is mostly linear from 1000 eV to 5000 eV, which is the operating range of the ion gun used in this experiment.

From the sputtering yield of Yamamura's equations and based on the argon ion beam current from the sputtering instrumentation, the volume of sputtered material can be determined by

$$Y(I, t) = \frac{\rho N_A Vol}{ItM_m}. \quad (24)$$

N_A is Avogadro's number, ρ is the mass density of atoms, Vol is the volume of atoms sputtered, I is the current of bombarding ions in units of ions s^{-1} , t is the sputtering time, and M_m is the molar mass of ThO₂.

2.5 X-ray Photoemission Spectroscopy

Detailed quantum mechanical treatment of photoemission spectroscopy (PES) which includes X-ray photoemission spectroscopy (XPS), Auger electron spectroscopy (AES), and ultraviolet photoemission spectrometry (UPS) is complicated because it is a multibody, quantum mechanical, and time varying problem. The electronic final state of the material, after photoemission, is different from the initial state of the material due to the missing photoelectron. The initial state is the product of the departing electron and the other remaining electrons [23]

$$\psi_i(N) = C_i \phi_{i,k} \psi_{i,R}^k(N-1), \quad (25)$$

where $\psi_i(N)$ is all the initial electronic state, C_i is an antisymmetrizing factor, $\phi_{i,k}$ is the orbital of the soon-to-exit electron, and $\psi_{i,R}(N-1)$ is all the other electrons. Similarly, the final state, $\psi_f(N)$, is well described by the remaining bound electrons, $\psi_{f,R}(N-1)$, and the

wavefunction of the ejected electron, $\phi_{f,Ekin}$, times a constant, C_f which depends on the probability of the particular final state occurring. The equation for the final state is

$$\psi_f(N) = C_f \phi_{f,Ekin} \psi_{f,R}^k(N-1). \quad (26)$$

The transition matrix of the initial state to the final state is then

$$\langle \psi_f | \vec{r} | \psi_i \rangle = \langle \phi_{f,Ekin} | \vec{r} | \phi_{i,k} \rangle \langle \psi_{f,R}^k(N-1) | \psi_{i,R}^k(N-1) \rangle. \quad (27)$$

The Sudden Approximation Theory makes the simplifying assumption that there is no core-hole relaxation and the bound electronic wavefunction remains unchanged between the initial and final states [23]. Additionally, there will be a specific number of excited states for the remaining electrons when the ejected electron departs the crystal. A sum of the excited states is accounted for as

$$\langle \psi_f | \vec{r} | \psi_i \rangle = \langle \phi_{f,Ekin} | \vec{r} | \phi_{i,k} \rangle \sum_s \langle \psi_{f,s}^k(N-1) | \psi_{i,R}^k(N-1) \rangle. \quad (28)$$

The remaining sections of Chapter 2.5 describe the origins of XPS peaks.

2.5.1 XPS Shakeup Satellites of ThO₂

Critical to the binding energy of the electron is the final state of the remaining electrons as described in Equation 28 [23]. For ThO₂, the satellite peaks of Th 4f_{7/2} and 4f_{5/2} are formed from the shakeup of the thorium valence band states (7p, 7s, 6d, and 5f) and the oxygen 2p states [24, 25]. The inbound photon ejects the first electron and excites an additional electron to one of many possible bound states. The first electron's kinetic energy is reduced by the magnitude of the excited state transition. This loss in kinetic energy gives rise to multiple shakeup satellite peaks depending on the transition.

2.5.2 The XPS Spin-Orbit Splitting of Peaks

The angular momentum and spin quantum numbers describe an electric dipole generated from the revolution and rotation of electrons. Changes in the spin quantum number causes splitting in the energy states that is called spin-orbit energy coupling [26]. The total spin of the electronic state, J , is a combination of the orbital, L , and spin, S , quantum states. The change in energy of the states is directly proportional to the coupling of the these quantum states [26],

$$\Delta E = \frac{1}{2m^2c^2} \frac{1}{r} \frac{dV(r)}{dr} \vec{S} \bullet \vec{L}. \quad (29)$$

ΔE is the energy of the system, m is the mass of the electron, c is the speed of light, r is the radial distance of the electron from the nucleus, and V is the electric potential of the electron. Since $J = j(j+1)$, $L = l(l+1)$, and $S = s(s+1)$, where j , l , and s are the specific quantum numbers associated with the quantum state, then the expectation value of the change in energy $\overline{\Delta E}$ becomes [26]

$$\overline{\Delta E} = \frac{\hbar^2}{4m^2c^2} [j(j+1) - l(l+1) - s(s+1)] \overline{\frac{1}{r} \frac{dV(r)}{dr}}. \quad (30)$$

Thus, an energy difference is expected with different orbital quantum numbers l , and quantum numbers s .

The electron spin s is either $\pm 1/2$. The orbital angular momentum l depends on the character s ($l = 0$), p ($l = 1$), d ($l = 2$), and f ($l = 3$). The number of electrons, n , associated with each spin-orbit coupling j value is $n = 2j + 1$ and non-negative. Thus the s orbital can only have a total angular momentum of $1/2$. The p , d , and f type orbitals can be split further. The p orbital can have j values of $1/2$ and $3/2$, the d orbital values of $3/2$

and 5/2, and the f orbital values of 5/2 and 7/2. Assuming the detector response for electron energies is the same and that the electron cross section of the material is the same for the different electron energies, the area under the experimental XPS peaks should have the ratio calculated above depending on core electron angular momentum character. For example, the $p_{3/2}$ orbital peak will have twice the area of the $p_{1/2}$ orbital peak.

2.5.3 Chemical Shifts and Surface Sensitivity of XPS

Another concern with XPS interpretation is the chemical and electrical environment of the atomic electrons. The final, $\psi_{f,R}$, or initial, $\psi_{i,R}$ states of electron orbitals are influenced by nearby charged atoms. These atoms are electrically charged due to prior X-ray induced electron ejection. Thus positive charge can build up on the surface of nonconducting material [27]. The attractive charge changes the final state wavefunction, $\psi_{f,R}$, and the binding potential, V , from Equation 29 and 30 respectively. This is called a core-hole relaxation [23]. This affects the final state energies and causes a shift in the binding energies.

Secondly, atoms in a crystal are bonded through metallic, ionic, or covalent bonds. For ionic bonds and covalent bonds with electronegative atoms, the atom that is oxidized has fewer orbital electrons than nuclear charge and thus has a larger attractive force on the outer electrons. This increases the remaining electrons' binding energies, shifting the XPS spectrum peak. The atom's electrons are further shielded from the positive charge of the nucleus and the electronic orbital spread out, moving further from the nucleus. Thus the electrons require less energy to be removed from a molecule. A

positively charged ion's binding energy will shift to higher energies, and a negatively charged ion's binding energy will shift to lower energies when compared to a neutral atom [28]. For example, In thorium metal, Th $4f_{7/2}$ peak has a binding energy of 333.1 eV, whereas in ThO₂ the Th $4f_{7/2}$ peak is at 334.9, a shift of 1.8 eV [29].

2.5.4 From Electron Kinetic Energy to Electron Binding Energy

The electron analyzer in PES does not measure binding energies, but instead the kinetic energy of the escaped electrons. The binding energy must be calculated from the kinetic energy of the electrons and the incident photon energy. X-rays penetrate deeply into a material based on the attenuation coefficient of the constituent atoms. These X-rays of energy $h\nu$, excite electrons from their ground state orbital to the vacuum. If, the X-rays have more energy than the binding energy of the electron to the atom, E_{bind} , the ejected photoelectrons depart the atom with a certain kinetic energy E_k . However, the electron must also overcome the work function of the crystal. Additionally, the work function of the system, ϕ_{sys} , must be accounted for due to measurement of the photoelectron within the electron analyzer. However because the Fermi energies of the system and crystal are pinned, the difference in vacuum level must be subtracted from the electron kinetic energy as in Figure 9. The final relationship of these energies is

$$E_{KE} = h\nu - \phi_{sys} - E_{binding}. \quad (31)$$

XPS is a near surface technique. Due to the electron absorption and scattering cross section of ThO₂ crystal, only electrons near the surface will escape with the initial kinetic energy. Electrons liberated from the atoms deeper in the crystal are down scattered or can be recaptured by the crystal.

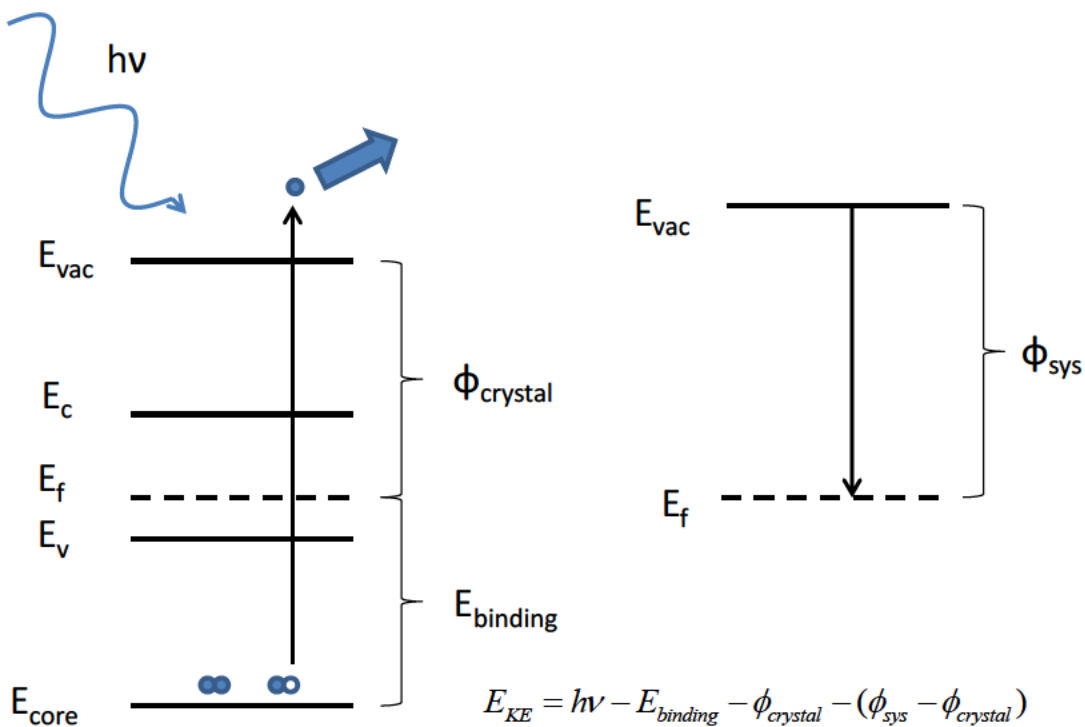


Figure 9. The schematic depicts the atomic binding energy levels for XPS. The incoming X-ray excites an electron out of the core orbital and exceeds the work function of the crystal $\phi_{crystal}$. The electron exits the crystal and travels towards the analyzer. The electron analyzer that has a work function, ϕ_{sys} . E_c is the energy of the conduction band, E_f is the Fermi energy, E_v is the energy of the top of the valance band, and E_{core} is the energy of a specific core level electron. The energy balance equation is simplified into Equation 31.

III. Methodology

3.1 General

The two techniques used for examining the geometry and chemistry of the ThO₂ surface are AFM and XPS. Two modes of AFM operation used: tapping mode surface scan and contact mode tip calibration adhesion probing. XPS was used to monitor the surface before, during, and after surface cleaning. To clean and smooth the surface three techniques were used: 1) Ar⁺ sputtering mechanically removed impurities and dislocated

edges and shelves, 2) resistive heating provided thermal energy to adsorbed atoms and molecules, and 3) a dry nitrogen flow removed adsorbed water layers. The general steps of the experimental process are depicted in Figure 10.

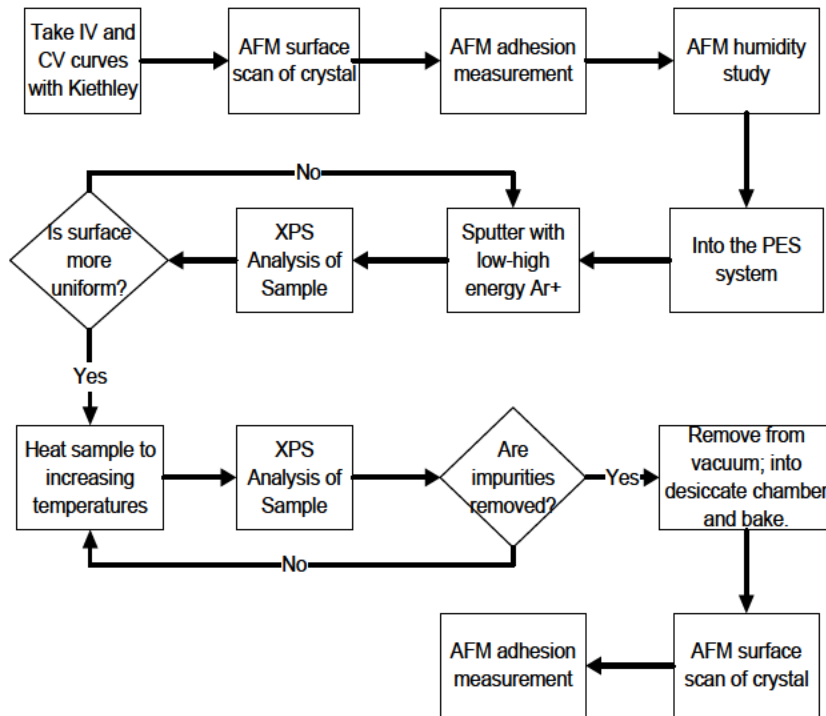


Figure 10. Process chart for determining geometry and chemistry of ThO_2 .

3.2 AFM Spectroscopy to Measure Adhesion Force and Surface Roughness

AFM measurements are designed to visually and quantitatively analyze the crystal surface roughness during the experiment. The AFM adhesion measurements were conducted before and after the ThO_2 crystal was sputtered and heated. The AFM multimode nanoscope requires the crystal to be mounted to a magnetic plate. For optimal measurement conditions and noise reduction, the crystal must be completely rigid with a flat surface on the plate and a parallel flat surface exposed to the AFM tip. Double sided

tape is affixed to the crystal and to the magnetic mounting plate. The AFM Multimode Nanoscope IIIa is controlled by software version V5.31r1.

The AFM is also used to analyze the adhesion force between the metal tips and the ThO₂ surface. AFM force calibration is not a standard operational mode; however, this calibration procedure can be used to monitor a tip's response to the surface during contact mode operations. The crystal is slowly raised towards the tip until contact and then slowly lowered. The flex in the cantilever is measured by the change in deflection of a laser off the back of the cantilever. For these measurements, the tip moves over a range of 500 nm with the photodetector collecting 512 samples for the extension of the tip, and 512 samples during the retraction of the tip. The tip travels the 500 nm in 0.5 seconds (1 Hz total oscillation) for a speed of 1.0 $\mu\text{m/s}$. Since all forces respond in the femtosecond range, much faster than the tip can move, the contact time of the tip to the crystal surface does not change the measured adhesion force [20]. The deflection setpoint, deflection sensor, and “z scan start” (Nanoscope IIIa parameter settings) varied with the surface location and type of tips. These settings were adjusted so that cantilever deflection into the crystal was only 25 nm, and the adhesion force sensitivity was maximized. The resonance frequency of each tip was measured five times and averaged.

The ThO₂ surface is not perfectly smooth, so a statistical approach to determining the adhesion properties of the metals to the surface was required. The AFM tip interacts with varying crystal surface features at different locations. To produce statistically significant conclusions, a grid pattern of 9 points, 5 microns apart, was determined. At each point, 5 measurements were taken at 2 second intervals. The exact procedure for measuring the adhesion is described in Appendix A. Also, because of these

imperfections, and due to the expected dipole on the surface of ThO₂, water adhered to the surface.

Each metal tip underwent the following procedures. First, the adhesion measurements were determined under atmospheric conditions. Then a 1 gallon plastic bag was placed over the AFM measurement device and loosely sealed at the bottom as in Figure 11. Dry nitrogen flowed into the bag at a rate of approximately 1.5 liters per minute for 30 minutes. The flow was fast enough to inflate the bag. The dry nitrogen flow was reduced to reduce vibrational noise in the AFM tip, but remained fast enough to achieve positive pressure on the bag and restrict water's reentry into the bag. Vibrational noise in the tip was assessed through the contact mode scope trace screen that plots the shudder and harmonics of the tip as it conducted a contact scan. These steps are repeated multiple times.



Figure 11. This AFM Setup with the dry nitrogen bag was used for adhesion measurements. Dry nitrogen is pumped into the plastic bag through a plastic tube. The dry nitrogen reduces the relative humidity and thus reduces the adsorbed water. Although water cannot be completely removed in this manner, a control of the relative humidity reduces the variability of laboratory humidity.

For each of the four metals (nickel, gold, titanium, indium) the humidity was measured before each run. The AFM software determined the total adhesion force measurement for each scan and a statistical computation of all the force measurements was made to compare the various metals.

Three criteria were proposed to investigate the suitability of a metal to serve as an ideal contact for ThO₂: work function, lattice spacing, and adhesion force. The work function of the metal must be smaller than or equal to the electron affinity of the crystal [11]. Lattice match increases the adhesion of the metal to the crystal and improves charge transfer from the metal to crystal. The adhesion force of the metal to the crystal is a direct measure of how well the metal adheres to the crystal. Although not critical, difficulty in applying the metal contact should be considered; vapor deposition of a high melting point metal is difficult. In this research, elimination criteria were lanthanides, actinides, and mixed metals. If a metal adhered well to the ThO₂, but it provided a poor Ohmic contact, then mixed metals would be considered in future experiments. Table 2 lists a few considered metals and their material properties.

Table 2. List of seven metal candidates and pertinent metal properties. Asterisks denote the metals used in this research.

Metal	Lattice Constant (Lattice: Å)	(100) Lattice Match (ratio: % error)	Nearest Neighbor (Å)	Work Function (eV) [30]	Melting Point (K) [30]
Indium*	Tetragonal 3.2523/4.9461[8]		3.25	4.09	430
Silver	FCC 4.0862[30]	4/3 2.6	2.88	4.74	1235
Aluminum	FCC 4.0495[30]	7/5 1.4	2.86	4.26	933
Titanium*	HCP 2.953/4.729[30]		2.95	4.33	1941
Nickel*	FCC 3.5238[30]	8/5 0.9	2.49	5.35	1728
Gold*	FCC 4.0786[30]	7/5 2.1	2.88	5.31	1337
Platinum	FCC 3.9231[30]	7/5 1.7	2.77	5.93	2041

The four selected metals are chosen for specific advantages over other metals.

Gold was chosen over Pt and Ag due to its ubiquitous use in the electrical industry.

Platinum has the higher work function and melting point. Silver has a poor lattice match and high melting point. Gold is the “universal contact” material in the electronics industry and if ThO_2 is expected to replace SiO_2 , it requires industry standard production methods and materials. However, gold contacts require significant *n*-type doping of Si at the interface to reduce the Schottky barrier formed [11], and hence may not be a suitable candidate for ThO_2 . Indium was chosen over aluminum. Both have poor lattice matching, but indium has a lower work function. Aluminum was already attempted as a contact material for HfO_2 MOS devices [4]. Titanium is often described as another “universal contact” material for its ability to adhere to many materials. Of the metals considered, Nickel has the best lattice match of 0.9% at an 8:5 ratio. Thus, Gold, In, titanium, and nickel were chosen for this research. AppNano SICON series tips were vapor deposited with a nominal 10 nm of metal by the manufacturer (a point important to theory of Chapter 2 and discussion of results later). The AFM tips have a radius of curvature of 10 nm at the tip end. The spring constants ranged between 0.2-0.5 Nm^{-1} .

The AFM adhesion force calibration mode measured the metal-to-crystal adhesion forces. These forces are differentiated into capillary and non-capillary forces as detailed in Chapter 2. The first task was to determine the overall adhesion force for each metal at each humidity condition. A MATLAB program was written to extract force and distance information from the AFM measurements. First, the maximum cantilever deflection was determined by numeric differentiation. Then, the average resting deflection of the cantilever was extracted by averaging the deflection location beyond the

adhesion peak. The maximum deflection is the difference in the resting deflection and the maximum cantilever deflection. By multiplying the deflection range of the cantilever by the spring constant of the cantilever, the adhesion force of the metal to the surface was determined by Equation 14 (Chapter 2).

The 5 samples of the 9 points are averaged together, and the standard deviation is computed for the metals with an asterisk in Table 2. All 9 points are then averaged together (with errors propagated in quadrature) to determine a per-metal atmospheric condition average. By analyzing a plot of the atmospheric conditions versus adhesion force, it was possible to determine the response of each metal to the crystal with differing amounts of water on the surface (Figure 20). A negative slope means that the capillary force of water to metal and water to ThO_2 is a significant contributor to the adhesion force. The larger this slope magnitude, the greater influence water has on the total adhesion force. A zero or positive slope implies that water has an insignificant influence on adhesion force of the metal-to-crystal surface.

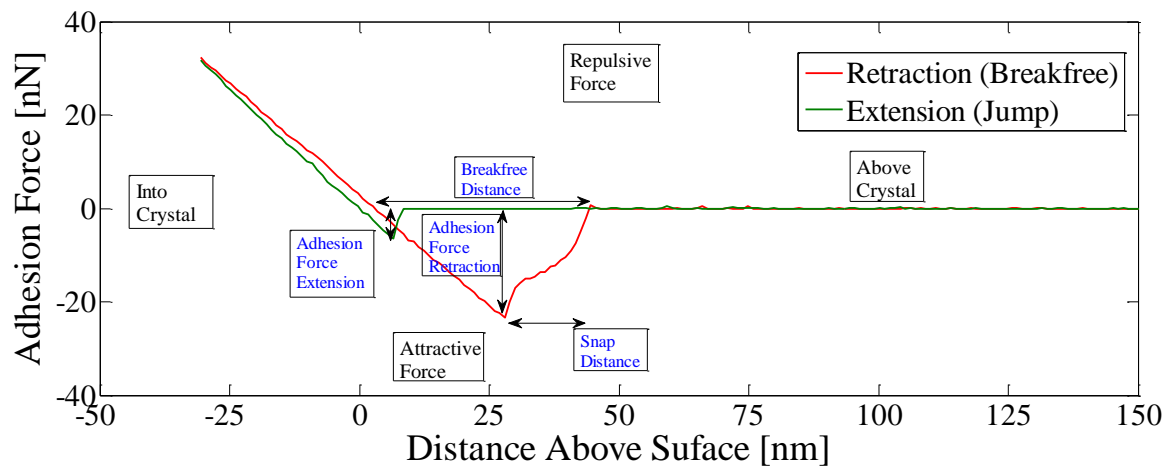


Figure 12. Although for indium, this plot is typical of the adhesion force spectral measurements used for the comparison of metal tips onto the ThO_2 single crystal.

The adhesion plot spectrum provides visual and quantitative insight into the nature of the adhesion force. In Figure 12, the break-free distance [15] is the distance from the crystal surface to the point where the adhesion force is zero and is determined from the point where the adhesion force and repulsion forces are equal, to the point where the tip is out of the surface and at the free floating point. The snap distance is the difference in the cantilever location above the crystal surface from the point of maximum deflection to the free floating point. The slope of the compression line is the slope of the line where the tip is compressing the surface of the crystal. Finally, the adhesion force of the extension motion of the tip, the “jump,” is determined using the same methodology as the adhesion force, except during the extension phase of the cantilever movement cycle. As the tip extends towards the surface, the jump force attracts the tip and bends the cantilever. The cantilever continues to move towards the surface until it is no longer bent, at which point the force of adhesion is equal to the force of repulsion according to Equation 1 (Chapter 2). This point is the zero point distance above the crystal surface.

3.3 Dehydration of the Crystal Surface

As discussed in Section 2.3, the capillary force can significantly increase the total adhesion force. Consequently, the forces associated with water should be reduced in order to obtain an accurate measure of metal-to-crystal adhesion. If metal contacts are to be applied, the crystal will most likely be under vacuum, a low humidity condition. To adjust the number of monolayers or bilayers of water adsorbed on the surface to match the vacuum conditions, dry nitrogen flowed over the surface before and during certain AFM measurements to simulate a dry environment.

A study of water's influence on adhesion is conducted for an indium metal tip on as-grown ThO₂. For this measurement, the relative humidity was measured by a Precon temperature and humidity sensor using an Arduino microcontroller. For simplification, it is assumed that the relative humidity at the sensor is the same as the relative humidity above the crystal surface. Dry nitrogen flowed through the bag at similar rates to the procedure described in Section 3.2. A series of 5 surface adhesion measurements at the same location were taken every 1.5 minutes until the relative humidity dropped below the limit of detection for the device, about 0.25% humidity. The same settings were used for this measurement as the other adhesion force measurements.

3.4 Cleaning the Crystal Surface by Sputter Etch

Removing surface impurities, adsorbed material, and structural defects was critical to obtaining a precise measure of the adhesion force of metals onto the surface of ThO₂. Initial Ar⁺ sputtering experiments on Si wafers validated Yamamura's empirical equations and calibrated the location and width of the sputtering beam (Appendix B).

During initial processing and after AFM measurements, the crystal was chemically washed to remove contaminants. According to literature the appropriate methodology for cleaning and smoothing the ThO₂ surface was an acetone and methanol rinse, followed by a 0.05 μm diamond paste scrubbing [31]. However, the last step in this methodology was currently not allowed for these crystals by federal law and at AFIT. The crystal was affixed to the AFM magnetic base with double sided tape. However, the tape has a sufficient vapor pressure to increase the pressure in the XPS vacuum chamber

and thus was removed before these experiments. Again ethanol and acetone were used as cleaning agents along with gentle scrubbing with laboratory wipes.

In the load lock chamber, which was also the sputter etching chamber, the vacuum was pumped below 10^{-7} Torr. The Ar^+ sputtering gun was a SPECS IQE 12/38 ion source controlled by a SPECS PU IQE 12/38 Power Unit. The ion source was capable of producing a range of energies from 100 eV to 5000 eV with filament currents up to 5.1 Amps. The sputtering filament was degassed three times. Then the Ar(g) supply was tuned to 10^{-4} Torr at the filament. Once the vacuum and Ar(g) pressure were stabilized, the filament was turned on. The beam rastered a 7 x 7 mm region, creating a uniform sputter and ensuring complete crystal surface coverage. To smooth the surfaces, the angle of incidence was at a 75° angle to the Ar^+ beam. At this angle, the ion beam efficiently removed plateaus and edges from the surface [32].

Table 3. Argon sputtering gun was set to the tabulated values for different energies. The value of the extraction, focus 1, and focus 2 voltages are listed as a percentage of the filament voltage.

Energy [eV]	Extraction Voltage [%]	Focus 1 [%]	Focus 2 [%]	Width x [mm]	Width y [mm]
500	70.14	86.78	78.00	7	7
1000	77.54	88.38	77.50	7	7
1500	78.86	88.72	77.44	7	7
2000	79.74	89.02	77.16	7	7

The sputtering gun settings for each experiment are provided in Table 3. The filament emission current of $10 \mu\text{A}$ was sufficient to generate an effective beam current. The experimentation varied the sputtering angle of incidence and ion energy, but the duration and region sputtered was held constant at 30 minutes with an area of 49 mm^2 .

Since the crystal is less than 9 mm², the Ar⁺ sputtered the ThO₂ only 20% of the elapsed time. The remaining time, the beam was sputtering the Ta foil holder. The angle of incidence was based on the rotation of the manipulator holding the crystal. The estimated sputtering yield was based on Yamamura (Equation 15) discussed in Section 2.4. The volume sputtered is derived from Equation 24, and the sputtering depth is listed in Table 4.

Table 4. Mean sputtering depth computations based on Ar ion sputtering energy. The beam current is measured by the SPECS PU IQE 12/38 Power unit. The yield is based on the empirical formula of Yamamura, Equation 15. The theoretical volume is derived from Equation 24. Based on a crystal surface area of 9 mm² the mean depth is calculated.

Energy [eV]	Beam Current [$\mu\text{A/s}$]	Angle of Incidence [°]	Yield [atoms/ion]	Estimated Volume Sputtered [$\times 10^{-6} \text{ mm}^3$]	Estimated Mean Depth Sputtered [nm]
500	9 ± 1	0	0.010 ± 0.003	13 ± 3	1.5 ± 0.3
1000	8 ± 1	75	0.056 ± 0.011	40 ± 9	4.4 ± 1.0
1500	8 ± 1	75	0.15 ± 0.03	110 ± 25	11 ± 3
2000	8 ± 1	75	0.25 ± 0.05	178 ± 42	20 ± 5
2000	9 ± 1	60	0.67 ± 0.13	540 ± 120	59 ± 14

3.5 Cleaning the Surface by Heating

Heating provides two improvements to the surface quality of the ThO₂: it provides vibrational energy to overcome the adhesion energy of surface contaminants and provides free energy to overcome the energy barrier in the movement of ThO₂ molecules to other locations on the surface. The former reduces surface impurities and the latter anneals the surface. Water, hydroxide, and organic material reside on the crystal [7].

The first layer is actually a hydroxide layer and heating ThO₂ to 1273 K drives off all water [7]. Carbon dioxide also resides on the surface but can be driven off with temperatures of 1173 K. The carbon dioxide layer is computed to be only 0.5 layers thick [7]. Potentially, other material is thermodynamically stable on the surface of ThO₂ and requires additional heating to remove. However, the current system is unable to attain these temperatures with a maximum of 673 K.

The ThO₂ crystal was heated twice first to 573 K and then to 673 K. The crystal was heated and cooled slowly to ensure the off-gassing products did not reattach to the surface and allow the crystal temperature to stabilize for the XPS measurements. The vacuum chamber pressure did not exceed 10⁻⁷ Torr. The heating and cooling occurred in 50 or 100 K increments, and XPS spectra were measured after each increase or decrease. XPS was used to determine the relative concentration of contamination driven off the crystal surface.

3.6 X-ray Photoelectron Spectroscopy of As-Grown and Cleaned Surfaces

XPS is used to measure the relative quantity of impurities and adsorbents on single crystal ThO₂. The X-rays were generated from a SPECS XR 50/XRC 50 HQ X-ray source controlled by a SPECS XRC-1000 X-ray Control Source. A filament under high voltage ejects electrons that are accelerated toward an Al or Mg target. The accelerated electron ejects bound electrons from the target material resulting in electronic excited states. These excited states relax and produce characteristic X-rays. The X-ray source's total power was 300 W with 14 kV potential and 21.5 mA on the anode. The Al K_α peak at 1486 eV was assumed to be the main X-ray peak. To produce high signal-to-

noise XPS spectra, a single source X-ray line with a small FWHM is desired. Thus Al, which can only de-excite from the $2p$ to $1s$, is widely used as an excitation source. However, since Al has electrons in the $2p_{1/2}$ and $2p_{3/2}$ there is a small energy splitting due to bonding states and thus the spectra peaks $K_{\alpha 1}$ and $K_{\alpha 2}$ are separated by about 0.8 eV. An additional X-ray K_{α} emission occurs about 10 eV lower in energy due to a double ionized excitation state. This system does not have a monochromator to eliminate these other K_{α} peaks.

The energy resolution of the peaks, ΔE , should be a linear combination of the excitation X-ray peak width, ΔE_p , line width of the photoelectron emission, ΔE_n , and energy resolution of the analyzer, ΔE_a [28]

$$\Delta E = \sqrt{(\Delta E_p)^2 + (\Delta E_n)^2 + (\Delta E_a)^2}. \quad (32)$$

The energy resolution RES is calculated from the *FWHM* of the peak and intensity of the peak, h , by

$$RES = \frac{FWHM}{h}. \quad (33)$$

A hemispherical energy analyzer measures the kinetic energy of the photoelectron emitted from the crystal. The VG Scienta made R3000 was operated by software SES 1.3.1-r9. The analyzer operated with a pass energy of 100 eV, transmission lens mode, a 200 meV step size, and 70 frames per second. To increase resolution, the regional scans during the heating experiments had a step size of 100 meV. The analyzer aperture was set to the smallest curved opening. The analyzer was calibrated with an Gold foil and the system had a work function, ϕ_{sys} , of 4.3 eV. The vacuum chamber was maintained at less

than 5×10^{-8} Torr before and after spectrum measurements; during the measurements, the ion gauges were turned off to reduce noise. The completed system is shown in Figure 13.

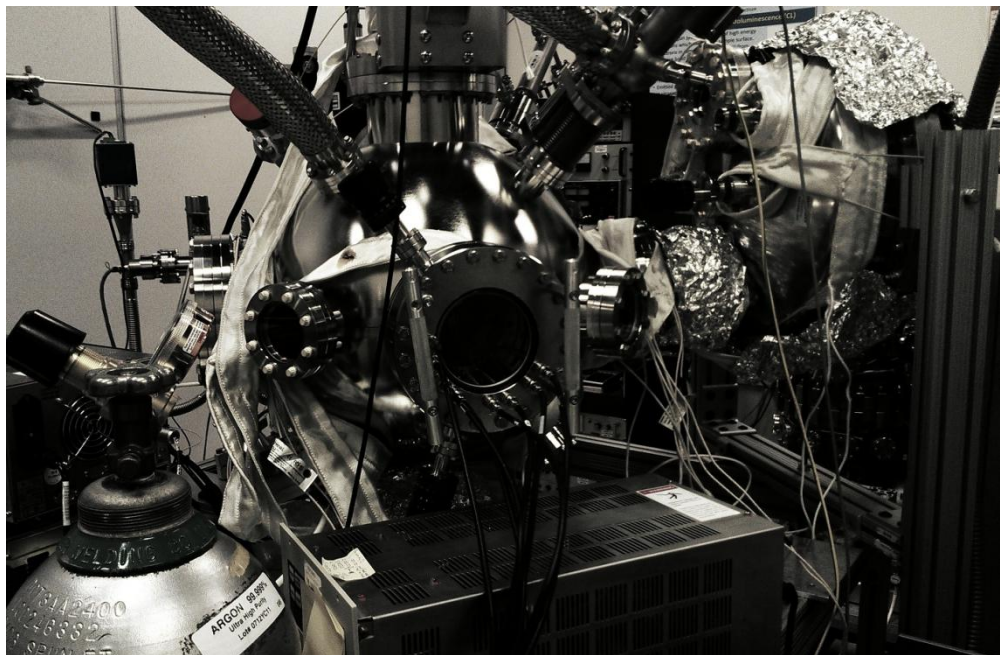


Figure 13. Photograph of the XPS system that was used for this experiment. The electron analyzer is covered with heating tape and tin foil from baking the system. The X-ray gun is located in the upper portion of the picture.

The crystal is mounted onto a Ta foil plate for support during sputter etching and XPS analysis. Ta is chosen as a mounting material for three reasons: none of the Ta emission peaks overlap Th or other peaks of interest, Ta is easier to spot weld than many other metals, and Ta is rigid at the thickness needed for a backing plate. A rectangular, L-shaped Ta piece was mounted to the Ta backing to support the short height of the crystal so that the front side would not be sputter etched by the Ar^+ . The other three crystal sides were secured by triangular, L-shaped Ta foil partially bent over the top. The

Ta foil is naturally oxidized and has impurities which appear in the XPS spectrum.

Figure 14 depicts the crystal mounted to the Ta foil plate. The Ta foil backing plate and small holding arms potentially could reduce the charging on the sample without resorting to a flood gun or metal screen [27, 28].



Figure 14. ThO₂ single crystal #8a mounted to Ta foil plate. The crystal was mounted on three sides by triangular Ta pieces. The white rings insulate a thermocouple used to measure temperature of the sample. The circular device behind the sample holder is the argon sputtering gun.

The raw data plots do not account for the system's work function (4.3 eV). The Ta binding energies shift by the system work function. The Th binding energies shift by both the system work function *and* the amount of surface charging. Attempting to calibrate against the Au 4f or C 1s, does not fully correct the ThO₂ spectra. Thus, all energies in XPS spectra are the “as measured” kinetic energies subtracted from the excitation energy according to Equation 31.

Besides visually inspecting binding energy shifts, data were analyzed for relative height, total intensity, FWHM, and energy shift. Because it is the largest and most resolved peak, the Th $4f_{7/2}$ peak, at 334.9 eV [29] was used as the primary peak for comparison to other peaks. All processing of the peaks' geometry was completed with Igor 6.2.2.2 (survey scans) or PeakFit 4.0 (regional scans) as in Figure 15.

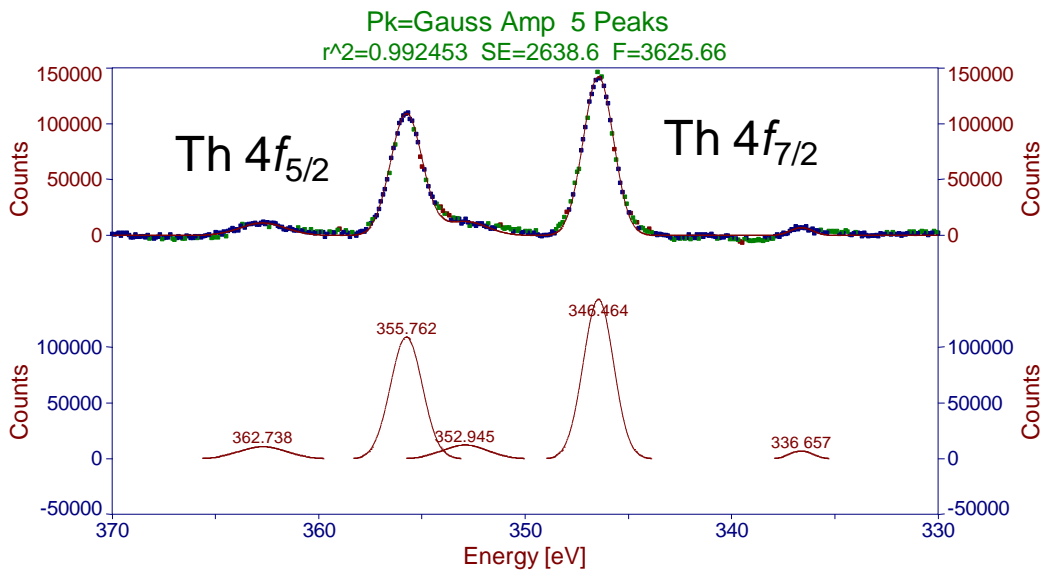


Figure 15. The PeakFit routine fits the Th $4f$ peaks post sputtering. The dots in the upper plot are actual counts and the red line is the sum of peaks in the lower plot. The energy values in the lower plot mark the Gaussian centroid.

The secondary electron background was subtracted using a linear slope. Savitsky-Golay and Fast Fourier Transform filters were used to smooth the spectra. All peaks are considered Gaussian. The peak shape (height and FWHM) was determined by fitting a Gaussian to the peak and then finding the components based on

$$y = he^{-\frac{1}{2}(\frac{x-x_0}{w})^2} + y_0, \quad (34)$$

where y is the number of counts, h is the height of the peak, w is width of the peak or the standard deviation of the peak, x_0 is the binding energy, and y_0 is the baseline height. The PeakFit software automatically computed the area under the peaks, while Mathematica's definite integral process was used to determine the area based on the height, h and FWHM provided by Igor software. The width of the peak, w , is determined by

$$FWHM = 2w\sqrt{\ln(4)}.$$

IV. Results and Analysis

4.1 Results and Analysis of the As-Grown ThO₂ Crystal

The as-grown ThO₂ crystals have significant surface defect and impurity concentrations. The hydrothermal growth technique uses a mineralizer, CsF, to partially dissolve ThO₂ and redeposit it onto the seed crystal. This mineralizer was incorporated into the crystal based on PES measurements. Also, atmospheric contaminants of H₂O, OH, and carbohydrates adhere to the surface. As the crystal cools and the autoclave depressurizes, the crystal growth process changes, resulting in the growth of plateaus, plane edges, and other two or three dimensional formations. Finally, Ta foil was used as a backing and mounting metal, which provides additional XPS signatures.

4.1.1 XPS Ta Foil Peaks and Baseline Th Peaks

Although Ta foil electron binding energy peaks do not overlap with Th emission peaks, the Ta signatures could be obscured by crystal impurities. Comparing the XPS spectrum of the Ta foil backing to the XPS spectrum of the as-grown crystal provided insight into peaks associated with the crystal, as in Figure 16. The Ta 4d doublet peaks at about 235 eV and 245 eV are noticeably resolved.

The Ta 4p_{3/2} at 408 eV, however, is not well-defined but can be resolved using peak fitting methods. Since Ta metal oxidizes readily to Ta₂O₅ there is an O peak at 535 eV associated with Ta₂O₅ and the Ta O peak has a shoulder associated with water adsorbed on the Ta surface. Ta also bonds with atmospheric C, which has an emission peak located at 290 eV. In this research, the O and C peaks associated with Th are

shifted about 7 eV higher in binding energy than the O and C peaks associated with Ta. The experiments at elevated temperatures revealed that the shift is mainly due to charging of the ThO₂. Otherwise, the two C peaks would nearly overlap, and the two O peaks would be separated by about 1 eV. The 1 eV separations are due to the chemical bonding of the O-to-Ta and O-to-Th. The difference in charging for the Ta and ThO₂ eliminate a complete spectrum shift for the work function of the system as per Equation 31. Section 4.2.3 further describes the affect of charging on the crystal and the XPS spectrum.

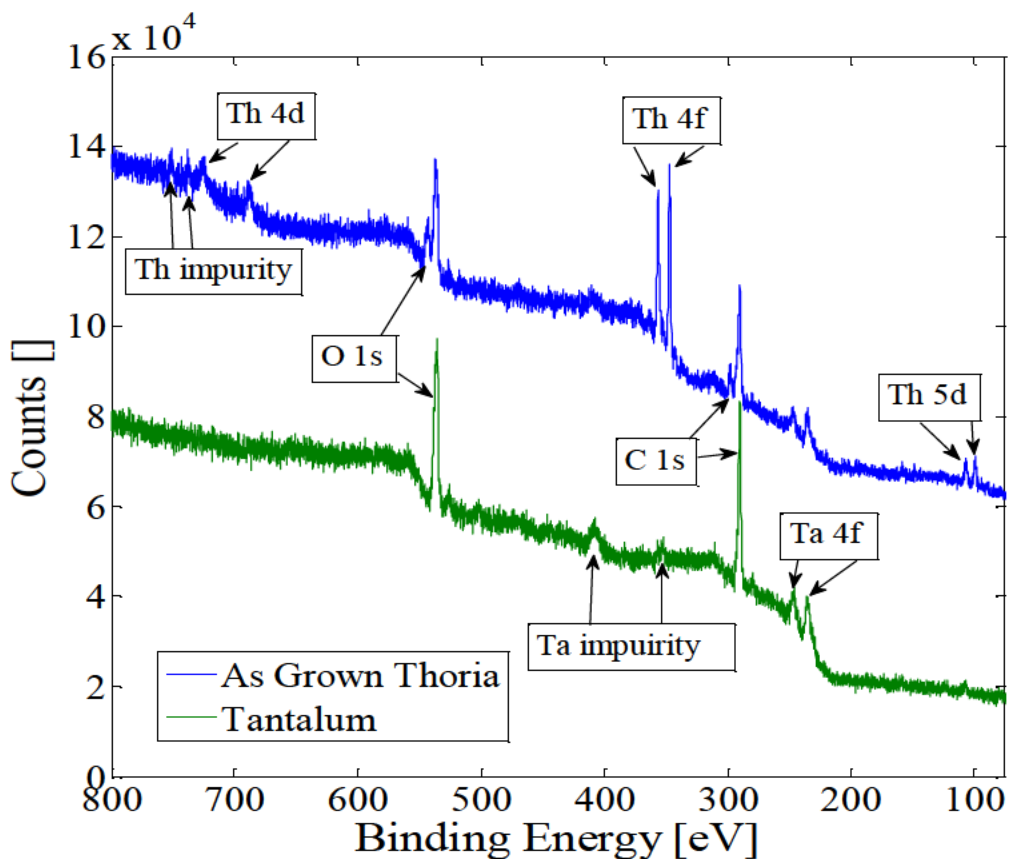


Figure 16. Ta and as-grown spectrum are plotted without shifting due to the system work function. Ta peaks at 250 eV are in both the Ta spectrum and in the Baseline Spectrum. The lower energy C peak near 285 eV, the lower energy O peak at 530 eV, and the peak at 400 eV are associated with Ta.

Other impurities in Ta include peaks near 350 and 400 eV. The peak at 350 eV is between the two Th $4f$ peaks and could distort the peak shape or give false indication of a shoulder. Thus, special care in crystal alignment normal to the electron analyzer reduced the Ta peaks to be indistinguishable from the spectral noise.

Three sets of Th peaks are resolved in the baseline spectrum. The $5d$ peaks near 100 eV are well-resolved because of low binding energy. These electrons must have high kinetic energy, E_{KE} . The high E_{KE} means that the electrons escape the crystal with minimal down scattering and that charging has less influence. Both affects improve the resolution of the low binding energy peaks. The $4d$ peaks near 700 eV are less well-defined because the kinetic energy of the electrons is less and thus are downscattered more easily, as shown in Figure 16. Since these peaks are nearly the same energy as several impurity peaks they will be used to compare the impurities. The Th $4f_{7/2}$ peak at 347 eV is the main Th peak (both in height and area) and is used as a comparison tool for other peaks. The significant $4f_{7/2}$ peak intensity results in a satellite peak at 342 eV due to Al-K α 3, 4 emissions [24]. The shake-up peak of the Th $4f_{7/2}$ results in a shoulder on the lower binding energy side of the Th $4f_{5/2}$ peak, and the shake-up peak of the Th $4f_{5/2}$ lies 7 eV higher in binding energy. The locations of the shake-up peaks give an estimate for the band gap of 7 eV.

4.1.2 Hydrothermal Growth Mineralizer Impurities in the As-Grown ThO₂ Crystal

CsF is within the near surface region of the sample. The Cs $3d$ peaks appear at 737 and 751 eV, (NIST value of 724.5 and 739.4 [33]) and the F 1s peak appears at 697 eV (NIST value of 685.9 [33]). These values are shifted due to sample charging and the

system work function as in Section 4.2.3. The Cs and F peaks do not appear in the Ta foil spectrum (Figure 16). The peaks near 700 eV are associated with the ThO₂ crystal.

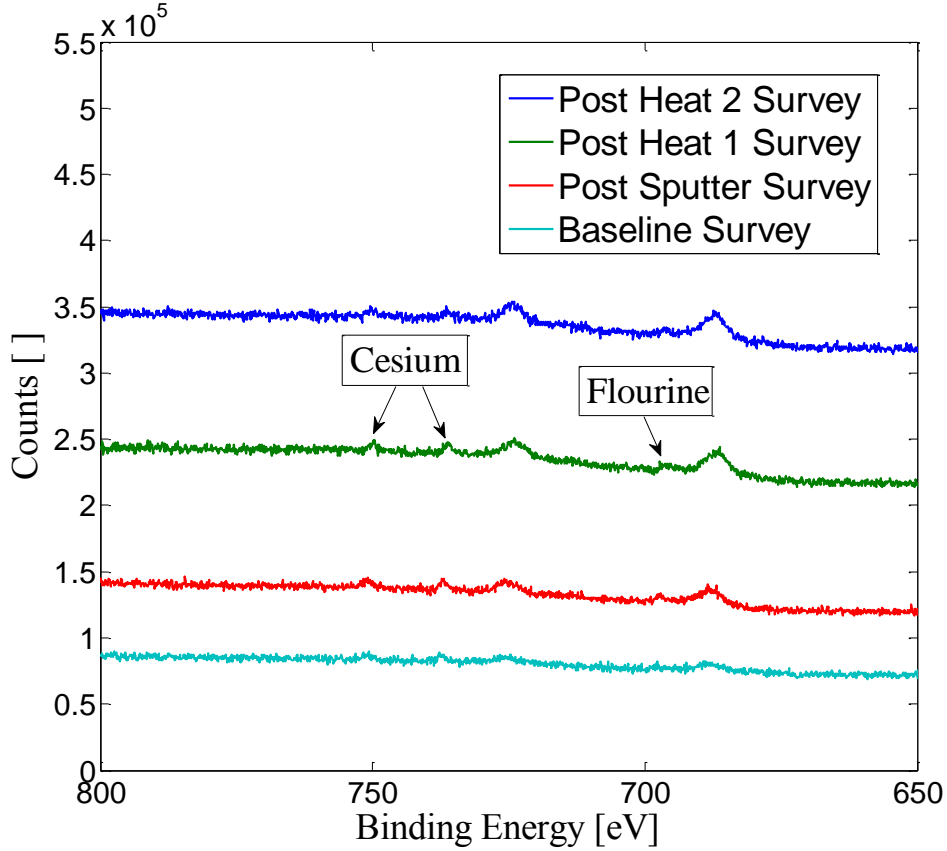


Figure 17. F and Cs impurity plot. The light blue spectrum is the as-grown crystal, the red line is after sputtering, the green line is after the first heating sequence, and the dark blue line is after the second heating sequence. The two unlabeled peaks are the Th 4d peaks.

4.1.3 Atmospheric Adsorbents on the As-Grown ThO₂ Crystal

O and C containing molecules are known to be adsorbents on the surface of ThO₂, and O is located within the bulk as the oxide of ThO₂. The C oxidation state causes a chemical shift in the binding energy of electrons resulting in a change in their measured

kinetic energies. The small shoulder on the higher binding energy O 1s ThO₂ peak (544 eV) is attributed to OH adsorbed onto the surface (Figure 18). Some of the contaminants are bound strongly enough to not vaporize at 10⁻⁹ Torr since they appear in the XPS spectrum at those pressures.

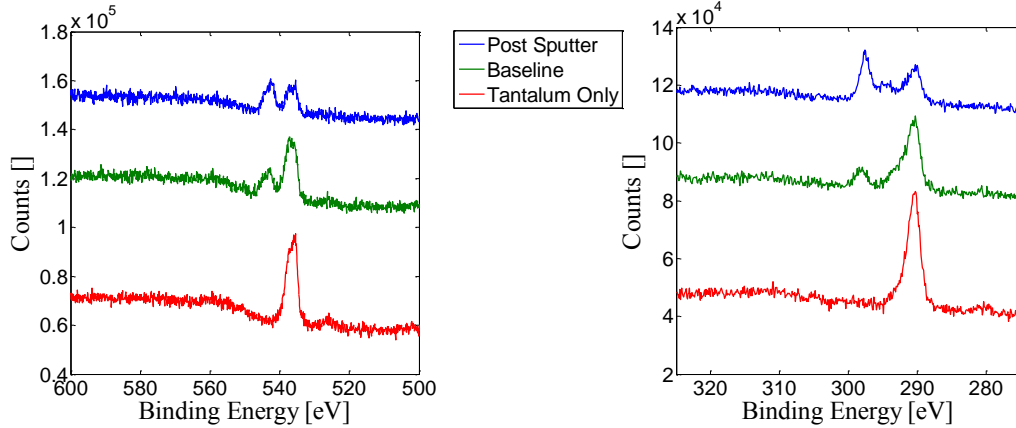


Figure 18. O and C peaks for the as-grown ThO₂ crystal. The peaks on the right in each spectrum are associated with Ta. The peaks on the left of each spectrum are associated with the crystal.

Although exotic final state effects are possible with *s*-character electrons as in Li₂O [34], the C 1s and O 1s peaks in this research are not spin-orbital doublets nor are the doublets due to multi-electron final state effects. The C 1s peak and O 1s peak associated with Ta are lower in binding energy than the C 1s and O 1s peak associated with ThO₂. The decrease in the Ta associated C 1s and O1s from the red, green, and blue spectra is due to refined placement of the ThO₂ crystal in front of the electron analyzer. The magnitude of decrease in Ta bound C intensity is proportional to the magnitude of decrease in Ta bound O.

4.1.4 Roughness of the As-Grown ThO₂ Crystal as Measured by AFM

The surface roughness is best measured with atomic force microscopy (AFM). Both types of data acquired by the AFM, tapping mode surface scan and adhesion force calibration, provide insight into the surface characteristics. Figure 1 presents the as-grown ThO₂ crystal through an optical microscope as multiple faceted, shiny clear and white giving the perception of a flat, smooth surface; however, the crystal is not smooth at the atomic level. The total surface deviation is nearly 100 nm as in Figure 19. Surface contaminants, impurities, and water could also motivate this surface roughness.

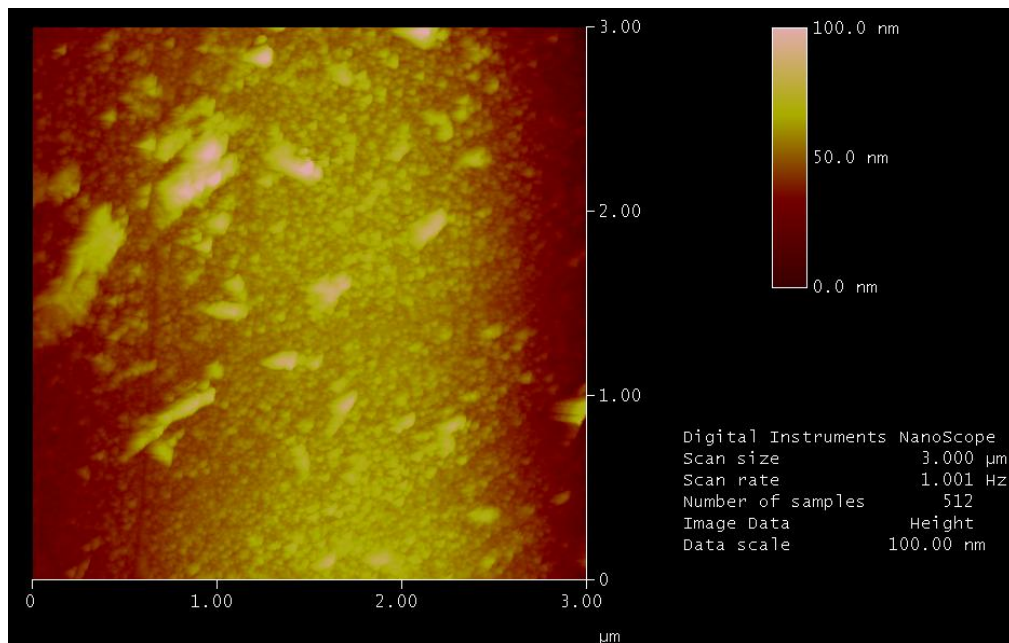


Figure 19. 3 x 3 μm initial surface feature scan by AFM. The surface is severely pitted with large features. These features are either contaminants or crystal, but will decrease the surface adhesion due to reduction in the tip surface area contacted.

Figure 20 depicts the adhesion forces of each of metal to the as-grown ThO₂. Force measurements at different locations on the crystal surface varied substantially, as in Figure 20 a). The measured error is due to surface feature variability and effective

contact area of the tip. Adhesion force measurements at a single location vary by smaller amounts, as in Figure 20 b). This error is due to electronic, detector, and vibration noise, which is in all electronic instrumentation.

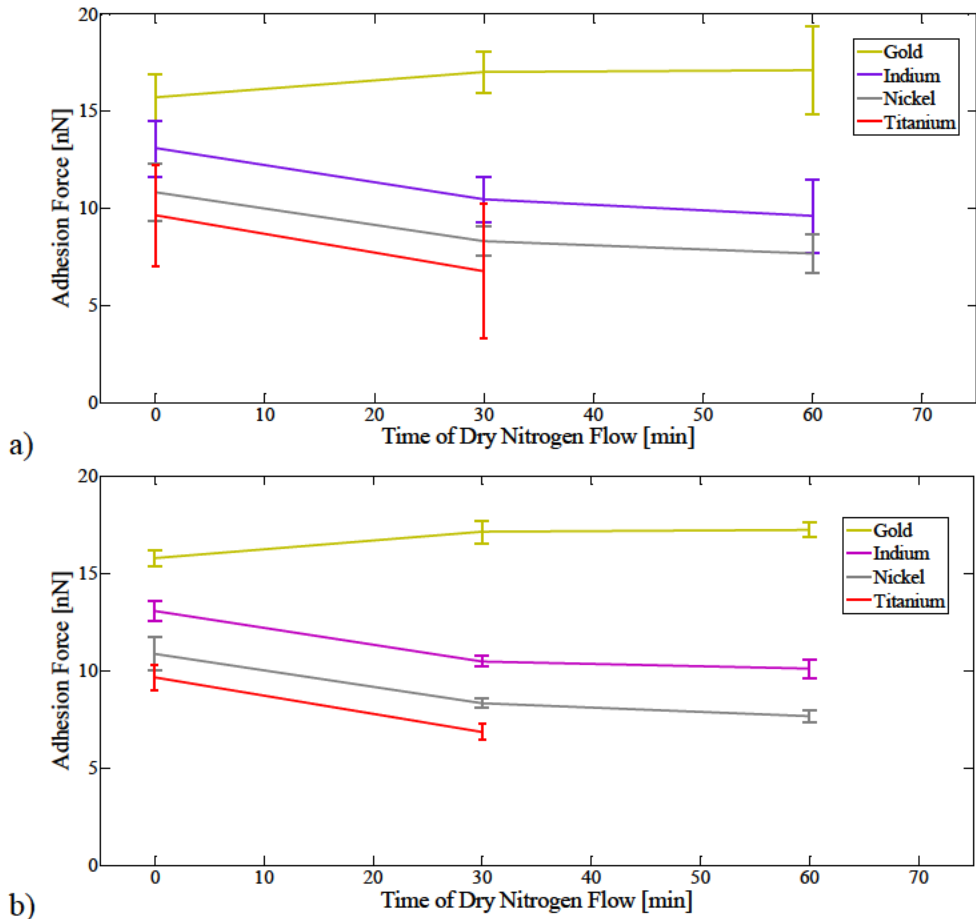


Figure 20. Crystal surface feature error verses electronic error. a) The surface error is computed by conducting standard error of the 9 measurement locations. Decreasing the humidity tends to increase the deviation. Plot a) depicts 1σ standard deviation with error propagated in quadrature. b) depicts 3σ standard deviation of the electronic error from the 5 measurements at the same location.

4.1.5 AFM Adhesion Force Measurements of the As-Grown ThO₂ Crystal

AFM also generates adhesion data from the adhesion force calibration. Analysis of the data in Figure 21 indicates a larger adhesion force for the metals to C (graphite) than for the metals to ThO₂.

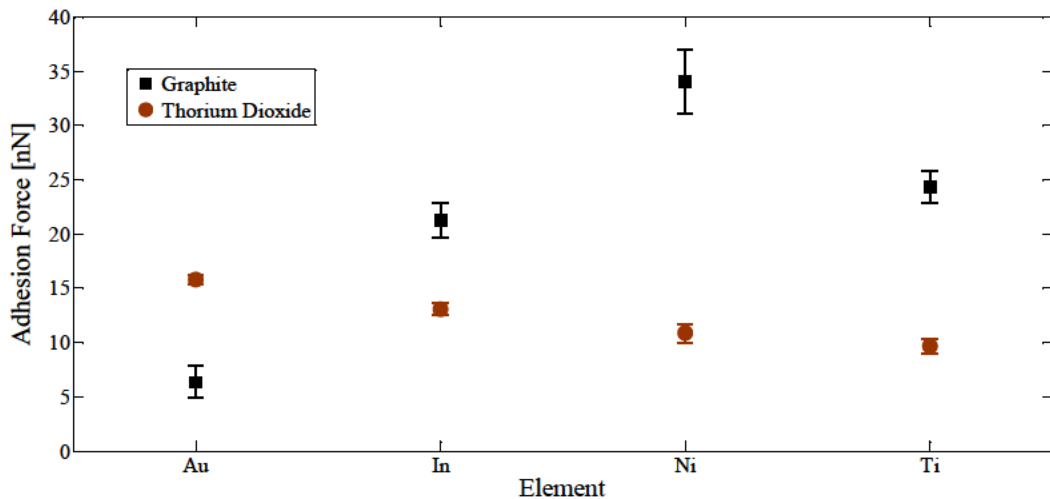


Figure 21. As-grown thorium dioxide adhesion force and graphite adhesion force. The graphite adhesion force is nearly 3 times larger for most metal tips to the graphite than to the thorium dioxide.

It is believed that the increase in adhesion force for graphite is likely due to the increase in contact surface area since graphite is atomically flat, which increases the effective AFM radius of the tip, $R_{t,eff}$, as supported by Equations 2, 6, 9, and 12. However if the flat plane is actually rough, the effective radius of the surface is reduced as in Section 2.2. Cleaning the crystal surface should reduce the surface variability, decrease the adhesion force deviations, and increase the total adhesion force.

The indium and gold metal tips are candidates for demonstrating the influence of water on the adhesion force of metals to ThO₂. Metallic indium is hydrophilic and easily

oxidized. The oxidation layer attracts water through hydrogen bonding and capillary forces. Gold is hydrophobic and does not oxidize readily. It should not have a significant amount of water on its surface. Therefore, capillary forces should be present in indium metal adhesion measurements and not be present in gold measurements.

Plotted in Figure 22 is the adhesion spectrum for In and gold demonstrating the extension (jump) and retraction (break-free). An interesting phenomenon occurs in the “snap” region of the break-free of indium. The indium tip in normal atmosphere exhibits two regions of different slope; one near 25 nm where the slope is large, another at 30 nm where the slope is lower and curved. This reveals the affect of two forces: the longer range capillary force and the shorter range van der Waals and dipole-induced dipole force. The gold metal tip spectrum does not have the longer ranged force as its “snap” region is 2 ± 1 nm while In snap region is 13 ± 2 nm.

Since the gold spectrum does not have the characteristics of capillary adhesion force, the “jump” force should be small; although, it should be the first force encountered as the tip approaches the surface, and the water from ThO₂ wets the surface of the metal. The “jump” force associated with In is certainly attributable to the capillary force. Surprisingly, however, the “jump” force exists in the gold extension spectrum, even if it is significantly smaller than the indium jump force. The gold adhesion force during retraction is six times larger than the extension “jump” force, but for indium the adhesion force during retraction is only 2.5 times larger than the extension force.

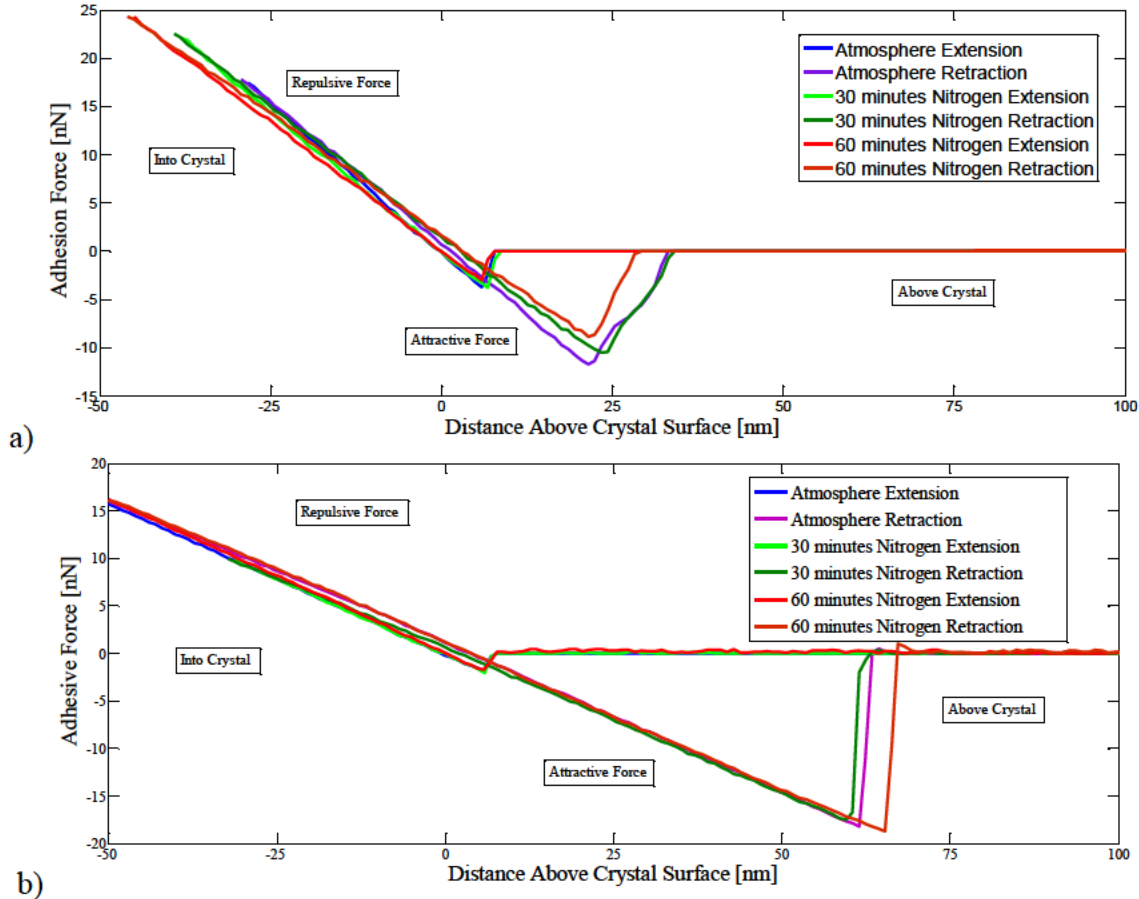


Figure 22. Adhesion plot of indium and gold on as growth ThO_2 . Plot a) shows the extension and retraction spectrum for indium at atmospheric conditions and after 30 minutes and 60 minutes of dry nitrogen flow. Plot b) shows the extension and retraction spectrum for gold at atmospheric conditions and after 30 minutes and 60 minutes of dry nitrogen flow. These spectra were altered so that the adhesion forces were zeroed and the repulsive force slopes align.

The indium spectrum at atmosphere exhibits a large adhesion force curve associated with capillary force. And under dry nitrogen, the curve diminishes, but the adhesion force remains concluding that the van der Waals and dipole induced-dipole are still present. The gold adhesion spectrum does not demonstrate the capillary force, and yet its adhesion force is larger than indium's adhesion force. In fact, the dry nitrogen purge of humidity seems to increase the adhesion force of gold towards ThO_2 .

The crystal surface has large variations that influence total adhesion force adhesion variability by location and magnitude of capillary force. Significant impurities reside on the surface and near bulk. Systematic sputter etching and heating eliminates many of these sources of variability.

4.1.6 Surface and Interface Energy Computations for the As-Grown ThO₂ Crystal

The total adhesion force is computed from the interface energy by the sum of both the non-capillary and the capillary force contributions

$$F_{adh} = 4\pi R_t (\gamma_{tw} + \gamma_{cw} - \gamma_{tc}) + 4\pi R_t \gamma_L \cos \theta. \quad (35)$$

The capillary force term cannot be combined with other adhesion force term. Although both contain the radius of the tip, the assumption that this radius is the same for both the capillary force and all other forces is not correct.

The non-capillary force radius is smaller than the actual radius. Surface roughness increases the distance D between the crystal surface and the metal tip. Figure 23 depicts a rough surface and a curved tip that contacts only parts of the surface. This results in a larger D , causing a larger denominator in Equation 2, and results in a smaller F_{vdW} . Thus one could measure the increase in average distance and conduct an integral in Equation 7. However, continuing the assumption that the tip is perfectly spherical and the crystal surface is completely planer, one can use Equation 8 as equivalent statement. To continue this assumption, $R_{t,non-cap}$ must become the effective radius, $R_{t,non-cap,eff}$. Therefore, as the surface becomes more rough, the average distance, D , between the tip and crystal increases and thus $R_{t,non-cap,eff}$ decreases.

The capillary force radius can be larger or smaller than the tip radius. A hydrophobic tip repels water, and its meniscus angle and effective tip radius should be nearly zero. A hydrophilic tip's effective radius varies with the relative humidity as described by the Kelvin radius, Equation 5. Greater humidity means that more water is on the surface which allows the tip to penetrate deeper into the water, d . As d increases, the denominator approaches 1.0, and the effective capillary radius approaches the actual tip radius. The more hydrophilic the metal tip, the more the water wicks up the tip and the larger d becomes. Figure 23 depicts a hydrophilic tip where the water wicks up the side of the tip.

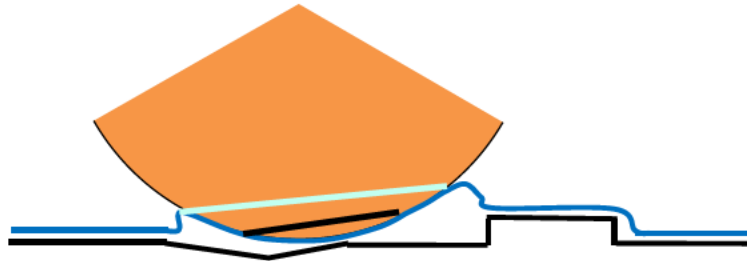


Figure 23. The effective radius of the tip is different for capillary and non-capillary forces. A hydrophilic tip is depicted. Water would not form a meniscus on a hydrophobic tip. The black line on the orange tip indicates the portion of the tip within the effective distance D from the crystal to the tip for non capillary forces. The light blue line is the effective radius due to wicking of the water to the tip.

In order to combine the two terms in Equation 35, a ratio of effective radii is multiplied to the second term.

$$F_{adh} = 4\pi R_{t,eff,non-cap} (\gamma_{tw} + \gamma_{cw} - \gamma_{tc}) + 4\pi R_{t,eff,cap} \frac{R_{t,eff,non-cap}}{R_{t,eff,non-cap}} \gamma_L \cos \theta \quad (36)$$

Dividing the total adhesion force by the common terms results in the total interface energy,

$$\gamma_T = \gamma_{tw} + \gamma_{cw} - \gamma_{tc} + \frac{R_{t,eff,cap}}{R_{t,eff,non-cap}} \gamma_L \cos \theta, \quad (37)$$

where γ_T is the interface energy used to generate the adhesion force of the tip to the crystal surface and is the measured quantity in this research. This equation is not found in literature, and it is a novel method for investigating the adhesion forces of two surfaces, given by a third surface—including both capillary and non-capillary forces.

To compute γ_T , the $R_{t,eff,non-cap}$ is estimated to be 20 nm given the tips were manufactured with a radius of curvature of 10 nm and approximately 10 nm of metal is deposited on each tip. An estimated 25% of the tip provides contact with the crystal surface giving an $R_{t,eff,non-cap}$ of 5 nm. The γ_T in Table 5 is calculated by dividing the adhesion forces plotted in Figure 21 by $4\pi R_{t,eff,non-cap}$.

Table 5. As-grown interface energy estimates for metal tips onto ThO₂. The interface energies are computed with an effective tip radius of 5 nm.

γ_T [Jm-2]	Au	In	Ni	Ti
As-Grown Wet	0.25 ± 0.02	0.21 ± 0.02	0.17 ± 0.03	0.15 ± 0.05
As-Grown Dry	0.28 ± 0.02	0.16 ± 0.03	0.12 ± 0.02	0.11 ± 0.06

The adhesion force of gold increases with increasing humidity. Because the tip is hydrophobic, the last term of Equation 37 should be nearly 0, since the effective capillary radius of the tip is near 0. A decrease in humidity should increase the residual interface energies γ_{tw} and γ_{cw} . The reduction in adsorbed water changes the surface chemistry and increases the residual interface energy according to the Dupre Equation, Equation 11. Since the crystal surface geometry does not change during the dehydration process, γ_{tc}

should not change. Thus, based on Equation 37, the total interface energy of adhesion, γ_T , should increase with decreasing humidity (Table 6), which is supported by the computed values (Table 5).

Table 6. Affect of surface dehydration on interface energy quantities. Dashed lines represent the estimated change while solid lines represent a measured change.

Tip Classification	γ_T	γ_{tw}	γ_{cw}	γ_{tc}	$\cos(\theta)R_{t,eff,cap}$
Hydrophobic (Au)	↑	↑	↑	N/C	~0
Hydrophilic (In, Ni, Ti)	↓	↑	↑	N/C	↓

The adhesion force of indium, nickel, and Titanium could increase or decrease based on decreasing humidity. Like the hydrophobic tips, γ_{tw} and γ_{cw} should increase with decreasing humidity. But the capillary energy term in Equation 37 should decrease since the effective radius of the tip for capillary force, $R_{t,eff,cap}$ decreases with decreasing humidity. Based on Table 6, the magnitude of the capillary force is greater than or equal to the magnitude of the non-capillary forces. Since all the hydrophilic metal tip interface energies decreases, the capillary term decrease is much larger than the interface energy increases.

For the as-grown crystal, each term in Equation 37 provides the insight into the magnitude of the surface energy bonding. The $R_{t,eff,non-cap}$ and γ_{tc} should not change because they are independent of adsorbed water. But, $R_{t,eff,cap}$, θ , γ_{tw} , and γ_{cw} are influenced by the change in surface hydration. The critical quantity γ_{tc} describes the residual interface energy after the metal tip contacts the crystal. An increase in γ_{tc} , means

the metal tip and crystal surface do not satisfy dangling bonds, dipoles, etc, which could be interpreted as poor lattice match. These facts become critical when describing the post cleaning crystal.

4.2 Changes in the ThO₂ Crystal during Sputtering, Heating, and Dehydration

4.2.1 Heating Reduces the Mineralizer Impurities

The F and Cs peak intensities dramatically change during the sputtering and heating process. The broad, barely perceptible impurity peaks of the as-grown crystal actually become sharper and more resolved with sputtering (Figure 17 in Section 4.1.2). In fact the height of the F peak nearly doubles from the initial scan to the post-2000 eV sputter scan, and the F 1s to Th 4f_{7/2} ratio rises from less than 1% to 7%. Considering that the Th peak is also becoming more resolved, this improvement is significant. The sputtering removes the surface atmospheric contaminants increasing peak resolution and exposing more of the F and ThO₂ surface. Additional sputtering removes further impurity and crystal layers, but exposes more F.

Heating the sample then drives off the exposed F. Figure 24 depicts the results of both heating runs. After the 673 K annealing cycle, when the sample is at 300 K, the F 1s to Th 4f_{7/2} peak ratio is less than 1%. Because of the small signal to noise ratio at 700 eV, the error in the F peak area is large, up to 50%. However, the reduction from 7% post sputtering to less than 1% is statistically significant.

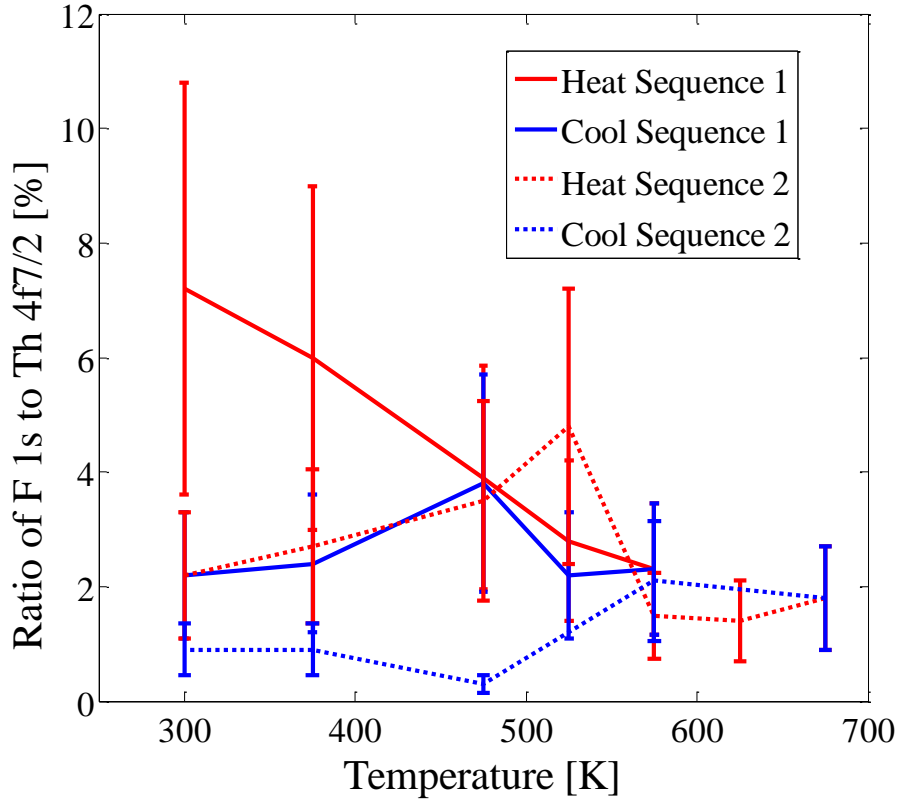


Figure 24. Fluorine to thorium peak ratio. The plot shows the influence of heating on the fluorine peak. Successive heating reduces the ratio to below 1%. Heating of the sample drives off fluorine from the surface. The error bars represent standard error based on the R-squared value of the peaks. The large error is due to the small signal to noise in the region

The Cs impurity peaks also undergo increased resolution with surface sputtering, but it is less significant than the F resolution. The Cs $3d_{5/2}$ peak intensity increases from 9,000 counts initially to 14,000 counts after all sputtering, but the ratio of peak area to the Th $4f_{7/2}$ stays constant at around $8 \pm 3\%$. The Cs, however, is not driven off by annealing. The Cs $3d_{5/2}$ peak to Th $4f_{7/2}$ peak starts at $11 \pm 2\%$ before heating, and is at $10 \pm 2\%$ after the first heating, and drops to $9 \pm 2\%$ after the second heating. Considering

the large error in this region of the spectrum due to small signal to noise, the drop in ratio percentage is within the error and thus statistically inconclusive.

Because all peaks become more resolved with sputtering, it is difficult to determine if and how much mineralizer impurity is removed. The peak resolution increases at a nonlinear rate with sputtering energy, and the electrons escape the surface without down-scattering or other peak broadening events. Thus the improvement in peaks can be attributed to the cleaning of the surface. Since XPS is a surface analysis tool, the depth of the mineralizer inclusion into the bulk is unknown, although previous TOF-SIMS experiments indicate it is deposited within the first 100 nm of the crystal surface [22]. In either case, additional sputtering, perhaps at higher energies, or heating to higher temperatures is required to remove the Cs.

4.2.2 Heating Changes the Concentration of Atmospheric Adsorbents

CO, CO₂, and other organic molecules should adsorb to the surface of ThO₂ [7, 35]. However, the C 1s peak associated with ThO₂ is nearly symmetric. Deconvolution results in two curves that are approximately 2 eV separated with the most intense peak at lower binding energy. The C 1s and O 1s peaks associated with the Th both shift in energy due to charging. The C 1s peak shifts almost 4 eV (Figure 25). During both annealing processes, the larger peak's intensity varied between 18-22% of the Th 4f_{7/2} peak, and the smaller peak varied between 1–3% of the Th 4f_{7/2}. Heating the crystal to 675 K did not remove the adventitious C nor change its oxidation state to a measureable extent with this technique. This is understandable as many researchers heat the sample to 1000 or 1075 K to drive off contaminants from Th or ThO₂ [24, 31]. As

stated in section 2.2, the (111) face should oxygen terminate, which would lead to the conclusion that CO and CO₂ adhere to the crystal surface. If the organic C is liberated by the vacuum, this matches the two carbon peak theory.

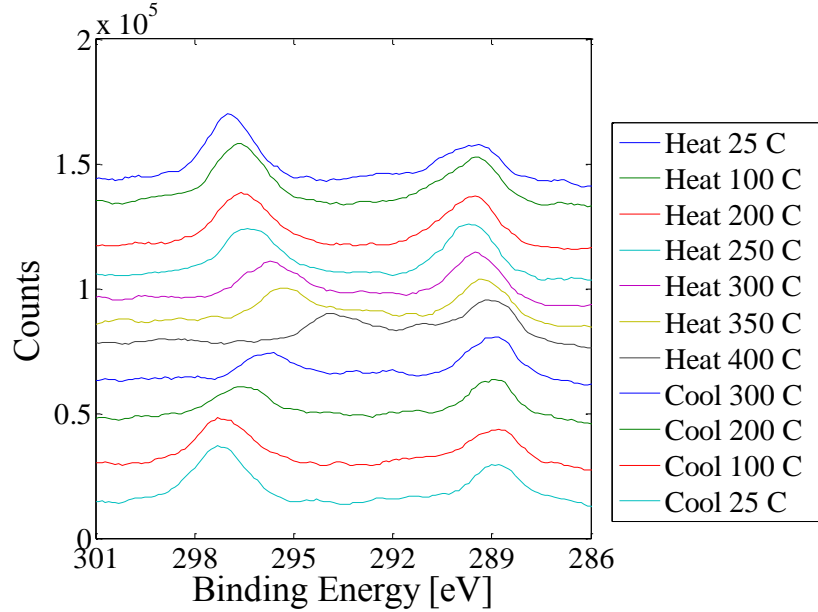


Figure 25. The C 1s peaks during 2nd heating experiment. The C 1s on the Ta peak (right) does not shift with heating. The C 1s on ThO₂ peak (left) shifts towards lower binding energy as the crystal is heated. “Heat” label is during the heating phase of the cycle and “Cool” is during the cooling phase of the cycle. This plot has a 5 point, moving-average smoothing function. The system work function and sample charging is not accounted for in this spectrum (the Ta associated C should be at 285.5 eV [33]).

Even with the 7 eV of charging removed, the C associated with ThO₂ has about 1 eV higher binding energy than the C associated with Ta. This is most likely caused by C present with different oxidation states, and the C is chemically shifted due to the substrate to which they are adsorbed.

The OH peak on the shoulder of the Th O 1s peak decreased slightly with heating. The O 1s peak associated with O bonded to Th in the crystal lattice remained nearly constant at 25% the intensity of the Th $4f_{7/2}$ peak (Table 7). The OH shoulder, at the higher binding energy, decreased by nearly half when heated to 675 K (Table 7). Annealing at higher temperatures should remove the OH shoulder.

Table 7. O 1s ratio peak intensity changes after sputtering and heating. The O 1s peak intensities are compared to the Th $4f_{7/2}$ peak of that spectra.

Area Ratio	O 1s Th-O	O 1s OH Shoulder
Post 673 K heat	$25 \pm 2\%$	$5.7 \pm 1.1\%$
Post 573 K heat	$25 \pm 2\%$	$7.2 \pm 1.8\%$
Post sputtering	$23 \pm 2\%$	$11 \pm 2\%$
Baseline	$26 \pm 4\%$	$11 \pm 3\%$

4.2.3 Heating Changes the Quantity of Charge on the ThO₂ Surface

All ThO₂ peaks have binding energy shifts as the crystal is annealed. This is solely due to the charging of the ThO₂ crystal. The first indication of the charging was the investigation of C 1s peaks, which are plotted in Figure 25. The C peak associated with Ta shifts less than a few tenths of an eV from its original location. The Ta foil is grounded and is not influenced by charging phenomena.

The locations of Th peaks in ThO₂ have not been reported in literature for single crystals. Most values reported are of ThO₂ powder or of Th metal with the surface oxidized to a ThO₂ thin film [24, 29]. Since XPS is a surface technique, these peaks should be at the same binding energy; however, the previously reported values did not

have the peak shifting due to crystal charging. The measured values, once shifted to account for the charging and work function of the system, closely match the values of Fuggle and McLean. However, they do not perfectly align, especially the further they are from the Th $4f_{7/2}$ peak, as indicated in Table 8.

Table 8. Measured thorium binding energy compared to previously reported values. The experimental binding energy values are from the post sputter, post heating spectra. PeakFit 4.0 was used to generate the Gaussian fit to the peaks. The shifted binding energy accounts for the system work function and surface charging.

Orbital	Experimental Binding energy [eV]	Shifted Binding Energy [eV]	Fuggle Binding Energy [eV] [29]	McLean Binding Energy [eV] [24]
$5d_{5/2}$	98.9 ± 0.1	87.4	87.0	
$5d_{3/2}$	106.0 ± 0.1	94.5	94.0	
$4f_{5/2}$ K- α	336.2 ± 0.2	324.7		325.
$4f_{7/2}$	346.42 ± 0.01	334.9	334.9	335.0
$4f_{7/2}$ satellite	353.7 ± 0.2	342.2		343.
$4f_{5/2}$	355.72 ± 0.02	344.2	344.2	344.3
$4f_{5/2}$ satellite	362.9 ± 0.1	351.4		351.7
$4d_{5/2}$	686.98 ± 0.06	675.5	676.2	
$4d_{3/2}$	724.36 ± 0.08	712.8	713.5	

Besides surface charging and the system work function, additional processes cause the spectrum energies to contract. If the Th binding energy values are shifted so that the Th $4f_{7/2}$ peak matches the literature value, the $5d_{5/2}$ binding energy is 0.4 eV

above literature value, whereas the $4d_{5/2}$ binding energy is 0.7 eV below literature value. This demonstrates the contraction of the binding energies. Fuggle reports no charge build up on the surface. This can be attributed to Fuggle's ThO₂ crystal being surface oxidation on Th metal which grounds the thin film layer [29]. The hydrothermally grown crystal is 1.5 mm thick, too massive for mobile charges to reach the conductive Ta mounting plate in this highly resistive material. The Ta foil backing and Ta triangular brackets do not provide discharging. In Figure 26, a linear interpolation is used to align and correct the measured spectra to the results of the thin films [29].

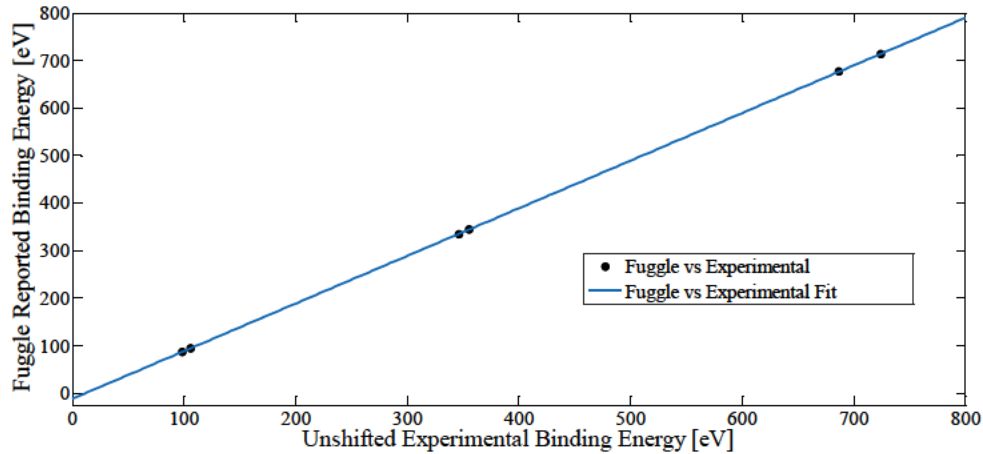


Figure 26. Uncorrected experimental binding energy versus Fugle reported binding energy. The points on the plot are the Th 5d, Th 4f, and Th 4d peaks for the post sputtering and heating spectrum and the binding energies reported by Fuggle [29]. Error bars are depicted, but are not visible. The error is computed as FWHM of peak and varies from 1.2 eV for the Th 4f_{7/2} to 3.0 eV for the Th 4d_{3/2}.

The equation of the fit line is $BE_{Fugle} = 1.0018 * BE_{Experimental} - 12.14$ with $R^2 = 1$.

The y-intercept represents the sum of both the surface charging and system work function. For a resistive material, Equation 31 becomes

$$E_{KE} = h\nu - \phi_{sys} - E_{binding} - Q_{crystal}, \quad (38)$$

where $Q_{crystal}$ is the effective energy shift cause by charging on the crystal described by the regression in Figure 27. The system work function, ϕ_{sys} , calibrated using gold $4f$ peaks is 4.3 eV. Thus at room temperature and under UHV, 7.8 ± 0.1 eV of sample charging exists. However, the slope of the regression is 1.002, which should be 1.00 if the contraction of the spectrum did not exist. This contraction is most likely due to a non-equilibrium surface convolved heavily with the non-linear dependence of the photoelectric mean free path as a function of kinetic energy. This non-linear dependence is well-described by the so-called “Universal Curve” [5].

Using the Th $4f_{7/2}$ peak shift as a representative peak, the change in binding energy due to annealing is plotted in Figure 27. Initially the crystal charging and system work function summed to a shift of 12 eV compared to the previous experiments [29]. During the first heating, the sample discharges rapidly and stabilizes at 10 eV, returning to approximately 11.5 eV upon cooling. When the sample is heated a second time, the charging follows that same path as the first cooling regime, and above 620 K has a sharp decrease in the degree of charging. Subsequent cooling causes the charging to return on a similar path, resulting in hysteresis in the temperature versus surface charging.

From the family of sigmoid functions, the Fermi function is fit to the data based on the system work function of 4.3 eV. This, system work function should not change significantly with temperature and is confirmed with the C $1s$ Ta peaks (Figure 25). The minimum value of the function was set to 4.3 eV. Based on the function, the degree of crystal charging is 7.3 eV, and the function inflection point is 698 K. At 850 K the function approaches the asymptote.

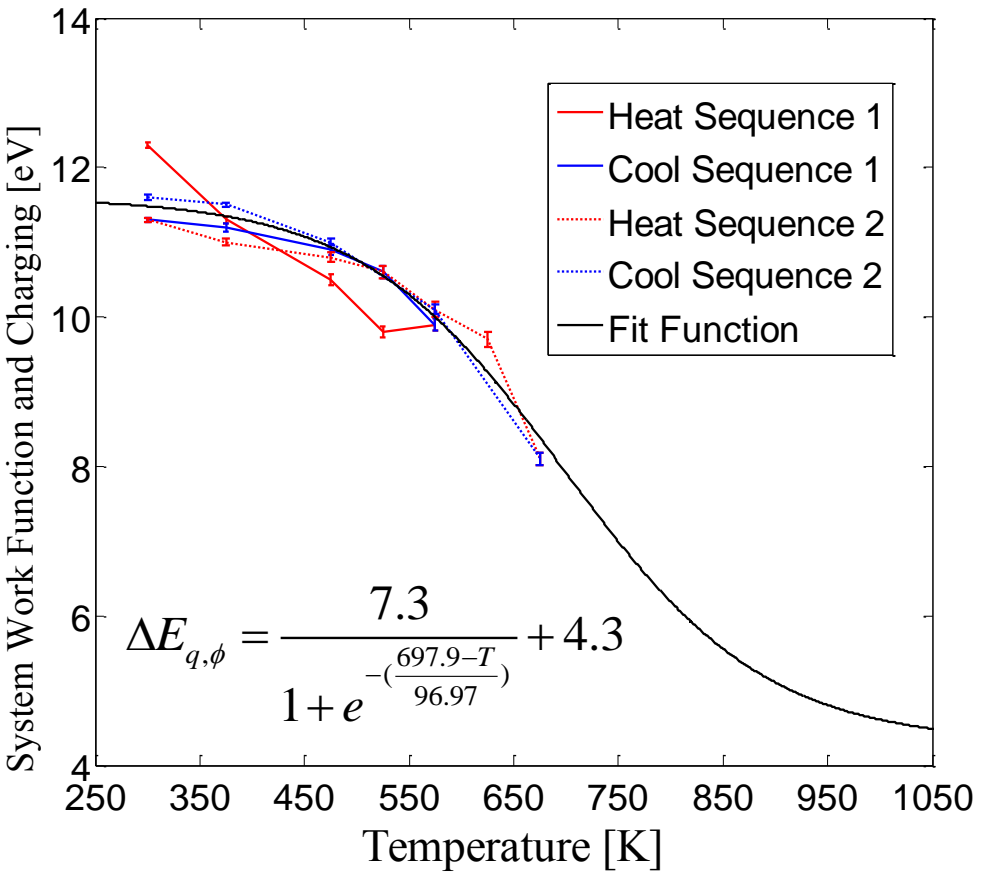


Figure 27. System work function and charging of ThO₂ verses temperature. The Th 4f_{7/2} peak is used to reference the peak shift. The measured peak location is subtracted from the value given by Fuggle [29]. Heating the crystal reduces the charging. The error bars are based on the 95% confidence of peak location determined by the PeakFit 4.0 software.

A secondary peak forms next to the main Th peaks at lower binding energy.

Figure 28 depicts the Th 4f_{7/2} at 342.9 eV and the 4f_{5/2} at 352.3 eV. The Th 4f_{7/2} satellite peak is normally underneath the Th 4f_{5/2} main peak and thus the 4f_{5/2} peak always has a shoulder. But the Th 4f_{7/2} does not have a shoulder as depicted in Figure 15. A single peak on the Th 4f_{5/2} shoulder cannot explain the large region on the peak's left. Thus

both peaks have an additional satellite peak that forms when heated above 575 K. This peak is located 2.0 - 2.5 eV lower in binding energy.

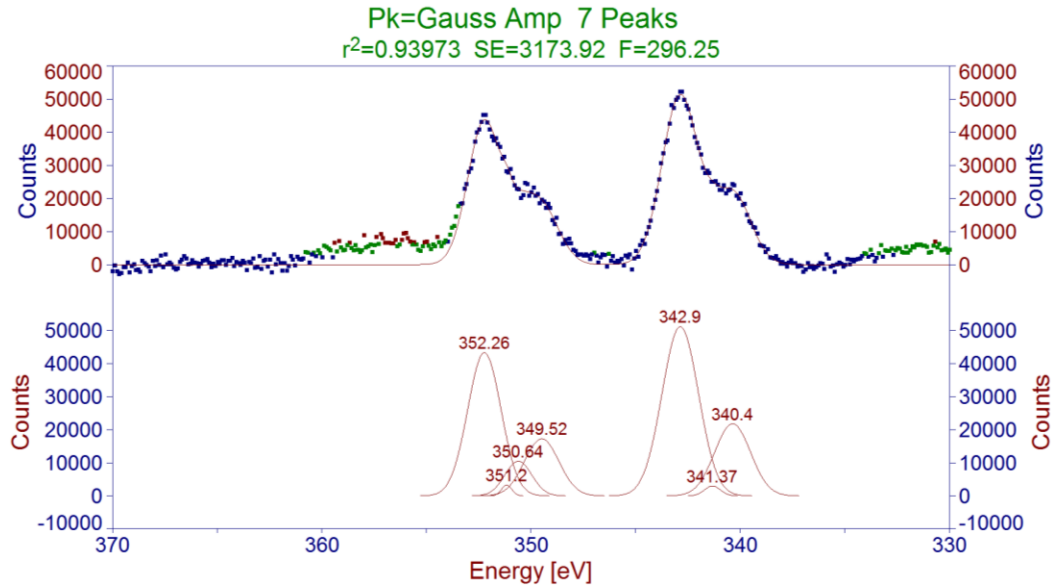


Figure 28. The Th peaks at 675 K during the heating phase of the 2nd sequence. The dots in the upper plot are counts, and the red line is the sum of peaks in the lower plot. Blue dots are within 1 σ of the red line, green dots with 2 σ , and red dots within 3 σ . The energy values in the lower plot mark the centroid of the Gaussian peak.

The discharging of the ThO_2 with heating has multiple possible explanations. First, heating can reduce the band gap of a semiconductor and excite more electrons into the conduction band. But since the band gap of ThO_2 is 6-7 eV, a negligible number of electrons are expected in the conduction band. The band gap may be estimated from the distance between the main Th 4f peak and its shake-up satellite peak. At 675 K the satellite peak is 7.7 eV higher in binding energy and is comparable to 7.1 eV reported in literature [5]. $Fm\bar{3}m$ crystals are potentially pyroelectric [36], which could reduce surface charging. Heating reduces surface impurity concentration and increases the

number of dangling bonds and imperfections. These could be charge transfer sites. Finally, the surface could be chemically reducing, becoming more metallic. This latter hypothesis explains the diminished discharging and increase in the Th 4f metallic character. Reduction and oxidation would describe the reversible process in Figure 27.

4.2.4 Humidity Reduces Adhesion Force for Hydrophilic Indium AFM tip

Humidity significantly increases the adhesion force of hydrophilic materials. Initial estimates concluded that one hour of purging would be required to achieve a dry surface. A separate study of relative humidity and adhesion force using an indium tip proved that humidity significantly alters the total adhesion force validating Equation 5 and subsequently Equation 6. Adhesion force was measured in 1.5 minute intervals. After 15 minutes the relative humidity surrounding the tip and crystal was below 1%. The tip to surface adhesion force had decreased to about 7 nN. The values of the initial adhesion measurements under dry nitrogen from 30 to 60 minutes indicate that the surface to tip adhesion force does not change with additional dry nitrogen time (Figure 29), at least in a significantly measureable manner with this experimental design. For indium, 15 minutes of drying time reduces the total adhesion force by 40%.

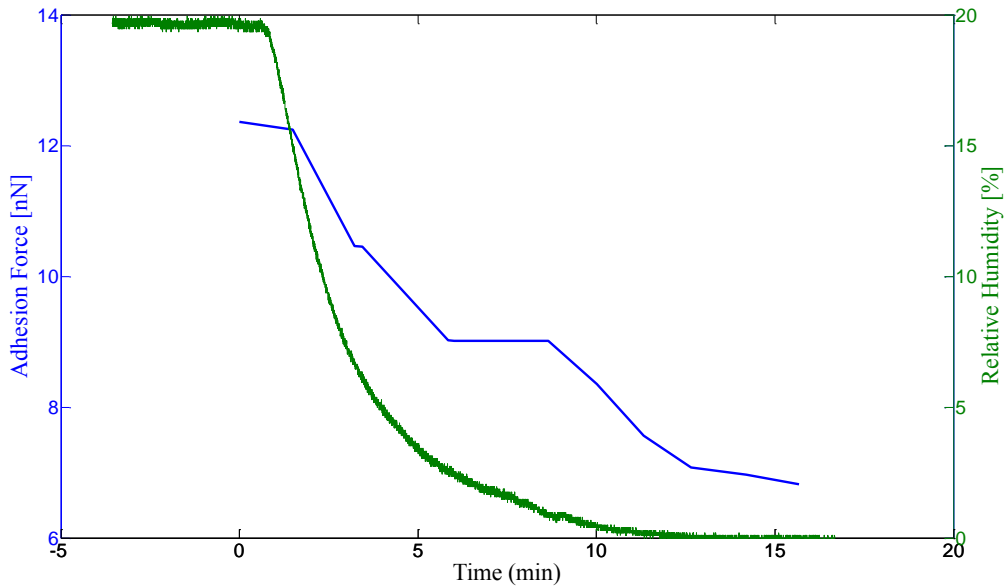


Figure 29. Adhesion force as a function of relative humidity. The adhesion force of the indium metal tip onto the as-grown ThO_2 crystal decreases proportionally with relative humidity. After 15 minutes the relative humidity was below the detectable limit, and the adhesion force had reached a minimum 7 nN.

Under atmospheric conditions, the peak snap exhibits two slopes: one that increases rapidly, and one that increases slowly with a slight curvature (Figure 22). Nickel also exhibited a similar response, except the curved portion was a straight line. Comparatively, titanium had a minimal double slope. Gold did not possess any curved or double slope during the snap portion (Figure 22). A rapidly increasing snap force means a rapidly decreasing adhesion force. This line is associated with van der Waals and dipole-induced dipole force, which rapidly decrease as D^{-6} as stated in Equation 4. The curved or straight gently sloping line is associated with capillary force. As humidity is reduced by the application of dry nitrogen, the curved snap region minimizes and the primary adhesive force contribution is van der Waals and dipole-induced dipole (Figure 30).

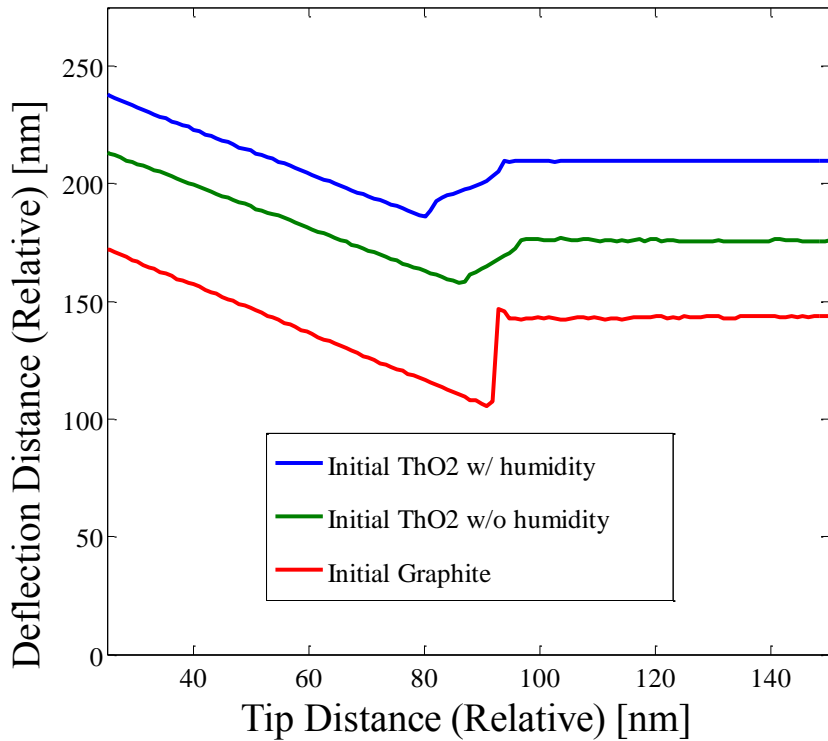


Figure 30. In metal tip adhesion force spectrum on ThO_2 and graphite. The shape of the adhesion force snap length is notably different with changing humidity. The two-phased snap, one that decreases quickly and one that changes slowly, becomes a single phase snap with low relative humidity. Indium metal tip on graphite shows only one adhesion force.

Graphite is considered to be hydrophobic. According to Figure 30, the indium tip when contacting graphite has an even larger snap slope and a smaller snap distance. Again, this straight line snap must be due solely to van der Waals forces. Thus, although the curved In-metal snap region is reduced, there is still an adhesion force due to the capillary force at reduced relative humidity. The nickel tip has the same response as the indium. The gold tip does not exhibit two slopes during the snap phase of retraction. Water has minimal influence on gold's adhesion force to ThO_2 . In fact, according to the measurements of the as-grown crystal, excess water on the surface decreases the adhesion

force from 17 nN to 15 nN. The titanium tip has a single slope during the snap phase of tip retraction; however, the slope is less steep than the gold slope and is proportional to the In slope at low relative humidity. Thus capillary forces do not appear to influence gold under any relative humidity measured in this research. Indium and nickel respond dramatically to the amount of surface hydration, while titanium does less so. Other than a comparative methodology, the degree of surface hydration cannot be determined directly from these measurements.

4.3 Impurities and Adhesion of the Crystal at the End of Cleaning

4.3.1 ThO₂ Impurities Reduced

Though reduced, an impurity concentration remains on the crystal surface after sputtering and heating. The C 1s peak is nearly unchanged, which is not unexpected because 875 K is required to remove C [7]. The F and Cs are revealed after sputtering, implying these constituents are in the bulk-surface layer. Only the F concentration was measurably reduced by heating. The most significant improvements after surface alteration are the changes in the O 1s peak. The adhesion force magnitude remains largely unchanged, although the deviation of the adhesion force based on location improves.

The O 1s peak improves by a factor of 2 after sputter etching and annealing of the sample. The O peak associated with ThO₂ remains nearly constant at 25% of the area of the Th 4f_{7/2} peak. The OH peak area reduces from 13% to 6% of the area of Th 4f_{7/2}. Sputtering resulted in a more Gaussian O 1s profile as in Figure 31.

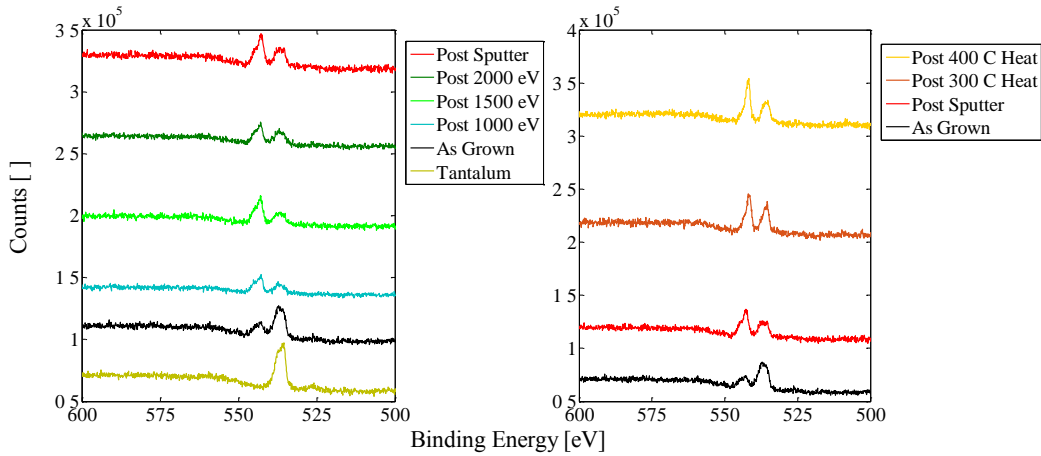


Figure 31. The ThO_2 (left peak) and Ta (right peak) O1s peaks as a function of sputter etching (left side chart) and heating (right side chart).

4.3.2 Th 4f Peak Improvement

The Th 4f peaks have improved in intensity (area) and resolution as in Figure 32.

The Th $4f_{7/2}$ peak intensity improved from $116,000 \pm 4,000$ counts to $300,000 \pm 5,000$ counts and the resolution improved by a factor of 3. Based on Equation 32, the energy resolution is a linear combination of X-ray line width, analyzer detector error, and line width of the photoelectron emission. During the experimentation, the analyzer detector error and X-ray line width did not change, thus the resolution improvement is a result of the improvement in photoelectron emission line width. Based on Equation 33, the thorium peaks become more resolved with nearly constant FWHM (Figure 32). The increased resolution also demonstrates improved surface variability.

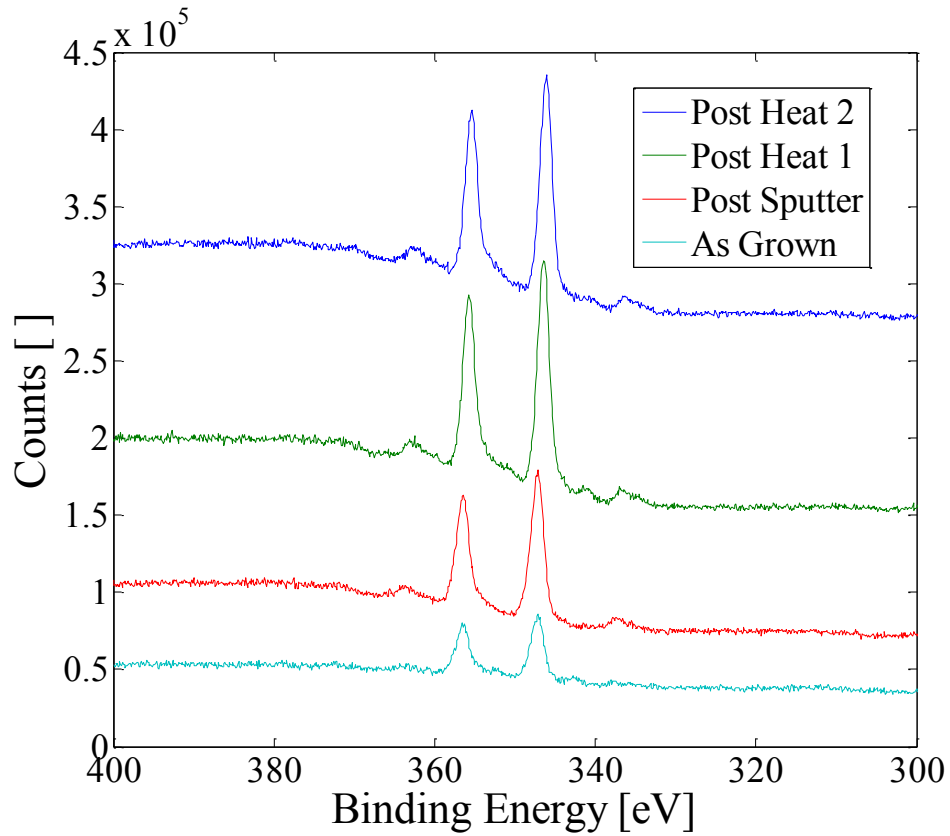


Figure 32. Thorium 4f peaks before and after the surface processing. From left to right: Th $4f_{5/2}$ satellite peak, Th $4f_{5/2}$ peak, Th $4f_{7/2}$ satellite (shoulder), Th $4f_{7/2}$ peak, Th $4f_{7/2}$ peak due to K-alpha 3,4.

4.3.3 Sputtering Improved Surface Variability

The XPS resolution indicates improvement in surface geometry. As the surface is sputter etched, surface features are removed, but defects are generated. Obviously, sputtering is a destructive process and cannot create a perfect crystal face. Sputtering creates defects, occlusions, and irregular surface organization while reducing features. These imperfections scatter the ejected electrons. Improvements in counts under the peak coincide with increased energy spread of the peak (Table 9).

Table 9. Resolution (RES) of the Th $4f_{7/2}$ peak before and after sputter etching. Values are derived from Igor software and error limits the significant figures.

Th $4f_{7/2}$	FWHM [eV]	H [counts]	RES [eV 10^{-5}]
As-grown	1.61	47,600	3.38
Post sputter 1000 eV	1.81	57,400	3.15
Post sputter 1500 eV	1.80	85,700	2.10
Post sputter 2000 eV	1.93	135,000	1.44

An AFM surface scan clearly demonstrates the cleaning of the surface due to sputtering. A histogram of pixel heights above an arbitrary minimum value is plotted in Figure 33. The AFM software converted the color pixel data into height by pixel data, which was then imported into MATLAB. The pixels were summed based on height bins of 2.0 nm for chart a) and 0.75 nm for chart b). The data scale on the initial crystal is 100 nm, while the data scale on the sputtered surface is 50 nm. The as-grown crystal surface has more surface variation than the sputtered surface. The 10% max width of the as-grown is 60 nm, while the 10% max width of the sputtered surface is about 20 nm, a reduction by a factor of 3. The distribution of surface heights is nearly Gaussian in shape. From this information, the surface has changed and although not atomically smooth, the surface features are significantly reduced.

However, these measurements were not from the exact same locations of the crystal surface. Each scan was $3 \times 3 \mu\text{m}$, and it is nearly impossible to find the exact spot repeatedly, although care was taken to be as close as possible. Consequently, it is assumed that these plots are representative of the rest of the crystal surface.

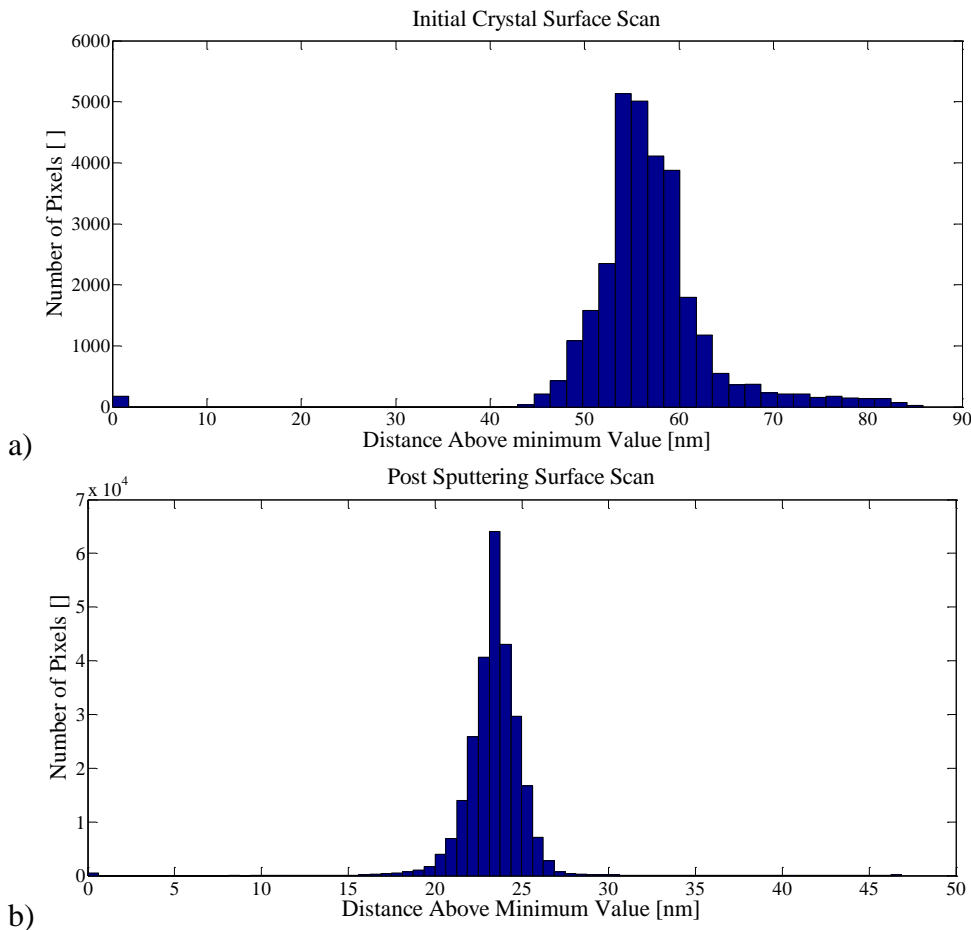


Figure 33. Changes in ThO_2 single crystal geometry and topography histogram. Initially the crystal was extremely rough with wide variation in surface height, almost 50 nm, plot a). After all sputtering runs the variation in crystal height reduced to about 15 nm, plot b). Bins size of 2.0 nm and 0.75 nm were used to create plot a) and b) respectively.

Another unique feature of the sputtered surface is cracking. These cracks may have formed either during the growth process or during surface processing. The cracks are locations where water and adsorbents reside and result in variation in the adhesion force measurements (Figure 34).

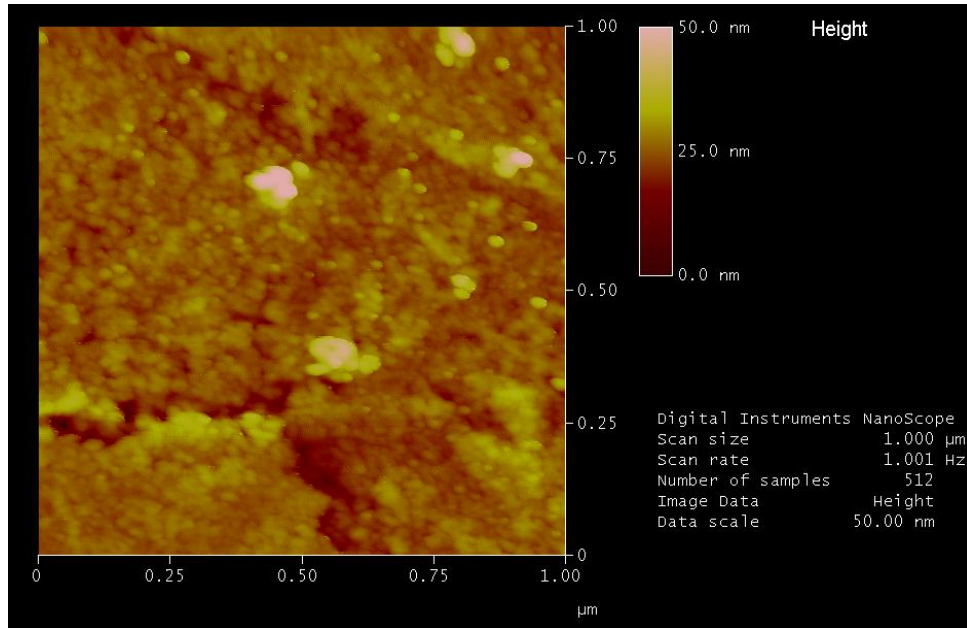


Figure 34. ThO_2 crystal 8a tapping mode surface scan after sputtering and heating. The crystal still has surface features including cracks, plateaus, and adsorbed mounds.

Even with the surface feature reduction, the adhesion force for the metal tips remained comparable to the original numbers, except for gold. Gold originally had a large adhesion force, but after the surface processing, the adhesion force reduced by two fold, which will be further analyzed in Section 4.3.4. The In adhesion changed very little from the beginning to the end of processing and water continued to modify the magnitude of the measured adhesion force.

Direct comparison of capillary force and other adhesion forces between humidity conditions is difficult. From Equation 5, the reduced humidity means less surface hydration; and from Equation 11, the work required to separate the water from the surface, W_{12} , is reduced. Since the surface energy of the metal, γ_m , crystal, γ_c , and water, γ_w , do not change, a reduction in W_{12} causes an increase in residual interface energy of the

crystal, γ_{cw} , and metal γ_{tw} . The increase in interface energy increases the total adhesion force that is not due to capillary force component in Equation 10. Conversely, the decrease in humidity decreases the surface hydration adsorbed and decreases the capillary force contribution to the total adhesion force per Equation 37.

Thus for metal tips (In and Ni) that respond strongly to the capillary force as the main attractive force, the reduction of surface adsorbed water reduces the total force. However, for metal tips (gold) that rely heavily on interface adhesion, a reduction in humidity actually increases their adhesion force, as in Table 10. This is primarily due to the increase in interface energy, as the water does not satisfy the crystal surface energy.

Table 10. AFM adhesion force measurements on ThO₂. Units are in nN. From the as-grown to the cleaned surface, the adhesion force of gold is reduced, while indium, nickel, and titanium remain the same. The variation in adhesion force due to irregularity of the crystal surface is reduced.

[nN]	Au	In	Ni	Ti
Humid as-grown	16 ± 1	13 ± 1	11 ± 1	10 ± 3
Dry as-grown	18 ± 1	10 ± 2	7.7 ± 1.0	7 ± 4
Dry post sputter and heating	8.5 ± 0.5	10 ± 2	6.2 ± 0.7	8.5 ± 0.8

The standard deviations of the adhesion force measurements at the 9 locations dropped significantly. Gold, nickel, and titanium metal tips have a reduction in adhesion force 1σ by half or more. Unfortunately, the In tip was damaged during the humidity measurement study. To ensure similar results for the as-grown crystal to the post cleaning crystal, two new tips were used in the final measurements. The two tips generated different responses, one at about 8.5 ± 0.5 nN and the other at 12.5 ± 1.0 nN,

attributable to different tip radii or metal coverage of the tip. The reduction in the standard deviation can be attributed to the increased uniformity of the surface caused by sputtering at 75° to the surface normal.

4.3.4 Adhesion Force and Interface Energy of Cleaned ThO₂ Crystal

Sputtering and heating the surface resulted in mixed results in the increase of adhesion force due to the increase effective radius of the tip, $R_{t,eff}$. Figure 35 is a plot of the adhesion force, F_{adh} , of the as-grown crystal to the cleaned crystal for the dry conditions as a function of the type of metal tip. Again, new In tips are used for the final measurements and potentially had a different effective tip radius.

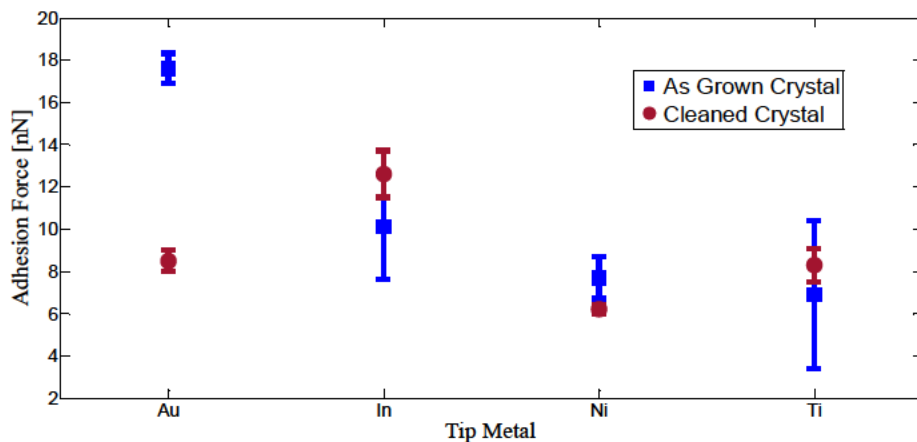


Figure 35. Adhesion force for each metal tip before and after surface processing. The blue squares are the as-grown crystal, and the brown circles are the cleaned crystal. The error bars show 1σ deviation based on measurements at the 9 locations. Indium, nickel, and titanium metals to ThO₂ adhesion force are similar before and after cleaning. The gold exhibits a large decrease in adhesion force after cleaning. The standard error decreases dramatically from the as-grown ThO₂ crystal to the cleaned crystal.

The resulting increase for the titanium adhesion was expected, but gold and nickel both decreased. The post-cleaning crystal measurement for the titanium and nickel adhesion force was within 1σ of the as-grown crystal measurement, and thus it is inconclusive on whether the changes are due to the uniformity of the surface increasing the effective radius or due to surface location deviations. However, gold's dramatic decrease must be attributable to another condition besides tip radius or surface uniformity. Apparently, the cleaned surface under dry conditions has different adhesion properties than the as-grown surface under similar conditions. Although some atmospheric contaminants such as CO_2 and CO were removed by surface processing, the contaminants quickly returned once the crystal was removed from vacuum. Unfortunately, the adhesion measurements cannot be resolved into the cause of the adhesion force.

Using Equation 37 for the cleaned crystal under similar humidity conditions, γ_{tw} , and $R_{t,eff,cap}$ are constant while γ_{tc} and $R_{t,eff,non-cap}$ change. This is the complexity: $R_{t,eff,non-cap}$ should increase with decreasing features, but the magnitude is unknown; γ_{cw} may or may not change, and its magnitude and sign are unknown. Thus the value of interest, γ_{tc} , should change in an uncertain manner. However, a literature review does provide a few tentative solutions.

Individual values for surface energy and interface energy have been measured and computed. The surface energy, γ_I , for the metals used are well known [37]. The surface energy of ThO_2 has also been computed as 1.15 Jm^{-2} . Since the surface tension of water is also known, Equation 11 could be used to compute the interface energy of the metal (γ_{tw}) and crystal (γ_{cw}) except the work reduction is unknown. Several researchers have

investigated the interface energy as a function of humidity and determined most metals hydrate (with other atmospheric contaminants) until their surface energy reduces to 0.045 Jm^{-2} under dry conditions and 0.038 Jm^{-2} for humid conditions [38]. Thus γ_{tw} should be constant since the humidity was controlled in the same manner before and after sputtering.

This assumption may not hold for the ThO_2 crystal. Based on the Kelvin equation (Equation 5), the volume of water is proportional to the humidity; however, since the surface conditions changed by cleaning, the Kelvin radius may have also changed. Thus the exact magnitude and direction of γ_{cw} is unknown.

Table 11. Estimated interface energy of metal to ThO_2 crystal. The values are based on an effective tip radius, $R_{t,eff,non-cap}$, of 5 nm.

$\gamma_T [\text{J m}^{-2}]$	Au	In	Ni	Ti
Dry as-grown	0.28 ± 0.02	0.16 ± 0.03	0.12 ± 0.02	0.11 ± 0.06
Dry final	0.14 ± 0.01	0.17 ± 0.03	0.10 ± 0.01	0.14 ± 0.01

Values for γ_T listed in Table 11 are based on an effective tip radius, $R_{t,eff,non-cap}$ of 5 nm and assume that it is the same for the as-grown and cleaned crystal surfaces. Based on the results from the graphite study, decreasing the surface features increase the adhesion force meaning an increase in the $R_{t,eff,non-cap}$. To make a comparison of the metals, this increase must be considered the same for each tip and is constant.

An illustrative example of the change in the value of γ_{tc} is in Table 12. The value for γ_{cw} is arbitrarily set to decrease by 0.04 Jm^{-2} . Between the tip and crystal, the residual interface energy increases for gold, but decreases for the other metals. Even with a

different value of γ_{cw} , the gold γ_{tc} value will always be more positive than the other metals. By cleaning the crystal surface, the adhesion of gold to ThO₂ decreased dramatically. Impurities, defect sites, and/or adsorbed material enhanced gold adhesion to the crystal.

Table 12. The change in estimated interface energy values from the as-grown to the cleaned crystal. For comparison the $R_{t,eff,non-cap}$ is estimated to be 5 nm and γ_{cw} is estimated to decrease by 0.04 Jm⁻².

[Jm ⁻²]	γ_T	γ_{tw}	γ_{cw}	γ_{tc}	$\cos(\theta)R_{t,eff,cap}$
Au	-0.14	N/C	-0.04	+0.10	N/C
In	+0.01	N/C	-0.04	-0.05	N/C
Ni	-0.02	N/C	-0.04	-0.02	N/C
Ti	+0.03	N/C	-0.04	-0.07	N/C

Under the conditions of this experiment, the adhesion force of the metals to the surface processed ThO₂ is In>Au~Ti>Ni. This trend is valid under the following caveats: every metal adsorbs water and atmospheric contaminants resulting in the same interface energy, the tip metals are unoxidized or chemically unaltered, the tips are the same size with the same effective contact radius, and the residual energy for each metal is the equivalent. Unfortunately, Equation 37 only explains trend information and is unable to predict or compute accurate values for the interface energy and adhesion force. However, since the goal of this work was to determine the efficacy of using AFM and XPS techniques to identify a potential metal contact from a set of candidates, this has proven to be successful. The precise values may need additional theoretical and experimental measurements.

V. Conclusions and Recommendations for Future Research

5.1 General

Sputter etching the ThO₂ crystal surface at 2000 eV at 75° with respect to the surface normal significantly improves the surface uniformity. The Th 4f peaks peak resolution improved two fold. The AFM surface scan analysis reveals three fold reduction in the crystal height deviation and results in Gaussian peak profiles. Finally, the standard deviation of the adhesion force measurements improves by a factor of 2. Yet, the surface is not smooth enough to increase the total adhesion force and thus increase the effective radius of the tip.

Sputtering and heating reduce the number of impurities in the sample. Sputtering reveals F and Cs concentrations in the top crystalline layers; their associated XPS peaks resolve with high energy sputtering. Annealing is able to reduce the F 1s signature to less than 1% ratio with Th 4f_{7/2}, but the Cs peaks remain. This is either due to cesium's very low lattice mobility, or more likely, not enough energy was provided to sputter etch entire surface layers (a purposeful result to prevent chamber contamination). Heating reduced the OH shoulder on the Th O 1s peak by half (from 11% to 5.7%), but C was not measurably reduced by the sputtering or heating cycles. Additional heating is required to remove the Cs and C from the ThO₂ surface.

Heating the crystal from room temperature to 675 K reduces the amount of charging from 7.3 eV to 4.0 eV. The Fermi function fits the discharging curves and predicts the amount of charging for temperatures in excess of 675 K. The binding energy

formula must be corrected for charging with the inclusion of the Fermi function (Equation 38). The metallic Th $4f$ peaks appear in the XPS spectrum at 2.5 eV lower in binding energy than the oxide Th $4f$ peaks. The most likely explanation is that the ThO_2 surface is becoming more metallic allowing surface discharge and increasing surface metallic characteristics through oxidation and reduction mechanisms that have not yet been published in literature. Because of the charging of the sample, the C $1s$ and O $1s$ peaks are resolved from the Ta associated C $1s$ and O $1s$.

Measuring the adhesion force of metal tips to ThO_2 using AFM is feasible and an interesting study. For a surface processed ThO_2 single crystal, In has the largest adhesion force. However, the exact nature of adhesion for the different metals is difficult to determine. Since In has a large potential capillary contribution, gold could have the largest adhesion force due to the interface energies. All interface energy and adhesion force equations depend on effective tip radii. Unless each tip's radius is measured before and after each AFM spectrum, the exact radius during the measurement is unknown. Thus Equations 36 and 37 may be entirely accurate, but only provide trend information and post-data explanation of the results. Furthermore, even with the knowledge of the tips' radii, the amount of crystal surface contacted by the tip will vary based on the crystal roughness.

Gold adheres better to the as-grown ThO_2 surface than to the processed surface. If the impurities and defects on the surface result in poor Ohmic contact, then gold is not a suitable candidate. Capillary forces are significant to hydrophilic metals. An increase in capillary force has a corresponding decrease in the residual interface energy of the tip and crystal. Hydrophilic metal tips (e.g. Ni and In) demonstrate substantial decreases in

adhesion force with the reduction of water. Hydrophobic metals (e.g. gold) have a slight increase in adhesion force due to increased interface energy of the hydrated ThO₂ surface. The magnitude of the changes determines the total interface energy increase or decrease.

Initially, the adhesion force and interface energy is Au>In>Ni>Ti. Post sputtering, In>Au~Ti>Ni for adhesion force and interface energy. From the results of these experiments, indium is the best metal to make a contact to ThO₂. The adhesion force of the cleaned crystal to indium was the highest under the conditions of this experiment. Indium is influenced by the capillary force, but the complete removal of water in a vacuum is not generally feasible. Initial XPS measurements to ThO₂ conducted at 10⁻⁹ Torr had an OH shoulder on the O peak. Thus, during vapor deposition, there will be water on that surface. Indium's low work function and low melting point make it an ideal material to use as a contact material.

The XPS and AFM combination are suitable methods to monitor the geometry and chemistry of crystal surfaces. Each technique provides multiple data sets with interesting features to analyze. Even now, there is more data that may be analyzed, and additional features of each measurement device that may be used to extract more information.

5.2 Future Research

A methodology to control the AFM adhesion variables must be determined. The radius of the tip was always unknown and estimated in this research. SEM measurements would alleviate this uncertainty, instead of using graphite as a surrogate to infer tip geometry. The metal that adhered to the surface has a thickness 2-10 nm. Better control

of metal deposition on the tips needs to be maintained. Some measure of tip-damage resulting from measurement is necessary, which the SEM technique may satisfy. Measuring with 9 tips at 9 locations would increase the statistical accuracy, although it also would increase the laboratory time.

Additional hydrophobic metals should be compared to gold. Aluminum is an interesting candidate since it oxidizes readily and is very non-polarizable. This would provide information about the surface van der Waals interactions.

The charging and discharging of the ThO₂ provides an interesting study of the electrical nature of single crystal ThO₂. A Low Energy Electron Diffraction (LEED) system emitting low energy electrons could operate as a flood gun and neutralize the positive charge building up on the surface. By reducing the amount of charging, the spectral contraction could be analyzed. Also, by increasing the O partial pressure inside the vacuum chamber, the nature of the oxidation and reduction thermodynamics and kinetics could be determined. Heating above 675 K should confirm the Fermi sigmoid and provide further evidence to the metallic nature of the surface.

The contraction of the XPS spectrum due to charging is a unique discovery. The parameters of the linear fit equation have a physical meaning, where the ordinate intercept is the work function of the system plus charging of the sample. The slope is a function of the interaction of electrons, at a specific energy (abscissa), with the charged crystal surface.

Efficient surface processing requires additional investigation as 400° C was insufficient to drive off surface adsorbed carbon and oxygen. Procedures in literature specify heating ThO₂ to 1173-1273 K for cleaning [31, 35] in order to obtain LEED

patterns. Also heating to higher temperatures will provide ThO₂ molecules additional energy to overcome surface binding energies for more efficient annealing.

LEED is a suitable technique for determining the cleanliness and surface regularity of a single crystal. If the surface is not cleared of contaminants, the low energy electrons cannot depart the crystal. If the crystal does not have long range order, a LEED pattern will not appear [35]. If too many surface features exist on the crystal a distorted, imperfect LEED pattern is produced. Because ThO₂ has high symmetry, *Fm3m*, the LEED pattern should be simple to interpret [39]. Thus, LEED measurements provide another detailed method of analyzing the uniformity of the ThO₂ crystal surface.

Finally, understanding the influence of humidity and ThO₂ surface hydration is critical. Infrared spectroscopy (IR) provides information about the bonding of water at the surface. Scanning electron microscopy (SEM) provides the ability to measure the surface angle of water, θ , on various surfaces providing information on capillary force, as in Equations 7 and 8. Under vacuum, AFM would provide adhesion measurements in the same conditions that the metal would be deposited, and the humidity related variables could be controlled. The surface and interface energy relaxations of the metal and thorium would be at similar conditions. Finally, the AFM tips should be monitored for geometry change and metal removal.

Appendix A

Load lock sample change out procedures

Vacuum to Atmosphere

- 1) Close valve to main chamber
- 2) Close valve to turbo pump
- 3) Turn off load lock turbo pump: push stop button
- 4) Turn off load lock vac ion pump: push “start protect 1” button, push “HV1 on/off” button, turn off main switch
- 5) Switch off load lock ion gauge: menu, FP control, on/off, up arrow, enter
- 6) Switch off argon gun ion gauge: menu, off, enter
- 7) Turn nitrogen gas flow at cylinder – ensure slow steady flow
- 8) Connect nitrogen hose to load lock fill tube
- 9) Twist to open load lock door handle (do not want to pressurize the system)
- 10) Open green valve slowly to push nitrogen into load lock – pressure should reach about 760 Torr (this can be accomplished from the load lock side, best to monitor the pressure)

Atmosphere to Vacuum

- 1) Close door on load lock and secure tightly
- 2) Immediately close green valve on back of load lock (can be accomplished from load lock side, step 2 and 3 can be done simultaneously)
- 3) Turn off nitrogen flow at cylinder and remove hose from load lock fill tube
- 4) Ensure turbo pump is <5000 rpm
- 5) Open main valve to turbo pump: twist counterclockwise slowly until hear two clicks (valve is now unseated), continue twisting slowly (listen for scroll pump audio change – do not overwork the scroll pump)
- 6) Draw vacuum to <7.5E-3 Torr
- 7) Turn on turbo pump: press start button
- 8) Switch on load lock ion gauge: menu, FP control, on/off, up arrow, enter
- 9) Switch on argon gun ion gauge: menu, on, enter
- 10) Draw vacuum to <1E-6 Torr and allow turbo to reach 27,000 rpm
- 11) Turn on vac ion pump: push main switch to on, push “HV1 on/off”, wait until voltage reaches 7,000 V, press “start protect 1”.

Sputtering of sample procedures

Setup

- 1) Set argon gun ion gauge to mBar
- 2) Ensure argon line leak valve is closed
- 3) Turn off load lock ion gauge
- 4) Open valve on argon tank: ensure pressure is 50kPa (first line above 0)

- 5) Open green valve on the argon tank line $\frac{1}{2}$ turn
- 6) Slowly open leak valve until $>1E-5$ mBar pressure in argon gun reaction chamber
(8ea $\frac{1}{4}$ turns until pressure increase, but when it does, it is very sensitive)
- 7) Turn on the ion gauge in the load lock. Pressure should be $<5.0E-7$ Torr.
- 8) Degas at least 3x, continue to degas until pressure does not significantly change in argon gun reaction chamber
- 9) Allow pressure to return to $\sim 1E-5$ mBar in argon gun reaction chamber and $\sim 5.0E-7$ Torr in load lock chamber
- 10) Close the bypass leak valve with a $\frac{3}{4}$ " open end wrench (this will increase pressure in argon gun reaction chamber)
- 11) Adjust the leak valve (clockwise) to keep the pressure below $2E-4$ mBar
- 12) Select sputter settings
 - a) Factory defined: push recall, push number that represents the settings
 - b) User defined: push modify, select parameter to adjust, twist large black knob to select value, select next parameter
- 13) Operate the argon sputter
- 14) Ensure maximum emission current by increasing the argon pressure in argon gun by opening the leak valve. Pressure should be between $1.0 E-4$ mBar and $1.5E-4$ mBar.

AFM measurement procedures

AFM Multimode Startup Procedures

- 1) Turn on computer (ns3a)
- 2) Turn on all three monitors
- 3) Turn on controller computer – toggle switch in the rear of device (allow 30 minutes for warm-up when taking spectrum)
- 4) Launch software Nanoscope V5.31r1
- 5) Switch multimode from STM to AFM. Ensure laser light is in sample area
- 6) Turn on optical light. Light control box is located on the back side of the AFM workbench
- 7) Ensure the slide is in the stage; if not, follow AFM Tip Installation
- 8) Ensure tip is in view of the microscope.
- 9) Focus microscope onto sample.
- 10) Lower tip to sample by toggling switch “down” in pulses until the tip comes into focus (tip should look like one section0
- 11) Adjust laser onto tip by adjusting the knobs on the upper right hand side
- 12) Maximize signal hitting the detector by adjusting the mirror. Handle behind the AFM head.
- 13) Move the detector to the center of the laser beam. The upper and low numbers should read near zero. Back left buttons move the x and y directions.
- 14) Adjust the top reading to -0.5 which is negative pressure (tip is still above the surface)

- 15) If running a adhesion measurements only, change the surface scan area to 1nm before step 16.
- 16) Press the green icon microscope button to engage the tip.

AFM Tip Installation

- 1) Turn AFM holding plate upside down
- 2) Grab the AFM tip with needle nose tweezers at near 90 degree angle
- 3) Push AFM holding plate down to open copper holding bar
- 4) At a 25 degree angle slide AFM tip under copper holding bar and in between the two side holding notches.
- 5) Ensure AFM tip is perpendicular to AFM holding plate with freestanding microscope.
- 6) Ensure AFM head holding bracket is up. Turn knob behind optical port.
- 7) Ensure AFM sample stage (and sample) is below four ball bearing resembling supports.
- 8) Insert AFM holding plate into AFM head at a 25 degree angle so that divots fit over the ball bearing resembling supports.
- 9) Ensure holding plate is in the supports.
- 10) Close AFM head holding bracket. Turn knob behind optical port.

AFM Force Measurements

- 1) Ensure software is set for contact mode in “other control” box
- 2) Set scan size for 1 nm
- 3) Choose AFM tip location (relative to (0,0)) in the x and y coordinates
- 4) Ensure deflection set point is at 0.5 V
- 5) Engage tip by clicking green tip icon
- 6) Allow system to stabilize: view scan screen and watch for changes in zscan number
- 7) Click “view”, “Force Mode”, “Calibrate”
- 8) Adjust the range to 500 nm (should not change)
- 9) Adjust the scan rate to 1Hz (should not change)
- 10) Adjust the number of samples to 512 (should not change)
- 11) Adjust the Data scale so that the peak fits in the window
- 12) Adjust deflection setpoint: - is up and + is down, so that the cantilever zero line is at 0 deflection.
- 13) Adjust the zscan scale: - is left and + is right, so that the adhesion dip is two intervals from the left hand side of the screen
- 14) Click on the deflection gain setting. Click the upper portion of the repulsive force then click on the lower portion of the adhesive force to attain the slope of that curve. Readjust the data scale if necessary.
- 15) Click utility and filename to change the file name
- 16) Click the capture image button (camera) to take data.
- 17) Click the eyeball button to return to the main AFM screen
- 18) Click the red AFM tip button to retract the tip
- 19) Complete steps 3-7 and 11-13 and 16-18 for repeating the process.

Appendix B

Silicon Sputtering Results

To ensure accurate sputter etching of the ThO₂ single crystal a series of sputtering was conducted on Si(111). Silicon was chosen because of its availability, surface uniformity, and ability to directly compare results to empirical formula. A 6 inch Si(111) wafer was fractured into smaller fragments. The surface was cleaned with acetone and ethanol to remove contaminants. The surface nearly atomic flat and would provide sufficient ability to compute volume sputtered.

The tests demonstrated the argon gun's ability to change beam current shape, shift location, and raster an area. To this end, the energy of the beam was held constant at 5000 eV, the time sputtered held at 30 minutes, and the emission current held at 10 mA.

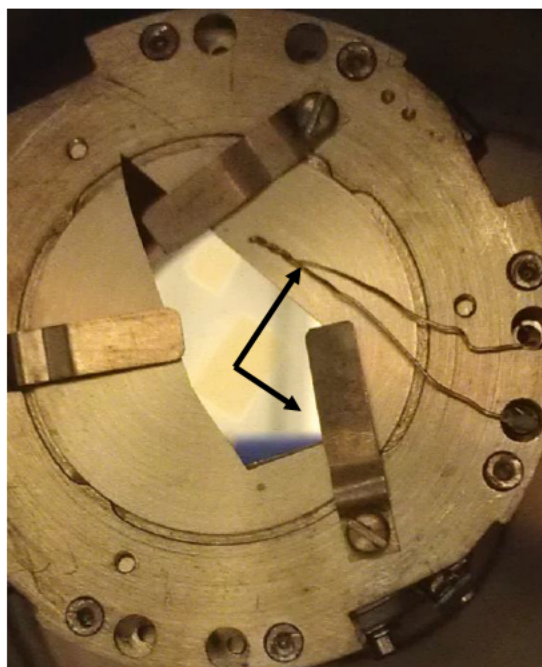


Figure A. (111) Si wafer sputtered at 5000 eV by Ar⁺.

The volume of the sputtered surface is compared against the theoretical empirical values. Test 3 sputtered volume has the shape of a rectangular pyramid, and thus very simple to determine the volume. With a sputtered area of 24 mm^2 at maximum depth and sputtered area of 900 nm at the crystal surface, the volume sputtered is 0.050 mm^3 . According to Yamamura the parameters for Si is $W_{Z2} = 2.32$, $U_s = 4.63 \text{ eV}$, $Z_2 = 14$, $M_2 = 28.085 \text{ g cm}^{-3}$, and $s = 2.5$. Based on these numbers, the sputter yield is 1.3 atoms/ion, from Equation 18. Test 3 had a beam current range from $19\text{-}24 \mu\text{A}$ and a sputter time of 30 minutes. The volume of material sputter is computed with Equation 27 and found to be 0.007 mm^3 .

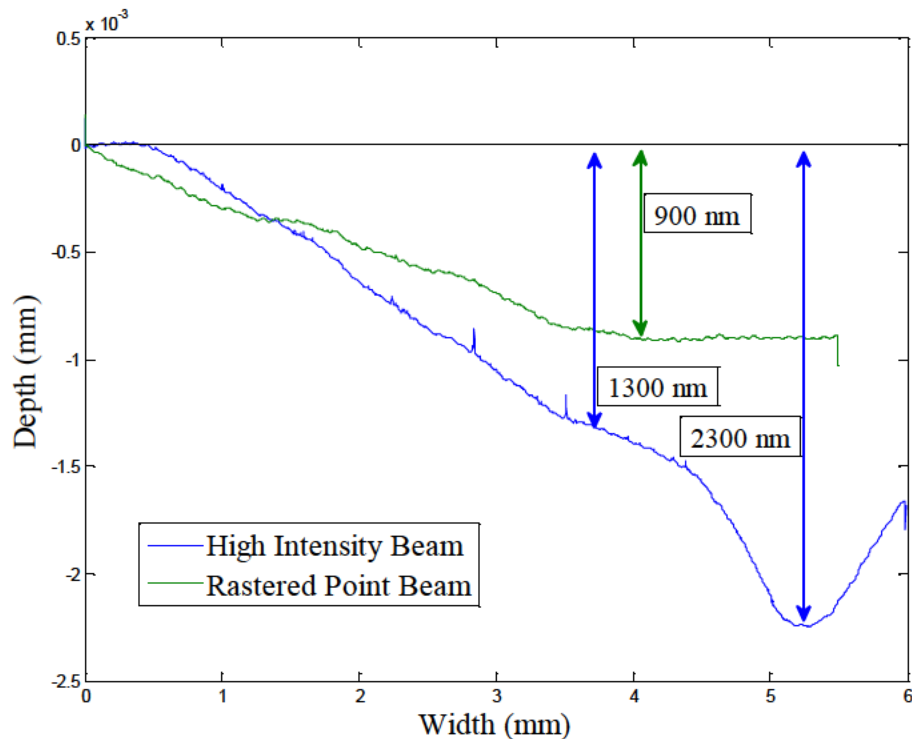


Figure B. Profilometer scan of the Si (111) wafer. The blue curve depicts the depth of the high current beam and the green curve represents the low current rastered scan.

This study generated interesting information concerning the operations of the argon sputtering gun and the vacuum system setup. The argon sputtering gun axis is not up and down, left and right, but at a 30° cant, see Figure A. Also, the argon ion beam does not strike the center of the sample holder, but about 2 mm right of the argon gun y axis. The Ar⁺ beam current is directly proportional to the argon ion partial pressure in the argon gun reaction chamber. Close control of the argon pressure will ensure more uniform beam current. Because the argon gun has a recycling mechanism for low energy argon ions, the pressure in the reaction chamber tends to increase with time. Thus the leak valve should be tightened to keep the reaction chamber pressure below 1.5x10⁻⁴ mBar. The working distance of the argon gun to sample plate is slightly larger than the manufacturer settings. Thus the sputtered region is larger than the width settings on the control unit. Beam spread due to charged ion repulsion and nominal beam width cause non-uniform sputtering at the edges of the sputtered area. For uniform sputtering, the sample should be entirely contained inside the sputtered area.

Based on test results, the rastered, low current beam provided the most uniform sputter. Special care of the angle of deflection is required to strike the crystal surface.

References

- [1] G. Wilk, R. Wallace and J. Anthony. Hafnium and zirconium silicates for advanced gate dielectrics. *Journal of Applied Physics* 87(1), pp. 484-492. 2000.
- [2] R. Terki, H. Feraoun, G. Bertrand and H. Aourag. First principles calculations of structural, elastic and electronic properties of XO₂ (X = Zr, hf and th) in fluorite phase. *Computational Materials Science* 33(1–3), pp. 44-52. 2005.
- [3] F. Ergin, R. Turan, S. Shishiyau and E. Yilmaz. Effect of gamma-radiation on HfO₂ based MOS capacitor. *Nuclear Instruments & Methods in Physics Research Section B-Beam Interactions with Materials and Atoms* 268(9), pp. 1482-1485. 2010. . DOI: 10.1016/j.nimb.2010.01.027.
- [4] J. A. Felix, D. M. Fleetwood, R. D. Schrimpf, J. G. Hong, G. Lucovsky, J. R. Schwank and M. R. Shaneyfelt. Total-dose radiation response of hafnium-silicate capacitors. *Nuclear Science, IEEE Transactions on* 49(6), pp. 3191-3196. 2002.
- [5] T. D. Kelly, "Electronic and Physical Characterization of Hydrothermally Grown Single Crystal ThO₂," December, 2013.
- [6] A. Demkov and A. Navrotsky, Eds., *Material Fundamentals of Gate Dielectrics*. Netherlands: New York, 2005.
- [7] J. Belle and R. M. Berman, "Thorium dioxide: properties and nuclear application," *Naval Reactors Office USDOE*, 1984.
- [8] (January 2015). *WebElements* [Crystal Structure Indium]. Available: <http://www.webelements.com/>.
- [9] M. Bagge-Hansen, R. A. Outlaw, K. Seo and D. M. Manos. Morphology and crystallization of ThO₂ thin films on polycrystalline ir. *Thin Solid Films* 520(13), pp. 4249-4253. 2012.
- [10] M. C. Cheynet, S. Pokrant, F. D. Tichelaar and J. Rouviere. Crystal structure and band gap determination of HfO₂ thin films. *Journal of Applied Physics* 101(5), pp. 054101-054101-8. 2007. . DOI: 10.1063/1.2697551.
- [11] B. Zeghbrouck (2011). *Principles of semiconductor devices*. Available: <http://ecee.colorado.edu/~bart/book/book/title.htm>. DOI: Jun 2014.
- [12] R. K. Behera and C. S. Deo. Atomistic models to investigate thorium dioxide (ThO₂). *Journal of Physics-Condensed Matter* 24(21), pp. 215405. 2012.

- [13] R. Jones, H. Pollock, J. Cleaver and C. Hodges. Adhesion forces between glass and silicon surfaces in air studied by AFM: Effects of relative humidity, particle size, roughness, and surface treatment. *Langmuir* 18(21), pp. 8045-8055. 2002.
- [14] W. P. Ellis, A. M. Boring, J. W. Allen, L. E. Cox, R. D. Cowan, B. B. Pate, A. J. Arko and I. Lindau. Valence-band photoemission intensities in thorium dioxide. *Solid State Commun.* 72(7), pp. 725-729. 1989.
- [15] T. Eastman and D. Zhu. Adhesion forces between surface-modified AFM tips and a mica surface. *Langmuir* 12(11), pp. 2859-2862. 1996.
- [16] M. D. Mathews, B. R. Ambekar and A. K. Tyagi. Bulk and lattice thermal expansion of Th_{1-x}Ce_xO₂. *Journal of Nuclear Materials* 280(2), pp. 246-249. 2000.
- [17] F. Skomurski, L. Shuller, U. Becker and R. Ewing. The corrosion of UO₂ and ThO₂: A quantum mechanical investigation. *Journal of Nuclear Materials* 69, pp. 411. 2005.
- [18] P. Atkins, *Physical Chemistry*. New York: W. H. Freeman and Company, 1998.
- [19] J. N. Israelachvili. *Intermolecular and Surface Forces* (Second Edition ed.) 1995.
- [20] D. Sedin and K. Rowlen. Adhesion forces measured by atomic force microscopy in humid air. *Analytical Chemistry* 72(10), pp. 2183-2189. 2000.
- [21] Y. Yamamura and H. Tawara. Energy dependence of ion-induced sputtering yields from monatomic solids at normal incidence. *Atomic Data and Nuclear Data Tables* 62(2), pp. 149-253. 1996.
- [22] T. Kelly, "TOF-SIMS of Hydrothermally Grown Single Crystal ThO₂," 2015.
- [23] S. Hüfner. *Photoelectron Spectroscopy : Principles and Applications* / 2003.
- [24] W. McLean, C. A. Colmenares and R. L. Smith, "Electron-spectroscopy studies of clean thorium and uranium surfaces. Chemisorption and initial stages of reaction with O₂, CO, and CO₂," *Physical Review B (Solid State)*, vol. 25, pp. 25, 1 January, 1982.
- [25] A. Teterin, M. Ryzhkov, Y. Teterin, K. Maslakov, T. Reich and S. Molodtsov. Emission of ThO₂ valence electrons upon excitation with synchrotron radiation near the O 4, 5 (th) resonance absorption threshold. *Radiochemistry* 51(6), pp. 560-566. 2009.
- [26] R. Eisberg and R. Resnick, *Quantum Physics of Atoms, Molecules, Solids, Nuclei, and Particles*. USA: John Wiley & Sons, 1985.

- [27] B. W. Veal and D. J. Lam. X-ray photoelectron studies of thorium, uranium, and their dioxides. *Physical Review B (Solid State)* 10(12), pp. 4902-8. 1974.
- [28] P. van der Heide, *X-Ray Photoelectron Spectroscopy*. Hoboken: John Wiley & Sons, 2012.
- [29] J. Fuggle, A. Burr, L. Watson, D. Fabian and W. Lang. X-ray photoelectron studies of thorium and uranium. *Journal of Physics F: Metal Physics* 4(2), pp. 335. 1974.
- [30] D. Lide, Ed., *CRC Handbook of Chemistry and Physics*. New York: CRC Press, 2003.
- [31] T. N. Taylor, C. A. Colmenares, R. L. Smith and G. A. Somorjai. The thorium (100) crystal face: A study of its cleaning, surface structure, and interaction with oxygen and carbon monoxide. *Surface Science* 54(2), pp. 317-339. 1976.
- [32] A. Hu and A. Hassanein. How surface roughness affects the angular dependence of the sputtering yield. *Nuclear Instruments & Methods in Physics Research Section B-Beam Interactions with Materials and Atoms* 281pp. 15-20. 2012.
- [33] (15 September 2012). *NIST x-ray photoelectron spectroscopy database*. Available: <http://srdata.nist.gov/xps/Default.aspx>.
- [34] K. Yao, D. Kwabi, R. Quinlan, A. Mansour, A. Grimaud, Y. Lee, Y. Lu and Y. Shao-Horn. Thermal stability of Li₂O₂ and Li₂O for li-air batteries: In situ XRD and XPS studies. *Journal of the Electrochemical Society* 160(6), pp. A824-A831. 2013.
- [35] R. Bastasz, C. A. Colmenares, R. L. Smith and G. A. Somorjai. A LEED and AES study of the structure, debye temperature, and oxidation of the (111) crystal face of thorium. *Surface Science* 67(1), pp. 45-60. 1977.
- [36] J. Kim, J. Baek and P. Halasyamani. (NH₄)₂Te₂WO₈: A new polar oxide with second-harmonic generating, ferroelectric, and pyroelectric properties. *Chemistry of Materials* 19(23), pp. 5637-5641. 2007.
- [37] L. Vitos, A. V. Ruban, H. L. Skriver and J. Kollár. The surface energy of metals. *Surface Science* 411(1–2), pp. 186-202. 1998.
- [38] M. Bennett and W. Zisman. Effect of adsorbed water on the critical surface tension of wetting on metal surfaces. *J. Colloid Interface Sci.* 28(2), pp. 243-249. 1968.
- [39] L. J. Clarke, *Surface Crystallography: An Introduction to Low Energy Electron Diffraction*. New York: John Wiley & Sons, 1985.

Vita

MAJ Scott W. Key graduated with a Bachelor of Science in Chemistry from Mercer University and was commissioned into the US Army as a 2nd Lieutenant in the Ordnance Corps. He served in Germany with the 1st Infantry Division, Alaska with the 25th Infantry Division, and Aberdeen Proving Ground with the 20th Support Command (CBRNE). His last assignment before arriving at AFIT was the Assignment Officer for Functional Area 52 at the Army Human Resources Command. He commanded a maintenance company in the 25th Infantry Division for 18 months. He deployed to Iraq twice in support of Operation Iraqi Freedom.

REPORT DOCUMENTATION PAGE				Form Approved OMB No. 074-0188	
<p>The public reporting burden for this collection of information is estimated to average 1 hour per response, including the time for reviewing instructions, searching existing data sources, gathering and maintaining the data needed, and completing and reviewing the collection of information. Send comments regarding this burden estimate or any other aspect of the collection of information, including suggestions for reducing this burden to Department of Defense, Washington Headquarters Services, Directorate for Information Operations and Reports (0704-0188), 1215 Jefferson Davis Highway, Suite 1204, Arlington, VA 22202-4302. Respondents should be aware that notwithstanding any other provision of law, no person shall be subject to an penalty for failing to comply with a collection of information if it does not display a currently valid OMB control number.</p> <p>PLEASE DO NOT RETURN YOUR FORM TO THE ABOVE ADDRESS.</p>					
1. REPORT DATE (DD-MM-YYYY) 26-03-2015	2. REPORT TYPE Master's Thesis	3. DATES COVERED (From – To) June 2013 – March 2015			
TITLE AND SUBTITLE Surface Geometry and Chemistry of Hydrothermally Synthesized Single Crystal Thorium Dioxide			5a. CONTRACT NUMBER		
			5b. GRANT NUMBER SC86R-84752F-503000		
			5c. PROGRAM ELEMENT NUMBER		
6. AUTHOR(S) Key, Scott W., Major, USA			5d. PROJECT NUMBER		
			5e. TASK NUMBER		
			5f. WORK UNIT NUMBER		
7. PERFORMING ORGANIZATION NAMES(S) AND ADDRESS(S) Air Force Institute of Technology Graduate School of Engineering and Management (AFIT/ENP) 2950 Hobson Way, Building 640 WPAFB OH 45433-8865			8. PERFORMING ORGANIZATION REPORT NUMBER AFIT-ENP-MS-15-M-87		
9. SPONSORING/MONITORING AGENCY NAME(S) AND ADDRESS(ES) Domestic Nuclear Detection Office 245 Murray Drive, Building 410 Washington DC 20528 POC: Mr. William Ulicny Email: William.Ulicny@HQ.DHS.GOV			10. SPONSOR/MONITOR'S ACRONYM(S) DNDO		
			11. SPONSOR/MONITOR'S REPORT NUMBER(S)		
12. DISTRIBUTION/AVAILABILITY STATEMENT DISTRUBTION STATEMENT A. APPROVED FOR PUBLIC RELEASE; DISTRIBUTION UNLIMITED.					
13. SUPPLEMENTARY NOTES This material is declared a work of the U.S. Government and is not subject to copyright protection in the United States.					
14. ABSTRACT The surface chemistry and geometry of hydrothermally grown, single crystal ThO ₂ was studied using X-ray Photoemission Spectroscopy (XPS) and Atomic Force Microscopy (AFM). The crystal was studied before and after sputter etching with Ar+, heating up to 675 K, and dehydration with dry nitrogen. The hydrothermal growth technique incorporated Cs and F into the near surface bu k. Heating to 675 K drove off the F, but did not the Cs. Sputtering with Ar+ at 75° cleaned the crystal and created a more uniform surface geometry. The Th 4f peak resolution, as measured by XPS improved by a factor of 3, the surface roughness, as measured by AFM, reduced by a factor of 2, and the error in adhesion force measurements at different location on the crystal reduced by a factor of 2. The surface of ThO ₂ becomes more metallic with heating. X-rays, used in XPS, created 7.3 eV of charging on the ThO ₂ crystal surface at room temperature. Metallic Th 4f peaks appeared in the XPS spectrum at 675 K, while the charging was reduced. The as-grown crystal, the adhesion force strength by metal was Au>In>Ni>Ti. Post cleaning the adhesion force change to In>Au~Ni>Ti. Interface energy computations confirm that the Au metal adhesion decreased by half for the cleaned crystal. Based on these results, indium is the best choice of metal for application of contacts to the ThO ₂ single crystal used in this research.					
15. SUBJECT TERMS ThO ₂ , thoria, XPS, AFM, sputtering, sputter etch, surface energy, interface energy, adhesion					
16. SECURITY CLASSIFICATION OF: a. REPORT U		17. LIMITATION OF ABSTRACT b. ABSTRACT U	18. NUMBER OF PAGES c. THIS PAGE U	19a. NAME OF RESPONSIBLE PERSON Tony D. Kelly, AFIT/ENP	
			114	19b. TELEPHONE NUMBER (Include area code) (937) 255-6565, ext 4697 (tony.kelly@afit.edu)	

Standard Form 298 (Rev. 8-98)
Prescribed by ANSI Std. Z39-18